The effect of the antioxidant alpha-tocopherol on the structure of phospholipid model membranes and lipid phase behaviour

Divya Malia

Department of Chemistry

Imperial College London

A thesis submitted for the degree of Doctor of Philosophy,

June 2022

I, Divya Malia, declare that the work carried out in this thesis is my own unless otherwise stated

Copyright statement

The copyright of this thesis rests with the author. Unless otherwise indicated, its contents are licensed under a Creative Commons Attribution Non-Commercial 4.0 International Licence (CC BY-NC). Under this licence, you may copy and redistribute the material in any medium or format. You may also create and distribute modified versions of the work. This is on the condition that: you credit the author and do not use it, or any derivative works, for a commercial purpose. When reusing or sharing this work, ensure you make the licence terms clear to others by naming the licence and linking to the licence text. Where a work has been adapted, you should indicate that the work has been changed and describe those changes. Please seek permission from the copyright holder for uses of this work that are not included in this licence or permitted under UK Copyright Law.

Abstract

α-Tocopherol (vitamin E) is a powerful antioxidant within living cell membranes and whilst its antioxidant activity is well studied, its impact on lipids and lipid phase behaviour is less known. This work aims to elucidate how α-Tocopherol's antioxidant function is enhanced at low concentrations within living cell membranes, and how its function could be best harnessed in increasing the shelf life of food products. The interaction of α-Tocopherol with phosphatidycholine model membranes has been analysed using X-ray diffraction, solid-state NMR, differential scanning calorimetry and microscopy techniques.

Our work has found that α-Tocopherol behaves similarly to cholesterol in that it promotes fluidisation in parts of the membrane and rigidity in other parts. We show phase separation in giant unilamellar vesicles comprised of ternary mixtures of dipalmitylphosphatidylcholine, dioleoylphosphatdiylcholine and α-Tocopherol using fluorescence microscopy. This is a novel finding as prior to this, phase separation has only been associated to sterols or stanols. The implications of this are wide ranging, as in vivo it is likely α-Tocopherol is forming a liquid ordered type phase. From commercial perspective, replacing cholesterol with α-Tocopherol would be a healthier alternative.

We have also reported the curvature inducing impact of α-Tocopherol in unsaturated phosphatidylcholines. X-ray diffraction data shows that α-Tocopherol induces an inverse hexagonal phase, which coexists with an Im3m inverse bicontinuous cubic phase at specific concentrations with dioleoylphosphatdiylcholine. We also report the formation of the hexagonal close packed phase which previously has only been reported once. This phase forms at certain compositions of α-Tocopherol, triolein (oil) and dioleylphosphatidylethanolamine. The formation of these curved structures demonstrates α-Tocopherol's ability to minimise the water-oil interface as that is where oxidation reactions occur. Cubic phases are also extremely valuable for nutrient and drug delivery.

Acknowledgements

Firstly, I would like to thank my supervisors Prof. John M. Seddon, Prof. Rob V. Law and Dr Nick J. Brooks for their guidance over the course of this project. I would also like to thank Nestlé for the funding and Dr. Laurent Sagalowicz and Dr. Olivier Schafer for their advice.

I would also like to thank all the members of the Membrane Biophysics Group for their continuous support inside and outside of the lab. I am very grateful to the wonderful friends and co-workers for making the last four years enjoyable. Also, a specific thank you to other supervisors within Membrane Biophysics like Prof. Oscar Ces and Dr. Yuval Elani who always made time for extra support.

Another thanks to Dr. Marc Antoine Sani, from the University of Melbourne for his help in carrying out the dePaking protocol on NMR data.

Finally, I would like to thank my family and friends, without whose unwavering support this project would not have been possible.

Contents

Copyright Statement 2

Abstract 3

Acknowledgements 4

Contents 5

List of Figures 8

List of Abbreviations 12

Chapter 1: Introduction 13

1.1 The structure and function of α-Toc 13
1.2 Cell Membranes and Lipids 14
1.3 Lyotropic liquid crystals 15
1.3.1 Lamellar Phases 17
1.3.2 Cubic Phases 18
1.3.3 Bicontinuous cubic phases 18
1.3.4 Inverse micellar cubic phases 19
1.3.5 The 2D-Hexagonal Phase 20
1.3.6 Packing geometry and frustration in the hexagonal phase 20
1.4 Lateral stress profile and stored curvature elastic stress 21
1.5 The role of cholesterol and the liquid ordered phase 23
1.6 The interaction of α-Toc with lipids 24
1.7 The physical distribution of α-Toc in membranes 25
1.8 The impact of α-Toc on phospholipid phase behaviour 26
1.9 Aims 27

Chapter 2: Theory 28

2.1 X-Ray Diffraction 28
2.1.1 Braggs Law 29
2.1.2 Small Angle X-ray Scattering 30
2.1.3 Wide Angle X-ray Scattering 31
2.1.4 Synchrotron radiation 32
2.2 Nuclear Magnetic Resonance (NMR) 32
2.2.1 Solid-state NMR spectroscopy 34
2.2.2 Molecular Interactions 34
2.2.3 Shielding Interaction 35
2.2.4 ^{31}P Solid State NMR 36

2.2.5 ^{2}H Solid State NMR 37
2.3 Differential Scanning Calorimetry 38

Chapter 3: Methods and Materials 39

3.1 Materials 39
3.2 Sample preparation 39
3.2.1 Lipid films 39
3.2.2 Preparation of Giant Unilamellar Vesicles (GUVs) by electroformation 39
3.2.3 Preparation of Droplet Embedded Vesicles (DEVs) 40
3.3 DSC Experiments 40
3.4 Solid state-NMR Experiments 40
3.5 X- Ray Diffraction 41
3.6 Fluorescence Microscopy 41
3.7 Polarising Microscopy 42
3.8 Fluctuation Analysis 42

Chapter 4: DPPC interactions with α-Tocopherol 43

4.1 Introduction 43
4.2 Results 46
4.2.1 DSC of fully hydrated mixtures of DPPC and α-Toc 47
4.2.2 Small Angle X-ray Diffraction of DPPC and α-Toc 50
4.2.3 Wide Angle X-ray Diffraction of DPPC and α-Toc 53
4.2.4 Solid state ^{31}P NMR of α-Toc and DPPC 56
4.2.5 Fluorescence Microscopy of Giant Unilamellar Vesicles of α-Toc, DPPC and DOPC 59
4.2.6 Solid state ^{2}H NMR of α-Toc, d_{62}-DPPC and DOPC 63
4.3 Chapter Summary 68

Chapter 5: DOPC interactions with α-Tocopherol 69

5.1 Introduction 69
5.2 Results and discussion 72
5.2.1 X-Ray Diffraction Data of DOPC and α-Toc 72
5.2.2 Interactions of 0-32 mol% α-Toc with DOPC 74
5.2.3 Interactions of 32-38 mol% α-Toc with DOPC 82
5.2.4 Interactions of 38-80 mol% α-Toc with DOPC 86
5.2.5 Ternary Phase Diagram of α-Toc, DOPC and DPPC 88
5.6 Chapter Summary 93

Chapter 6: Triolein and DOPE interactions with α-Tocopherol 95

6.1 Introduction 95
6.2 Results and Discussion 98
6.2.1 SAXS of Triolein and DOPE 98
6.2.2 Interactions of Triolein, DOPE and Water studied by SAXS 100
6.2.3 Polarising Microscopy of Triolein and DOPE (in excess water) 103
6.2.4 SAXS of Triolein, DOPE, and α-Toc (excess water) 105
6.3 Chapter Summary 114

Chapter 7: Analysis of Droplet Embedded Vesicles 115

7.1 Introduction 115
7.2 Results and Discussion 118
7.2.1 Proof of formation of Droplet Embedded Vesicles (DEVs) and contact angle 118
7.2.2 The addition of α-Toc to DEVs 122
7.3 Chapter Summary 124

Chapter 8: Conclusions and Future Outlook 126

8.1 Key findings and future outlook of Chapter 4 126
8.2 Key findings and future outlook of Chapter 5 127
8.3 Key findings and future outlook of Chapter 6 and 7 128
8.4 Implications and limitations of work 129

Chapter 9: Bibliography 131

Chapter 10: Supplementary Information 141

10.1 Supplementary Information Chapter 4 141
10.2 Supplementary Information Chapter 5 143
10.3 Supplementary Information Chapter 6 147
10.4 Supplementary Information Chapter 7 149

List of Figures

Figure 1. 1 The chemical structure of α-Tocopherol (α-Toc) 13
Figure 1. 2 Cartoon representation of an amphiphilic molecules and a bilayer structure in an aqueous environment. 15
Figure 1. 3 Depiction of a normal micelle and an inverse micelle 16
Figure 1. 4 Lipid type based on their geometrical profile. Type 0 aggregates are flat whereas Type I and II are intrinsically curved. 17
Figure 1. 5 Cartoon of lamellar phases. 18
Figure 1. 6 Depiction of bicontinuous cubic phases: Pn3m, Ia3d and Im3m. 19
Figure 1. 7 Drawing of Fd3m phase formed of 8 large (light) and 16 smaller (dark) inverse micelles. 19
Figure 1. 8 Depiction of the normal hexagonal (H_I) and inverse hexagonal (H_{II}) phases. It comprises of infinitely long rods of lipid packed into a hexagonal lattice. 20
Figure 1. 9 Packing frustration in the H_{II} phase 21
Figure 1. 10 Image showing the origin of the various stresses along the membrane, the headgroups have a positive outward pressure, as do the chains, however the polar/non-polar interface has a negative inward pressure as the contact of the hydrocarbon chains with water is reduced. 22
Figure 1. 11 Image depicting the stored curvature elastic stress in a bilayer 23
Figure 1. 12 Cartoon depiction of the L_o phase with cholesterol depicted by the yellow ovals. The lipids associated to cholesterol are in an all trans state. 24
Figure 1. 13 Representation of three membrane locations for α-Toc 26

Figure 2. 1 Model of constructive X-rays diffracted from parallel planes with a repeat spacing of d ..29
Figure 2. 2 Model of the Ewald sphere 30
Figure 2. 3 Schematic of the generation of synchrotron radiation 32
Figure 2. 4 Illustration of the shielding interaction and its orientation dependence. 36
Figure 2. 5 Paked (grey) vs. depaked spectra of d-DMPC. 38

Figure 4. 1 Chemical structure of lipids: DPPC and DOPC and α-Toc 43
Figure 4. 2 Model of the modulated phase where the α-Toc composition is coupled to the bilayer curvature. 44
Figure 4. 3 The smoothed DSC thermograms of DPPC and DPPC with α-Toc mixtures in excess water 47
Figure 4. 4 The melting transition temperature (T_m) of DPPC at various compositions of α-Toc 48
Figure 4. 5 The change in molar entropy with the addition of α-Toc to DPPC, calculated from DSC thermograms. 49
Figure 4. 6 SAXS data of various compositions of α-Toc with DPPC in excess water at 25 °C 50
Figure 4. 7 Assignment of ripple diffraction peaks for DPPC at around 40-43 °C (near the pre-transition temperature), 4 mol% α-Toc and 10 mol% α-Toc with DPPC at 25 °C. 51
Figure 4. 8 The schematic for the ripple phase of DPPC illustrating the lattice parameters. 53
Figure 4. 9 The position of the peak centre arising from the WAXS peak, taken at various compositions of α-Toc with DPPC, and at various temperatures. 54
Figure 4. 10 The FWHM (full width half maximum) of the WAXS peak of various compositions of α-Toc with DPPC, and at various temperatures. 55
Figure 4. 11 ^{31}P NMR spectra of DPPC with various concentrations of α-Toc at 25 °C and 60 °C 56
Figure 4. 12 Geometrical representations of (A) an ellipsoid, (B) a bicelle in the x-y plane and (C) a bicelle in the x-y-z plane. 58
Figure 4. 13 Composition dependence of phase behaviour in GUVs of DPPC/DOPC/α-Toc is visualised using fluorescence microscopy at room temperature. Compositions of vesicles are A (4:8:3), B

(2:2:1), C (8:4:3), D (7:14:9), E (1:1:1), F (14:7:9). Phase separation can be visualised for compositions B, C, E and F. 60
Figure 4. 14 The original images (bright GUVs with dark backgrounds) have also been inverted (dark GUVs with a light background) to easily visualise membrane phase separation 60
Figure 4. 15 A series of images which are a consecutive image stack for a video. It is of a phase separated GUV of composition B (Figure 2.12) which is moving in the z-axis i.e., moving out of the plane of focus. Clear bright and dark domains can be visualised 62
Figure 4. 16 ^{2}H-solid state NMR powder patterns of DPPC, DPPC: DOPC (1:1) and DPPC: DOPC: α-Toc (2:2:1) in excess water at 25 ^{o}C (left) and 60 ^{O}C (right). The quadrupolar splitting of DPPC-d_{62} increases with the addition of α-Toc to the system. 64
Figure 4. 17 Paked vs. DePaked ^{2}H NMR spectra of DPPC at 60°C. The dePaked NMR peaks allow for the designation of ΔV_Q with respect to the segment position. 65
Figure 4. 18 Order profiles for DPPC: DOPC (1:1) and DPPC: DOPC: α-Toc (2:2:1) at 25 C (left) in excess water. Order profiles for DPPC, DPPC: DOPC (1:1) and DPPC: DOPC: α-Toc (2:2:1) at 60 ^{O}C in excess water 67
Figure 4. 19 The order profile for DPPC in d_{62}-DPPC: DOPC: CHOL (1:1:1) at 25 °C and 60 °C. 68

Figure 5. 1. Chemical structure of lipids: DPPC and DOPC, α-Toc and Cholesterol 69
Figure 5. 2. SAXS data of DOPC with α-Toc (molar amount of α-Toc given in figure) in excess water conditions at 25 ^{o}C. 73
Figure 5. 3. SAXS data of DOPC with 0-32 mol% α-Toc in excess water conditions at 25 ^{o}C. 74
Figure 5. 4 Temperature scan of 10 mol% α-Toc with DOPC in excess water. 74
Figure 5. 5. The change in d spacing of the L_α phase of DOPC by the addition of α-Toc 75
Figure 5. 6 Schematic showing a shift in decrease in d spacing as the a-Toc sit deeper into the bilayer. Hypothetically this could be this could be the conformational structure of 32 mol% α-Toc with DOPC 76
Figure 5. 7. The Umbrella model. (A) low cholesterol concentration, PC headgroups can pack together cover the hydrophobic cholesterol body (B) At high cholesterol concentration, headgroups of PCs work together to cover more cholesterol. (C) The frustum shaped cluster 77
Figure 5. 8 WAXS data of α-Toc with DOPC and FWHM of WAXS peak with respect to α-Toc composition (right) 78
Figure 5. 9 The bending rigidity of GUVs comprised of varying compositions of α-Toc with DOPC.. .80
Figure 5. 10 The membrane tension of GUVs comprised of varying compositions of α-Toc with DOPC. The line is a guide to the eye. 81
Figure 5. 11 SAXS data of 32-38 mol% a-Toc with DOPC in excess water.. 82
Figure 5. 12 SAXS temperature scan of 34 mol% α-Toc with DOPC. The initial reading was taken at 25 C before the sample was heated to 60C and subsequent readings were taken at lower temperatures. Labelled are the corresponding L_α peaks (black) and H_{II} peaks (grey). The L_α only co-exists with the H_{II} at lower temperatures. 83
Figure 5. 13 SAXS temperature scan of 38 mol% a-Toc with DOPC (excess water).. 84
Figure 5. 14 Observed reciprocal spacings vs. $\sqrt{(h^2 + k^2 + l^2)}$ derived from SAXS data, which depicts a perfectly linear plot, confirming the presence of the Im3m phase of 38 mol% α-Toc with DOPC (excess water) 85
Figure 5. 15 SAXS patterns of 38-80 mol% α-Toc with DOPC in excess water at 25 $^{\circ}$C 86
Figure 5. 16 lattice parameter calculation of the H_{II} and Im3m phases formed over the 38-80 mol% α-Toc with DOPC range. An increase in the lattice parameter is seen at 40 mol% for both H_{II} and Im3m phases. 87
Figure 5. 17 Ternary phase diagram of DPPC/DOPC/α-Toc showing SAXS data of A (5:11:4), B (2:2:1), C (11:5:4), D (5:9:6), E (7:7:6), F (9:5:6) DPPC: DOPC: α-Toc compositions in excess water at 25 °C. All these compositions exhibit a lamellar phase. 88

Figure 5. 18 The ternary phase diagram of DPPC/DOPC/α-Toc showing SAXS data of 40 mol% α-Toc with DPPC:DOPC ratio of G (1:5), H (1:2), I (1:1), J (2:1), K (3:1), L (5:1) in compositions of excess water at 25 °C 89
Figure 5. 19 SAXS temperature scan of composition (L) 40 mol% α-Toc with (5:1) DPPC:DOPC ratio. Two separate lamellar phases form which are less distinguishable at higher temperatures. 90
Figure 5. 20 The ternary phase diagram of DPPC/DOPC/α-Toc showing SAXS data of 50 mol% α-Toc with DPPC:DOPC ratio of M (4:1), N (1:1), O (1:4) in compositions of excess water at 25 °C. 92
Figure 5. 21 The ternary phase diagram of DPPC/DOPC/α-Toc based on SAXS data in compositions of excess water at 25 °C. 93

Figure 6. 1 Chemical structures of Triolein, DOPE and α-Toc 97
Figure 6. 2 SAXS plots of Triolein with DOPE (without water), showing phase separation of Triolein from the H_{II} phase of DOPE. 98
Figure 6. 3 The lattice parameter of the H_{II} phase with respect to percentage DOPE with triolein....99
Figure 6. 4 The proposed lamellar TAG assembly model of triolein molecules where each structure (blue, grey and black) is representative of a triolein molecule 100
Figure 6. 5 Ternary phase diagrams of Triolein, Water and DOPE (wt%) with corresponding SAXS patterns depicting H_{II} phases. 101
Figure 6. 6 The lattice parameter of the H_{II} phase at compositions I (2:1:2), H (2:1:1.3) and G (2:1:0.8) (Triolein: Water: DOPE).....103
Figure 6. 7 Polarising microscopy images of DOPE with Triolein in excess water at 25°C. 104
Figure 6.8 SAXS profiles of compositions of α-Toc, DOPE and Triolein (excess water, at 25 °C) with compositions depicted in ternary phase diagram. 105
Figure 6. 9 Proof of the formation of the Fd3m phase from the additional Bragg peaks 106
Figure 6. 10 Face centered cubic (fcc) and hexagonal close packed (hcp) conformations with a packing fraction of 0.74. 107
Figure 6. 11 SAXS profiles of compositions of α-Toc, DOPE and Triolein (excess water, at 25 °C) with compositions depicted in ternary phase diagram (top). The proportion of α-Toc is constant at 30 mol% with varying amounts of DOPE: Triolein, (1) 70:0, (2) 67.5:2.5, (3) 62.5:7.5, (4) 60:10, (5) 57.5: 12.5, (6) 49:21, (7) 35:35, (8) 22:48, (9) 8:62 (mol%).....108
Figure 6. 12 Proposed models for DOPE alone, DOPE and dodecane (could depict any hydrocarbon) and DOPE and α-Toc 109
Figure 6. 13 SAXS profiles of compositions of α-Toc, DOPE and Triolein (excess water, at 25 °C) with compositions depicted in ternary phase diagram (top). The proportion of α-Toc is constant at 50 mol% with varying amounts of DOPE: Triolein. 111
Figure 6. 14 The schematic structure of the 3-D hexagonal inverse micellar structure. The spheres represent the polar regions (water cores plus lipid headgroups) and the remaining volume is filled by hydrophobic regions (lipid chains and triolein). 112
Figure 6. 15 The ternary phase diagram of DOPE: triolein: α-Toc (in excess water 114

Figure 7. 1 Different mechanisms favouring the formation of the nucleation site. 1) local bilayer deformation caused by curvature results in the accumulation of triglyceride molecules. 2) the presence of curvature inducing proteins or molecules can cause defects within the bilayer to form a nucleation site 3) triglyceride aggregates in locations with favourable interactions with proteins or lipids. 116
Figure 7. 2 Illustration of dewetting transitions. A liquid deposited on a surface can wet the surface or de-wet and form a droplet with a specific contact angle (Θ). The substrate is indicative of the lipid bilayer, and the liquid is the triglyceride encapsulated within a monolayer (when it forms a droplet). 117

Figure 7. 3 1) In vivo representation of lipid droplet formation in ER membranes, accumulation of oil molecules eventually results in the lipid droplet budding from the membrane. 2) In vitro this process can be replicated in GUVs to form DEVs.....119
Figure 7. 4 Brightfield image showing proof of formation of DEVs with arrows pointing at the oil droplet. The GUVs are comprised solely of DOPC, and the oil encapsulated is triolein. 119
Figure 7. 5 Brightfield images of DEVs made from varying compositions of DOPC: DOPE with triolein. The red circles are likely indicative of egressed lipid droplets. Scale bar is 10 μm (applies to all three images).....120
Figure 7. 6 Contact angle between the triolein lipid droplet and GUV within DEVs comprised of DOPC and DOPE mixtures. The error bar is indicative of the standard error of the mean calculated from three DEVs.....121
Figure 7. 7 Series of images depicting a budding event of a lipid droplet from a DEV. The DEV is comprised 5 mol% α-Toc with DOPC and triolein.....123
Figure 7. 8 Series of images depicting a budding event of a lipid droplet from a DEV. As the DEV egresses, the density of both the lipid droplet and the GUV changes meaning they are no longer in focus. The DEV is comprised 1 mol% α-Toc with DOPC: DOPE (1:1) and triolein.....124

List of Abbreviations

α-Toc α-Tocopherol

B_0 applied external magnetic field

Chol cholesterol

CSA chemical shift anisotropy

DEV droplet embedded vesicle

DOPC dioleoylphosphatdiylcholine

DPPC dipalmitylphosphatidylcholine

DOPE dioleylphosphatidylethanolamine

DSC differential scanning calorimetry

FWHM Full width at half maximum peak height

GUV Giant unilamellar vesicle

H_I Hexagonal phase

H_{II} Inverse hexagonal phase

L_α fluid lamellar phase

L_β gel lamellar phase

$L_{\beta'}$ tilted gel lamellar phase

L_o liquid ordered lamellar phase

NMR nuclear magnetic resonance

$P_{\beta'}$ ripple lamellar phase

SAXS small angle x-ray scattering

ss-NMR solid state nuclear magnetic resonance

T_m melting temperature

WAXS wide angle x-ray scattering

Introduction

1.1 The structure and function of α-Tocopherol

Vitamin E is the collective term for a group of hydrophilic compounds with distinct antioxidant properties essential for health. They are divided into a family of tocopherols (saturated side chain) and tocotrienols (unsaturated side chain) and are characterised by the same basic chemical structure of a long isoprenoid side chain attached at the 2-position of a 6-chromanol ring (Figure 1.1). There are eight naturally occurring forms of vitamin E of which alpha- and gamma- tocopherol are the most prominent. It is alpha-tocopherol (α-Toc) which is retained in the human body and resides mainly in Golgi membranes and lysosomes. [1] [2]

Two functions of α-Toc in cells are recognised: a) the primary function is to act as an antioxidant to prevent free radical damage to cells and more specifically to unsaturated lipids. Oxidation reactions within cells form reactive oxygen species which causes degradation. α-Toc functions as an antioxidant by intercepting free radicals and delocalising the unpaired electron into the ring system (Figure 1.1). The molecular structure of α-Toc consists of a chromanol head group, methylated at three positions on the benzene ring and a 16-carbon saturated phytyl chain attached. The hydroxyl group is responsible for the free radical scavenging activity therefore must be oriented towards the reactive oxygen species. b) the secondary function is to stabilise the structure of membranes or self-assembled lipids by forming complexes. [3] [4]

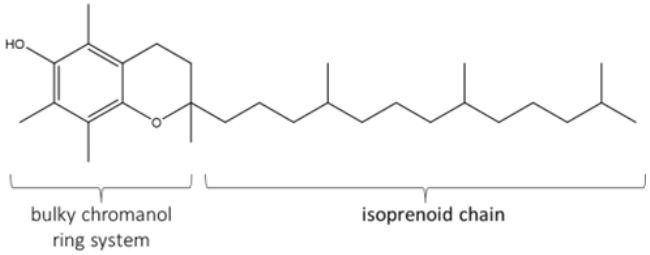


Figure 1. 1 The chemical structure of α-Tocopherol (α-Toc)

Although the antioxidant function of α-Toc is well studied, the structural impact on biological systems is still unclear. There is considerable evidence of the formation of complexes between α-Toc and the products of membrane lipid hydrolysis such as lysophospholipids and free fatty acids. These complexes prevent the detergent like actions of hydrolytic products on the membrane. The function of α-Toc however is not limited to protecting membranes, it has also been associated with inhibiting cell proliferation, impacting the rate of transcription of genes and platelet aggregation. [3 5 6]

From a commercial perspective, α-Toc is of great interest to pharmaceutical, skincare and food formulation industries. The oxidation of lipids, particularly unsaturated lipids such as omega-3, causes food products to become rancid. The incorporation of α-Toc may increase the shelf life; however, to effectively harness its antioxidant function, more information is required on its location and orientation within lipid membranes and self-assembled structures. In human cells, α-Toc makes up approximately 1.5% of the lipids in membranes and its preferential mode of action, alongside its localisation and impact within a lipid matrix, remains to be understood. [5 7]

1.2 Cell Membranes and Lipids

The cell plasma membrane is a semi-permeable barrier which separates the intracellular environment from the extra-cellular. It is comprised of a complex mixture of phospholipids, glycolipids, cholesterol and proteins and these compositions can be tuned to the required properties and structure of the membrane. Initially the fluid mosaic model was proposed by Singer and Nicholson to describe the membrane as a blend of lipids with embedded proteins arranged in a bilayer structure. It is now more widely believed that lipids can segregate into ‘domains’ which allows for finer tuning of the local environment to control cellular processes. These domains are generally regarded as more heterogeneous phospholipid domains. [8 9]

Phospholipids account for most of the lipids in the membrane and assemble into a bilayer structure which is driven by the hydrophobic effect. They are amphiphilic molecules with hydrophilic headgroups and hydrophobic tails, which causes them to spontaneously arrange to protect the

unfavourable interaction with the chains in the presence of water (Figure 1.2). Although the lipid portion of membranes is thought to be inert, there is a variety of different lipids which are unevenly distributed. Each leaflet is also not equivalent to the other, as each side is enriched with different lipids, these lipids are able to 'flip-flop' across the bilayer, but at a relatively slow rate (half-times of minutes to hours). [10] [11]

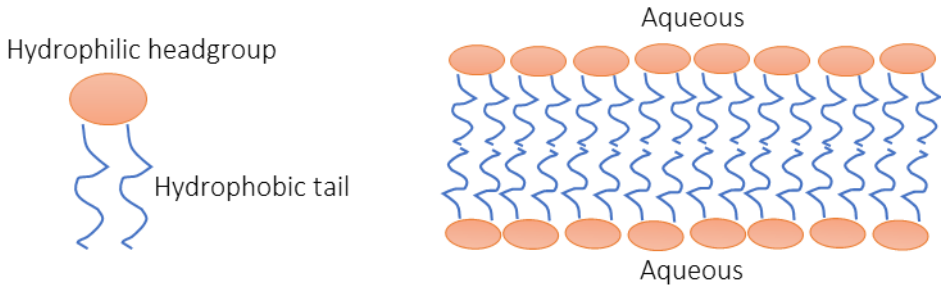


Figure 1. 2 Cartoon representation of an amphiphilic molecules such as a phospholipid (left) and a bilayer structure in an aqueous environment. This arrangement allows for hydrophobic tails to be shielded from the water whereas the hydrophilic headgroups are interacting with water.

1.3 Lyotropic liquid crystals

Liquid crystals are a fourth state of matter which are intermediate between liquids and solids. Two types exist: lyotropic and thermotropic. Thermotropic liquid crystals undergo phase transitions with varying temperature and pressure, whereas lyotropic crystals experience phase transitions depending on temperature, pressure, and/or solvent concentration. The present work focuses on lyotropic liquid crystals, which require a suitable solvent to form with long range periodicity and short-range disorder.

As these lyotropic liquid crystals are formed of amphiphilic lipid molecules, the inherent structural properties of the lipid dictate the geometry of the phase adopted. These phases may adopt one-dimensional order (lamellar sheets), two-dimensional order (hexagonally packed cylinders) or three-dimensional order (cubic phases). Phospholipids can have various headgroup structures, which can be charged or uncharged, and chains of varying number, length and degree of saturation. As a result, the nature of the headgroups and chains can significantly impact the phase behaviour of the lipid aggregate. For example, if the solvent added is water, then the lipid molecules will arrange themselves at the air-water interface. At certain lipid concentrations, these molecules will arrange into micelles

at the critical micelle concentration (CMC). Whether the system produces normal or inverse micelles is dependent on the balance of forces arising from the water content and headgroup or chain interactions (Figure 1.3). At low lipid concentrations these micelles will disperse within a solution, however at higher concentrations they will begin to aggregate and pack into liquid crystal mesophases. [12] [13]

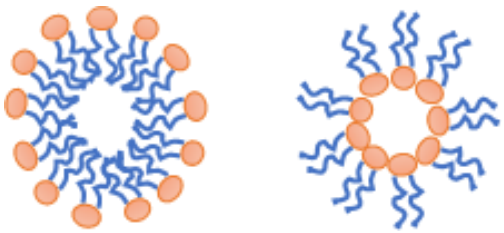


Figure 1. 3 Depiction of a normal micelle (left) and an inverse micelle (right).

Micelles have extremely high curvature and so their formation is based on the geometrical profile of the lipid. According to their geometrical profile, lipids can be classified into three types. These types are based on the cross-sectional areas of the headgroups with respect to the cross-sectional areas of the tail region. Type 0 lipids have a cylindrical geometric profile because the cross-sectional area of the headgroups and chain regions is almost equivalent. These cylinders can arrange next to each other without any resulting curvature. Type I lipids have larger headgroup areas than chain regions therefore curve away from the water interface whereas Type II lipids have smaller headgroup constituents therefore curve towards the water interface (Figure 1.4). In this work the main lipids which were studied are dipalmitoyl-phosphatidylcholine (DPPC) and 1,2-dioleoyl-sn-glycero-3-phosphocholine (DOPC), which are Type 0 lipids and therefore do not possess intrinsic tendency for curvature. 1,2-dioleoyl-sn-glycero-3-phosphoethanolamine (DOPE) was also studied and is classified as Type II and tends to curve towards the water interface, resulting in the formation of inverse mesophases. [14] [15]

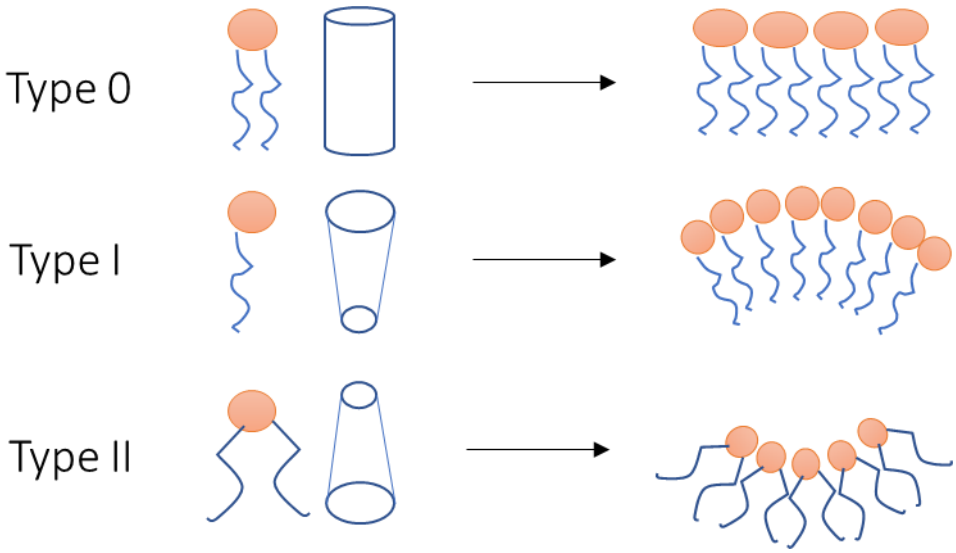


Figure 1. 4 Lipid type based on their geometrical profile. Type 0 aggregates are flat whereas Type I and II are intrinsically curved. Image adapted from Elani [15]

1.3.1 Lamellar Phases

The lyotropic liquid crystal mesophase with no overall net curvature is the lamellar phase. Lipids of biological membranes self-assemble into lamellar bilayers and are arranged as an infinite stack of bilayers separated by water. The lamellar phase itself can be subdivided depending on the hydrocarbon chain flexibility of the lipid. At low temperatures, most chain saturated phospholipids are in the crystalline phase (L_c) where the chains are headgroups are fixed in position and highly ordered. Most unsaturated lipids on the other hand are in the fluid lamellar phase (L_α), which is the most disordered phase, and the lipid chains are 'molten'. The lipid molecules exhibit rapid lateral diffusion, axial rotation, and trans-gauche isomerisation of chains (Figure 1.5).

The untilted lamellar gel phase (L_β) is an intermediate phase with the chains extended in an all-trans state and the molecules exhibiting long-axis rotation but limited or no lateral motion. This phase however is varied with slightly different properties of the polymorphs. In the tilted gel phase ($L_{\beta'}$) the molecules are tilted approximately 30° with respect to the bilayer normal. The interdigitated phase ($L_{\beta I}$) comprises of lipids with a long chain and a short chain and arranged in an interdigitated configuration. The ripple phase ($P_{\beta'}$) is also usually tilted with respect to the bilayer normal and has a periodic undulation along the plane (Figure 1.5). A change in temperature or pressure induces changes

from one lamellar phase to another. Above the melting temperature (T_m), the phospholipid will 'melt' from a L_β phase to an L_α phase, if the lipid is in an $L_{\beta'}$ phase it will exhibit a pre-transition to the $P_{\beta'}$ phase before transitioning to L_α. Other lamellar phases also exist, such as the liquid ordered (L_o) phase, which is discussed in a further section below. [12]

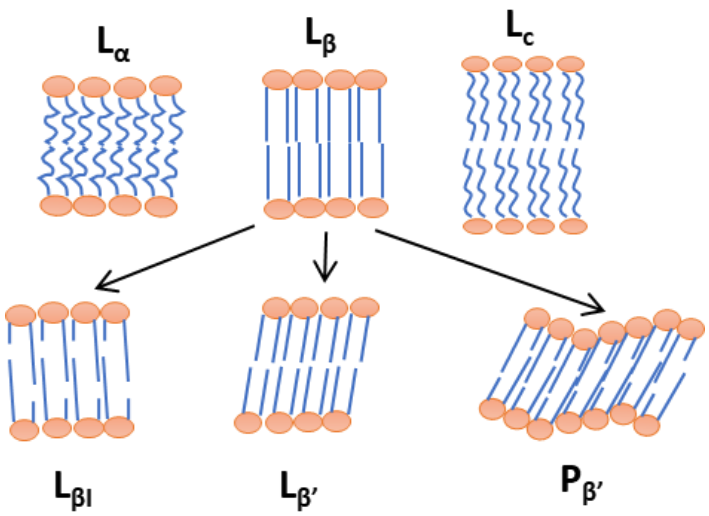


Figure 1. 5 Cartoon of lamellar phases. The three classifications are: fluid lamellar (L_α), gel lamellar (L_β) and crystalline lamellar (L_c). The L_β phase can exhibit in polymorphs of interdigitated ($L_{\beta I}$), tilted ($L_{\beta'}$) and rippled phases ($P_{\beta'}$).

1.3.2 Curved Lipid Phases

Type II lipids distort away from a lamellar phase because of the large acyl chain splay and small headgroups. These lipids tend to form inverse phases such as bicontinuous cubic phases which can be described as a continuous bilayer draped on a periodic minimal surface. If the preferred interfacial curvature is even greater, then the inverse hexagonal phase (H_{II}) may form (discussed in detail in a further section). Beyond this, quasi-spherical inverse micelles may form, which aggregate into inverse micellar cubic phases such as Fd3m.

1.3.3 Bicontinuous cubic phases

Inverse bicontinuous cubic phases are comprised of a single curved bilayer which separates two continuous networks of water. The three most common ones are: diamond (belonging to the Pn3m space group), primitive (space group Im3m) and gyroid (space group Ia3d).

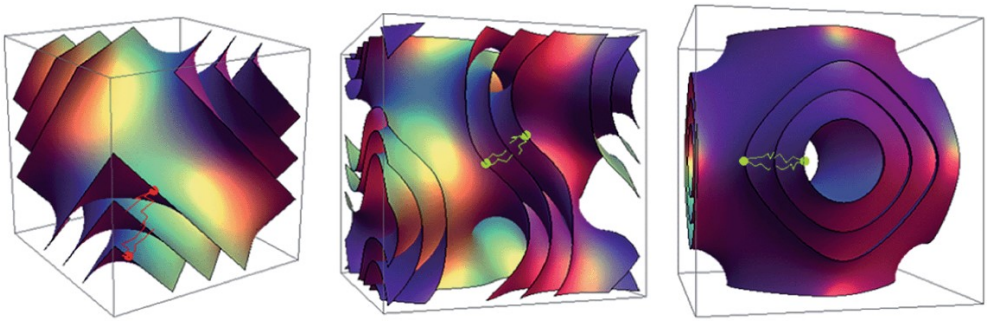


Figure 1. 6 Depiction of bicontinuous cubic phases: Pn3m, Ia3d and Im3m respectively. Figure taken from Tyler et al.[16]

1.3.4 Inverse micellar cubic phases

Inverse micellar cubic phases comprise of inverse micelles arranged in a cubic lattice. The three well established examples are Fd3m, Fm3m and Pm3n. The Fd3m phase which comprises of two different-sized inverse micelles arranged on a face centred cubic lattice. Each unit cell contains 8 larger inverse micelles arranged tetrahedrally on a diamond lattice and 16 smaller ones grouped in tetrahedral clusters. Formation of this phase usually requires the presence of at least two lipid components, one of which is weakly hydrophilic (e.g., diglyceride, fatty acid). This allows for the formation of two different sized micelles. It is speculated that the less hydrophilic species will locate in the smaller, more strongly negatively curved inverse micelles. [17] [18]

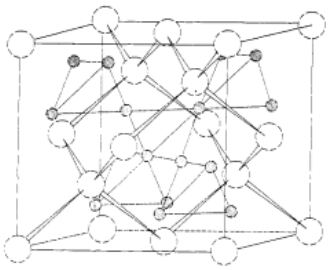


Figure 1.7 Drawing of Fd3m phase formed of 8 large (light) and 16 smaller (dark) inverse micelles. The spheres represent the water cores, the remaining volume is filled by fluid hydrocarbon chains of the lipid. Taken from Seddon et al.[18]

An inverse micellar 3-D hexagonal phase with an hcp arrangement has been previously reported. This phase is explored in further detail in Chapter 6. [19]

1.3.5 The 2D-Hexagonal Phase

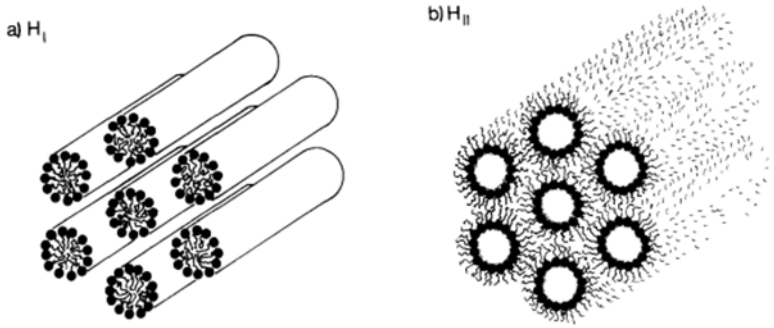


Figure 1. 8 Depiction of the normal hexagonal (H_I) and inverse hexagonal (H_{II}) phases. It comprises of infinitely long rods of lipid packed into a hexagonal lattice. Taken from Seddon et al. [20]

The 2-D hexagonal phase forms when the desire for curvature of the lipids is greater than that of the continuous phase, however not strong enough to form spherical micelles. Spherical micelles are limited in their expansion as there could be a void in the centre of the sphere. Longer acyl chains therefore distort from this into lower curvature structures such as cylindrical micelles which arrange into a hexagonal formation to form the hexagonal phase (Figure 1.8). This conformation can either be H_I (normal) with headgroups facing outwards toward the bulk, or H_{II} (inverse) with headgroups facing inward. [20] [21]

1.3.6 Packing geometry and frustration in the hexagonal phase

Although a more curved hexagonal phase alleviates some of the stored curvature elastic stress of the lamellar phase (see section 1.4), there remains a chain frustration in the H_{II} phase. This is because, at the boundaries of the cylindrical rods there is a potential void within the structure (Figure 1.9). To fill this void, the hydrocarbon chains may extend away from their optimal conformational state, which introduces a packing frustration. It is theorised that this may be partially alleviated if the cylinders adopted a hexagonal cross-section as opposed to a circular one. [17] [20]

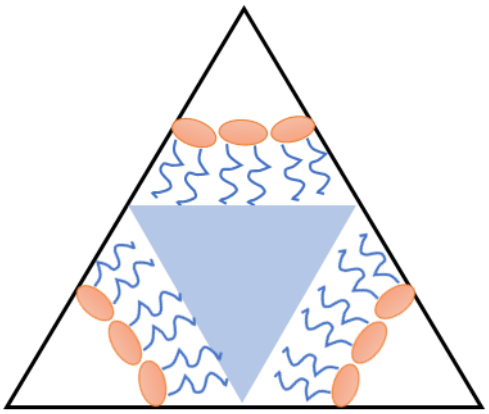


Figure 1. 9 Packing frustration in the H_{II} phase. Adapted from Seddon et al.[20]

1.4 Lateral stress profile and stored curvature elastic stress

Lamellar phases are successful in shielding the acyl chains from water, driven by the hydrophobic effect. However, to understand the other mesophases formed, it is important to understand the amphiphile's desire for curvature. This can be explained by looking at the lateral stress profile. Type I and II lipids (Figure 1.4) may be present in a flat bilayer and therefore impart the desire for interfacial curvature because of the non-uniform distribution of the lateral stresses. These lateral stresses vary per lipid but are governed by forces such as ionic attraction/repulsion, hydrogen bonding and steric interactions (Figure 1.10). [22]

To understand the lateral pressure profile p(z) parallel to the bilayer, the intermolecular interactions within a bilayer must be looked at (Figure 1.10). At the air-water interface there is an attractive lateral stress due to the hydrophobic effect minimising the contact of the alkyl chains to the water. This is counteracted by unfavourable steric and electrostatic interactions of the headgroups, which is partially offset by hydrogen bonding between headgroups. In the chain region, there are also unfavourable steric repulsions caused by trans-gauche isomerisation of the acyl chains, partially offset by favourable Van der Waals attractions.

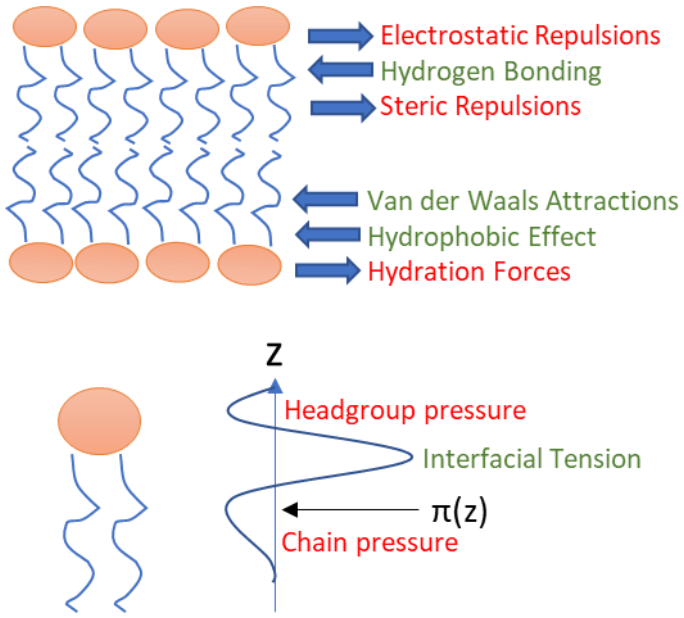


Figure 1. 1 Image showing the origin of the various stresses along the membrane, the headgroups have a positive outward pressure, as do the chains, however the polar/non-polar interface has a negative inward pressure as the contact of the hydrocarbon chains with water is reduced. Picture adapted from Ces et al. [14]

In a monolayer the overall net lateral tension at equilibrium is zero. This is represented in the Equation 1.1:

$$\int p(z)\, dz = 0 \qquad \text{Equation 1.1}$$

The torque (τ) of the monolayer is given by the first moment of the pressure profile in Equation 1.2, where κ is the bending modulus associated with the mean curvature and C_0 is the spontaneous curvature:

$$\tau = \int z.p(z)dz = \kappa c_0 \qquad \text{Equation 1.2}$$

For type I and II lipids the torque is non-zero meaning there is an imbalance of the forces between the headgroup and chain regions. As a result, the monolayers will want to either curve away or towards the aqueous phase however are unable to due to the stacking of the monolayers. This leads to an important biophysical property referred to as stored curvature elastic stress.

Each monolayer is forced to confine to a bilayer structure to minimise the free energy. If the monolayers did adopt their preferred curvature the resulting voids and the hydrophobic effect would be too energetically costly (Figure 1.9). Consequently, a packing frustration is created. This curvature

elastic stress plays an important role in modulating the shape of cell membranes therefore impacts lipid protein interactions and signalling events. The more Type I and II lipids present, the higher the curvature elastic stress. [23] [24] [14] [25]

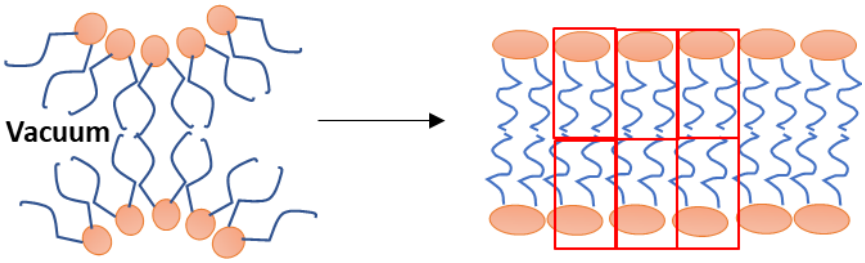


Figure 1. 11 Image depicting the stored curvature elastic stress in a bilayer. If the monolayer adopts its desired curvature, then the voids created would be energetically costly. Picture adapted from Ces et al. [14]

1.5 The role of cholesterol and the liquid ordered phase

Despite cholesterol's bad reputation in healthcare, it is a vital component of cell membranes. In eukaryote cell membranes it comprises of up to 50 mol% of the lipid content and depletion of cholesterol could lead to cell death. As a hydrophobic molecule, it inserts itself between lipid molecules in the cell membrane and maintains the fluidity by acting as a phase moderator. If cholesterol is incorporated into an L_β phase it fluidises the bilayer by disrupting the chain packing. On the other hand, if inserted into an L_α phase it results in ordering of the bilayer as cholesterol buries itself within the hydrocarbon chains of the lipid and forces them into an all-trans state to maximise the Van der Waals interactions and minimise sterically-unfavourable bent chain conformers. [26] [27]

At the correct compositions the liquid ordered phase (L_o) is formed, which contains characteristics of both the L_α phase and the L_β phase. It has high chain conformational order as in the L_β phase, but rapid lateral diffusion and long axis rotation as in the L_α phase (Figure 1.12). It is the L_o phase which is hypothesised to form lipid rafts in cell membranes whilst the rest of the membrane remains L_α. The lipid raft theory hypothesises that membranes contain microdomains with increased chain order, which specific proteins and lipids associate to. These rafts are hypothesised to serve as a site for cell signalling processes. In artificial giant unilamellar membranes, cholesterol promotes phase separation

of domains in mixtures of saturated and unsaturated lipids, by preferentially associating with the saturated lipids, forming an L_o phase which segregates from the L_α phase. [28] [12]

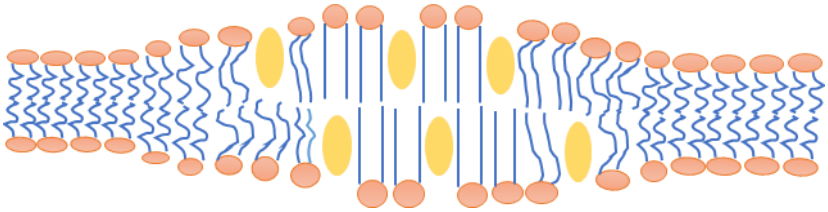


Figure 1. 12 Cartoon depiction of the L_o phase, within a L_d phase, with cholesterol depicted by the yellow ovals. The lipids associated to cholesterol are in an all trans state.

1.6 The interaction of α-Toc with lipids

The chemical reactivity of α-Toc is dependent on its vicinity to reactive oxygen species. This interaction is very likely facilitated by surface active species such as lipids as they would alter the physical location of tocopherols. Koga and Terao et al.[29] were one of the first to report the influence of phospholipids in the radical scavenging activity of vitamin E. It was found that phospholipids enhanced the accessibility of vitamin E toward chain initiating radicals in an aqueous microenvironment within bulk oil. This is because bulk oil contains trace water, which phospholipids can self-assemble around to form structures such as inverse micelles. The exact structure is dependent on the type of phospholipid; however, α-Toc can incorporate within these microstructures, and therefore due to a change in the micro-environment, orientate towards free-radicals. It should be noted that the structure of α-Toc is somewhat amphiphilic, (Figure 1.1), with a bulky, slightly polar chromanol ring system and a long acyl chain. [30] [31]

The effect of phospholipids on antioxidant reactivity can however vary depending on the environment. Chen et al.[32] found that association colloids formed of DOPC increased antioxidant activity at concentrations of 10 µm α-Toc in stripped soybean oil. However, at higher concentrations of α-Toc (around 100 µm), the opposite impact was seen. The presence of DOPC reduced the antioxidant activity of α-Toc at higher concentrations; the reason behind this is unclear however could be attributed to α-Toc reducing transition metals to a more prooxidative state at higher concentrations. The negatively charged interface formed by DOPC phosphate groups could attract these transition

metals. The balance of the prooxidant and antioxidant effect is dependent on the environment of α-Toc therefore it is important to understand its interactions with lipids. [30] [33] [34] [35]

1.7 The physical distribution of α-Toc in membranes

The physical interaction between phospholipids and α-Toc remains to be understood, to gain clarity on their chemical synergy. Salgado et al. demonstrated that α-Toc stabilised and formed bilayer structures of single chain or very asymmetric phospholipids, where they would otherwise form micelles.[36] Since then, several experimental and modelling studies have shown that the location of α-Toc within membranes enhances their efficiency. Three main vertical locations of α-Toc have been hypothesised; one with the chromanol moiety near the lipid headgroups, one with it close to the carbonyl groups, and one with the moiety deeper within the membrane and close to the acyl chains (Figure 1.13). [37] [38] [39]

Earlier work found that α-Toc was found closer to the lipid-aqueous interface in DMPC bilayers (location a, Figure 1.13), however this was disputed by Marquardt et al.[38] who used neutron diffraction, nuclear magnetic resonance (NMR) and ultraviolet (UV) spectroscopy to show that α-Toc resides deep within the membrane (location c, Figure 1.13). The consensus, through various studies using model membranes, is that α-Toc resides higher in the bilayer with its chain parallel to the acyl chain (position a) in most saturated bilayers. The location within unsaturated bilayers however tends to vary. In addition to its vertical location, the lateral segregation of α-Toc has also been questioned. It is often hypothesised that α-Toc has an affinity to polyunsaturated fatty acids (PUFA's) and are therefore segregated into the fluid zone of a lamellar phase bilayer. This was first suggested by Diplock et al.[40] based on molecular models and the conformation of multiple double bonds on PUFA chains being able to accommodate the methyl groups on the isoprenoid chain of α-Toc. However, the experimental support for this was sparse. Further to this, Kagan et al.[7] and Urano et al.[41] have provided evidence for the formation of complexes between α-Toc and free unsaturated fatty acids using NMR studies. [42] [43]

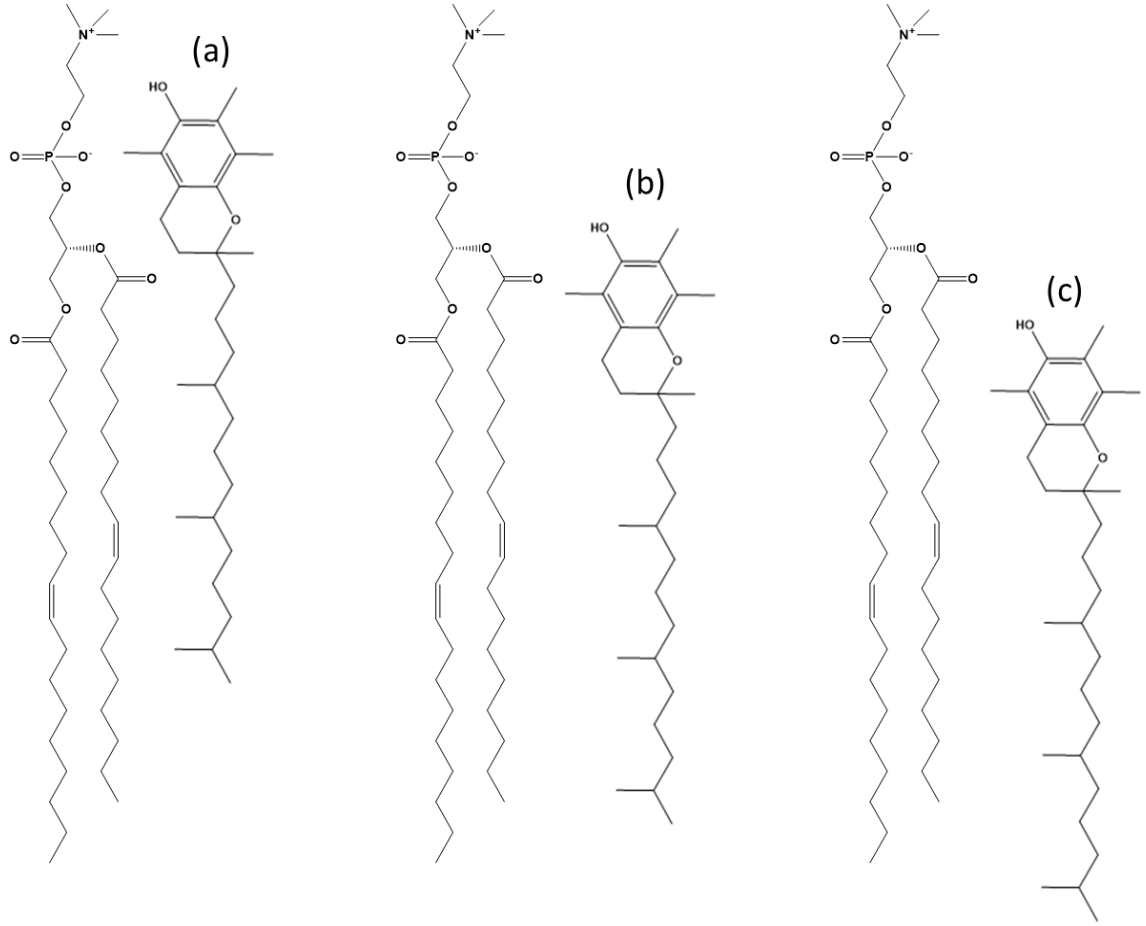


Figure 1. 13 Representation of three membrane locations for α-Toc described by Afri et al.[44] Adapted from Atkinson et al. DOPC is used as a representative lipid to depict the relative positions of α-Toc.[30]

1.8 The impact of α-Toc on phospholipid phase behaviour

Many studies have shown that α-Toc influences the phase behaviour of phospholipids. In aqueous dispersions of dimyristoylphosphatidylcholine (DMPC), it was shown to decrease the L_β to L_α phase transition temperature. Other studies with unsaturated phospholipids showed little effect at compositions of up to 10 mol% α-Toc. At higher compositions, the addition of α-Toc can lead to the formation of inverse mesophases. Wang et al. have[3] reported the formation of H_{II} and Pn3m structures in distearoylphosphatidylethanolamine (PE) induced by α-Toc whereas H_{II} and lamellar phase coexistence can be seen with dilauorylphosphatidylethanolamine (DLPE). The impact of α-Toc phase behaviour on phospholipids is reviewed and explored in further chapters, however it is important to note the significant impact the antioxidant can have on altering the mesophase structure of lipids. [5 45]

1.9 Aims

The aims of this work were to gain a better understanding of the interactions between α-Toc and phospholipids. Although the antioxidant mechanism is well known, α-Toc's interaction with lipids is less well understood. This work aims to elucidate the change in phase behaviour of lipids upon the addition of α-Toc, to better harness its capabilities. A potent antioxidant such as α-Toc is of interest to the skincare, pharmaceutical and food industries. To better understand its mechanism of action, to better design formulations, its fundamental interaction with lipids, and its ability to alter micro-environments, must be analysed. This work used X-ray diffraction, solid state nuclear magnetic resonance (ss-NMR) and other biophysical techniques (discussed in detail below) to probe the interaction between phospholipids and α-Toc.

The initial aim of this thesis was to analyse the interactions between phospholipids: DPPC and DOPC with α-Toc (in an excess of water), for binary and tertiary mixtures. A well-studied system in the literature is the cholesterol interactions with a saturated and unsaturated lipid (such as DPPC and DOPC). This work draws comparisons between cholesterol and α-Toc to identify if α-Toc may also be forming a phase like the L_o phase.

Further to this, the ternary lipid system of triolein, DOPE and α-Toc was explored. Triolein is an unsaturated triglyceride, widespread in foods, which is prone to oxidation reactions. DOPE is also a component of food systems such as lecithin. Self-assembled structures formed by DOPE and antioxidants such as α-Toc may help to delay these reactions and therefore increase the shelf life of food products. The aim was to analyse the interactions initially with X-ray diffraction to gauge the phase behaviour within these systems, and to complement this, microscopy techniques were also used.

Theory

2.1 X-Ray Diffraction

One of the main techniques used to probe lipid systems in this body of work is X-ray diffraction. X-rays have a wavelength (λ) of approximately 1.5 Å, which is of the same magnitude of the spacing between atoms in biological matter. The analysis of the angular dependence of the diffracted X-rays provides structural information of the regular repetitions of biological material.

The atomic scattering factor of an atom is proportional to its number of electrons. As biological and soft matter systems are made predominantly of low atomic number atoms (C, H, O and N), the scattering intensity is rather weak. The molecular aggregates which make up biological systems are also large, which means that X-rays scatter at smaller angles. Consequently, specialised equipment is required to emit sufficient flux of X-rays and to detect the weak signals. X-ray beam optics produce a highly monochromatic and collimated beam on the sample. The X-ray detector records the angular position of the scattered rays, in 1-D or 2-D. The diffracted X-rays at low 2θ values are referred to as small-angle X-ray scattering (SAXS), and those at large 2θ values are wide-angle X-ray scattering (WAXS). SAXS occurs at scattering angles of $2\theta \leq 2°$, and WAXS is at scattering angles of approx. $5 \leq 2\theta \leq 60°$.

Lyotropic liquid crystals possess long range periodicity and short-range disorder. Theoretically the repeating structures should result in sharp, resolution-limited diffraction peaks from the sample; however the peaks in the resulting pattern are broadened by processes such as thermal disorder and small domain (crystallite) size.[46 47]

2.1.1 Braggs Law

For diffraction to occur the diffracted X-rays must be in phase with each other i.e., constructively interfere. This means the path difference between X-rays diffracted from planes which are parallel to one another must be an integral number of wavelengths (Figure 2.1). This is defined by Braggs law (Equation 2.1).

$$n\lambda = 2d\sin\theta \quad \text{Equation 2.1}$$

where n is the integer order of reflection plane, λ is the wavelength of X-ray radiation, d is the repeat distance between planes in a lattice and θ is the angle at which scattering occurs.

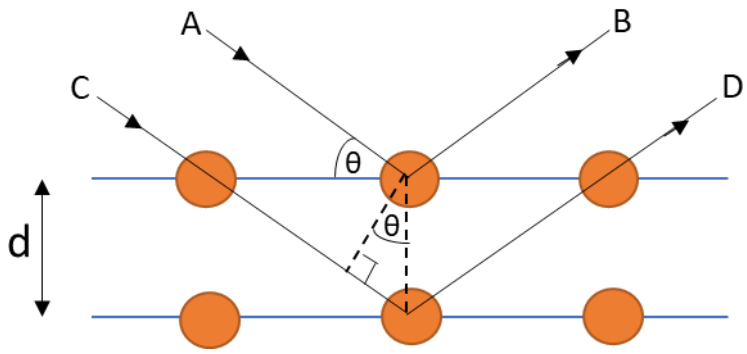


Figure 2.1 Model of constructive X-rays diffracted from parallel planes with a repeat spacing of d.

If the path difference between AB and CD is an integral number of wavelengths, then the constructive interference results in a Bragg peak. However, X-ray diffraction of lipid mesophases results in the diffracted rings rather than peaks. This is because mesophases e.g., bilayer stacks can be envisaged as mini crystals each randomly oriented at slightly differing angles to the incoming beams. Every set of planes will be capable of diffraction in each mini crystal, however as the crystals are oriented randomly, therefore the net result of diffraction will be equivalent to rotating a crystal about all possible axes. According to Braggs law, for a given peak, θ must be constant between the X-ray beam and the plane; this corresponds to rotation of the planes around the X-ray beam.

A given Bragg reflection will follow a path defined by a cone, making a constant angle of 2θ to the incoming radiation. This will hit the detector to give a circle centred on the axis of the incoming

radiation. The difference in spacing between these circles can be correlated to the known spacing of lyotropic liquid crystals. The circular patterns are radially converted to linear intensity plots, and the squared ratio of the peaks can be correlated to a phase.

Crystals including lyotropic liquid crystals can be regarded as the convolution of a unit cell and a lattice. A full description of the lattices and their symmetries can be provided by Guinier et al.[48] The planes in the sample lattice (described by Miller indices h,k and l) are represented by points in a 3-dimensional reciprocal lattice. For Braggs law to be satisfied and constructive interference to occur, the Ewald sphere must intersect the reciprocal lattice. The Ewald sphere is defined by the incident X-ray beam and has a radius of $\frac{1}{\lambda}$ (Figure 2.2). The distance S is consequently defined by equation 2.2.

$$S = \frac{2sin\Theta}{n\lambda} \qquad \text{Equation 2.2}$$

Substituting in Equation 2.1, for n = 1, results in S= $\frac{1}{d}$. It should also be noted that S is sometimes converted to q where S=q/2πs.

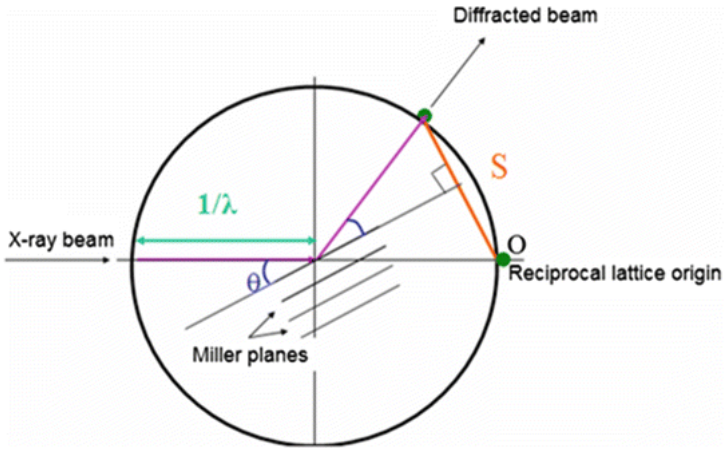


Figure 2. 2 Model of the Ewald sphere. Taken from Tyler et al.[49]

2.1.2 Small Angle X-ray Scattering (SAXS)

SAXS provides information about the long-range order and can be used to identify the phase and the lattice parameters. The ratio of the distance between SAXS rings (or SAXS peaks) can be correlated to

a specific liquid crystal mesophase depending on its symmetry (Table 2.1). The SAXS pattern also provides information of the d spacings and hence the lattice parameter. [49] [50]

Table 2. 1 Table of phases, relative peak positions and Miller indices. Taken from Tyler et al.[49]

Phase	Equation	Peak Position Ratio	Miller Indices (h,k,l)
Lamellar	$S_h = \frac{h}{a}$	1,2,3,4,5	(100), (200), (300), (400), (500)…
Micellar Cubic	$S_{hkl} = \frac{\sqrt{h^2+k^2+l^2}}{a}$	Fd3m: $\sqrt{3}$, $\sqrt{8}$, $\sqrt{11}$, $\sqrt{12}$, $\sqrt{16}$, …	(111), (220), (311), (222), (400)…
Bicontinuous Cubic	$S_{hkl} = \frac{\sqrt{h^2+k^2+l^2}}{a}$	Im3m: $\sqrt{2}$, $\sqrt{4}$, $\sqrt{6}$, $\sqrt{8}$, $\sqrt{10}$…	(110), (200), (211), (220), (310), …
		Pn3m: $\sqrt{2}$, $\sqrt{3}$, $\sqrt{4}$, $\sqrt{6}$, $\sqrt{8}$…	(110), (111), (200), (211), (220), …
		Ia3d: $\sqrt{6}$, $\sqrt{8}$, $\sqrt{14}$, $\sqrt{16}$, $\sqrt{20}$	(211), (220) (321), (400), (420), …
Hexagonal	$S_{hk} = \frac{2\sqrt{h^2+k^2+hk}}{a\sqrt{3}}$	1, $\sqrt{3}$, $\sqrt{4}$, $\sqrt{7}$, $\sqrt{9}$…	(100), (110), (200), (210), (300), …

2.1.3 Wide Angle X-ray Scattering (WAXS)

WAXS data provides information about the short-range order of the system. It is an indication of the average distance between hydrocarbon tails of neighbouring lipids. This allows for the identification of lamellar phases. The lipid molecules in the L_c phase are 'frozen' in their lattice points, resulting in sharp peaks in the WAXS. Increase in the motion of the lipid acyl chains (long-axis rotation on a 2-D hexagonal lattice) results in a slightly broader peak for the L_β phase which is centred at 4.2 Å. The L_α phase exhibits fast lateral diffusion, therefore the WAXS peak is broad and centred around 4.6 Å. The

L_o phase also exhibits rapid lateral diffusion and therefore it is difficult to distinguish it from the L_α phase.

2.1.4 Synchrotron radiation

A synchrotron is a particle accelerator in which electrons are accelerated to very close to the speed of light around a large ring. This is accomplished by high magnetic fields. The acceleration generates X-rays with varying wavelengths. The beams are much more intense and highly collimated than from standard X-ray generators, allowing the production of more intense diffraction patterns.

The radiation produced by a synchrotron has a wide range of wavelengths (0.01 to 10 nm). This is separated into different beamlines and the beam is focussed using optics. This creates a high photon flux to irradiate the sample, allowing patterns to be measured at a timescale of milliseconds.[51]

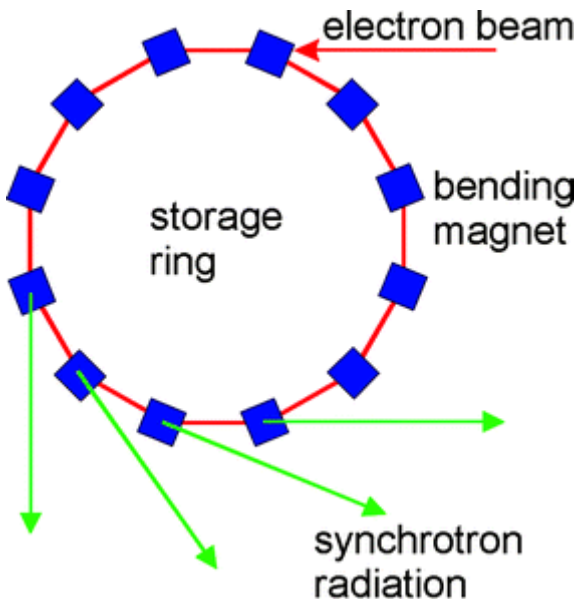


Figure 2. 3 Schematic of the generation of synchrotron radiation. Taken from Clegg et al. [52]

2.2 Nuclear Magnetic Resonance (NMR)

NMR is a powerful tool for probing structures at an atomic level to provide information on chemical environments and bonding. Each nucleon (neutrons and protons) possesses an inherent spin which is

exploited by the NMR technique. A combination of these spins gives rise to the spin quantum number, I. It should be noted that this not simply an addition of spins, rather a more detailed combination, which is outside the scope of this thesis. If I>0 then the molecule is NMR active, this includes nuclei such as ^{1}H, ^{2}H, ^{13}C, ^{15}N and ^{31}P.

NMR spectroscopy, like many other techniques, measures the energy emitted during relaxation from an excited state to a ground state. In this case it is the transition between nuclear spin levels. In the absence of an external magnetic field (B_o), atomic nuclei will randomly orient, and all these orientations are degenerate. The spin quantum number, I, can occupy quantised orientations, n, determined by:

$$n = 2I + 1 \qquad \text{Equation 2.1}$$

The presence of a magnetic field B_o removes the degeneracy as the spins will either align parallel or antiparallel to the field. This creates a difference in energy states and the energy gap between them is known as the Zeeman effect. This energy difference is small but proportional to the B_o, given by:

$$\Delta E = \gamma \hbar B_o \qquad \text{Equation 2.2}$$

Where ΔE is the energy difference between the spin energy levels, $\hbar$ is Planks constant h divided by 2π, and γ is the gyromagnetic ratio constant. The spin of a molecule creates its nuclear magnetic moment.

To transition from a lower energy to the excited energy level, electromagnetic radiation at the radio frequency range is required. This is known as the Larmor frequency and is dependent on the applied magnetic field. When NMR active nuclei are placed in a magnetic field, the spins aligning parallel to the B_o are energetically favoured meaning the spin states (or the nuclear magnetic moment associated to the spin) is asymmetrically distributed. As a result, the net vectorial sum of the magnetic moments is along the direction of B_o and is known as the magnetisation vector.

When a magnetic dipole moment is under the influence of B_o, it experiences a torque moment which tilts its direction and induces a precession of the magnetic moment around the direction of the B_o. An additional magnetic field (B_1) is applied perpendicular to B_0 at its Larmor frequency, which causes the magnetisation vector to move from the z-axis (aligned to the B_o) to the xy-plane. It is the precession of this magnetic moment in the xy-plane which induces a current that can be measured known as the Free Induction Decay signal (FID). It is a receiver coil which detects this current. The FID is termed as decay because the current decays as the magnetisation vector returns to its equilibrium state. The FID is then Fourier Transformed to the NMR spectrum. [53] [54]

2.2.1 Solid-state NMR spectroscopy

This body of work uses solid state NMR (ss-NMR) to analyse lipid systems. Provided here is a brief overview of the technique, for a more detailed overview please refer to Seelig et al. [55]

2.2.2 Molecular interactions

In quantum mechanics, the wavefunction (ψ) is a mathematical description of the state of the system; if the wavefunction is known then all the properties of the system can be deduced. An important property of a system is the nuclear spin or collection of spins, which are described by the ψ when immersed in a specific environment. An operator is also associated to a ψ and describes the observable physical information for the system. The total energy of a system is described as the Hamiltonian operator ($\hat{H}$) and defined as:

$$\hat{H} = \hat{V} + \hat{K} \qquad \text{Equation 2.3}$$

Where $\hat{V}$ is the potential energy operator and $\hat{K}$ is the kinetic energy operator.

The samples used for ss-NMR are generally comprised of powders consisting of many crystallites with random orientations. Due to the fixed position of these crystallites (lack of tumbling), the orientation of molecular interactions results in widening of the signal linewidth. This results in a spectrum called

the powder pattern. The molecular interactions within the system are chemical shielding, dipole-dipole interactions and quadrupolar coupling.

The broadening of the powder pattern in ss-NMR can be explained by the interactions which impact spin and are dependent on the crystallite orientation with respect to the magnetic field. The expression for the total $\hat{H}$ in a spin system is:

$$\hat{H} = \hat{H}_{ext} + \hat{H}_{int} \qquad \text{Equation 2.4}$$

Where $\hat{H}_{ext}$ is representative of the external B_o and $\hat{H}_{int}$ is representative of the internal molecular interactions which are summed as:

$$\hat{H}_{int} = \hat{H}^{CS} + \hat{H}^{Q} + \hat{H}^{II} + \hat{H}^{IS} + \hat{H}^{SS} \qquad \text{Equation 2.5}$$

Where CS is the shielding contribution, Q is the quadrupole coupling interaction and II, IS and SS are the spin interaction between two species of spin (I and S). In an NMR experiment the spin not only interacts with the B_o but also the smaller local magnetic field produced by other nuclear magnetic dipoles (B_{loc}). The magnitude of the impact of B_{loc} to the spin of a system is dependent on the chemical shielding. In solution NMR, the impact arising from B_{loc} to the spin is averaged to zero due to rapid tumbling of the molecule. As rapid tumbling does not occur in ss-NMR, a set of similar spins can experience the B_{loc} differently, if not perfectly aligned (as single crystals are). In a perfectly aligned sample, or a perfectly homogenous sample the contribution of line broadening from $\hat{H}_{int}$ is small. However, this project analyses lipids in water which have a gel-like consistency meaning there is low internal order. This results in broader signals in comparison to solution NMR spectra therefore the resulting spectrum is a powder pattern. [56] [57]

2.2.3 Shielding Interaction

The secondary magnetic field (B_{loc}) is produced by the current from electrons when immersed in a magnetic field (B_o). B_{loc} has an impact on the nucleus' resonant frequency, and the interaction of the electrons to the nucleus is called the shielding interaction (σ). The shielding interaction has an

orientation dependence as at certain orientations the neighbouring nucleus is unable to interact with the B_{loc} created by electrons (Figure 2.4). In solution NMR, the resonant frequency is quoted as the chemical shift (as it is measured as the shift from the reference) as a scalar number. As in ss-NMR there is an orientation dependence with respect to B_o, the frequency is quoted as a chemical shift tensor (σ).

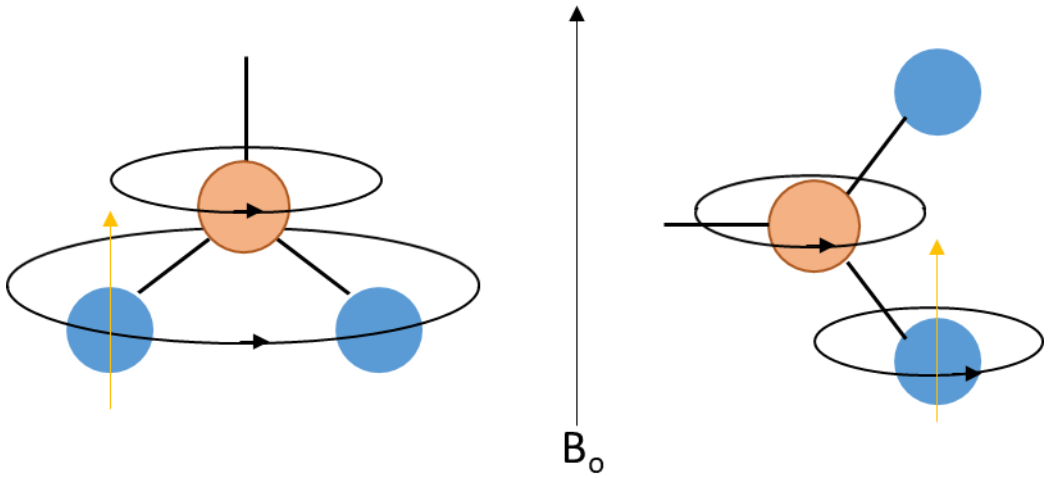


Figure 2. 4 Illustration of the shielding interaction and its orientation dependence. The magnitude and direction of the shielding field experienced by a nuclear spin (yellow arrow) is dependent on the orientation of the electron density with respect to B_o. [58]

It should be noted that each molecular group could be randomly oriented in many possible orientations with respect to B_o. Each orientation has its own spectral frequency so gives rise to its own line. It is the overlap of all these spectral lines which give rise to a powder pattern. Depending on the symmetry of the chemical shift tensor, the powder pattern assumes typically-shaped profiles which can be related to the particular lipid phase present. [59] [60] [61]

2.2.4 ^{31}P Solid State NMR

Phospholipids contain a phosphate group at the hydrophilic lipid headgroup which provides a selective tool for ^{31}P ss-NMR experiments. The resulting powder pattern provides information on the structure of the phase and the motion and orientation of the lipid headgroups. Aligned crystal samples would give a distinct chemical shift for each magnetically inequivalent crystal site, however a non-oriented sample produces a powder pattern due to the many different orientations.

The motional properties of a phosphate group within a lipid molecule are somewhat limited. The rotation of the phosphate group along the long axis results in the chemical shift tensor (σ_p) to be averaged resulting in an effective tensor which is axially symmetric around the director axis. These are represented as σ_{II} and $\sigma_{\perp}$, which are chemical shift tensors parallel and perpendicular to the axis. A stack of perfectly aligned bilayers comprised of phospholipids would show a single peak in the ^{31}P ss-NMR powder pattern as the phosphate groups would be axially symmetric around the bilayer normal. However, for unaligned bilayers, or for vesicles (micelles) the edges of the powder pattern are represented by σ_{II} (low intensity) and $\sigma_{\perp}$ (high intensity). [62]

2.2.5 ^{2}H Solid State NMR

Deuterium is a quadrupolar nucleus and therefore the nuclear spin is dominated by the quadrupolar interaction (as it has a spin of greater than ½). They occur because the electric quadrupole moment of the nucleus interacts with the electric field gradients (efg) generated by the electrons. This results in a distortion of the nucleus and line broadening of signal. The natural abundance of deuterium is very small therefore it is introduced into the target phospholipid through organic chemistry allowing for selective examination of different areas of the molecule.[63]

In this body of work the perdeuterated lipid DPPC-d_{62} has been used which allows us to record the spectrum of the entire lipid chain. The differences in motion of the chains in L_{α} and L_{β} phases produces characteristic powder patterns. The L_{β} phase shows a featureless peak and a lack of fine structure which is indicative of rigid chains on the NMR spectral timescale. The L_{α} phase however does have a powder pattern with more detailed fine structure, as the rate of molecular long axis rotation exceeds the NMR spectral timescale.

Quadrupolar splitting can be expressed as the order parameter, which is directly extracted when the C-^{2}H bond is aligned parallel to the magnetic field. This however is difficult to observe in a pake powder pattern due to the large overlap of the C-^{2}H bonds in a spectrum of perdeuterated phospholipid. In oriented or stacked bilayers, the overlap of the signal would be eradicated as all C-

^{2}H would be oriented at the same angle, however the sample preparation is difficult to achieve. This has led researchers to develop a 'depaking' method by which the unoriented axially symmetric static spectrum is converted into a 0° oriented spectrum whereby the quadrupolar splitting can be assigned to a chain position. [64]

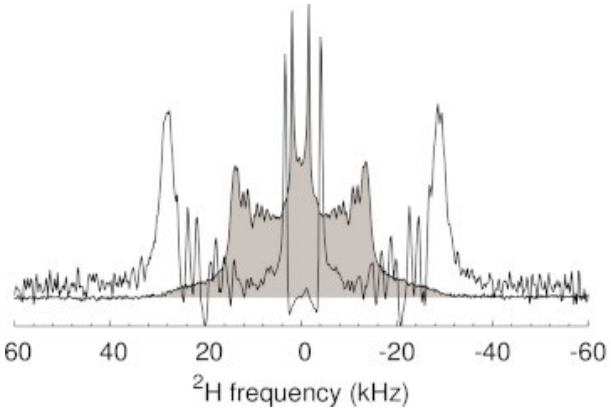


Figure 2. 5 Paked (grey) vs. depaked spectra of d-DMPC. Taken from Sani et al.[64]

2.3 Differential Scanning Calorimetry

Differential scanning calorimetry (DSC) is a thermoanalytical technique which can monitor the changes in phase transitions. A sample pan and an empty pan are heated at the same rate, and the difference in input energy required to match the temperature of the sample, to that of the reference is recorded. As a result, an endothermic process produces a peak, whereas an exothermic process produces a trough. The peak position provides the melting or crystallisation temperatures, and the area of the peak provides information about the enthalpy and entropy of transition. [65]

Chapter 3: Methods and Materials

3.1 Materials

1,2-dipalmitoyl-sn-glycero-3-phosphocholine (DPPC) and 1,2-dioleoyl-sn-glycero-3-phosphocholine (DOPC) were purchased from Avanti Polar Lipids (Alabaster, AL, U.S.A.) as solutions in chloroform (25 mg/ml) and stored at -20.0 °C and used as received. d_{62}-DPPC was purchased as a lyophilised powder from Avanti Polar Lipids. α-Tocopherol (98% purity), glyceryl triolein (triolein) and cholesterol were purchased from Sigma Aldrich (Gillingham, UK or Merk, Germany), and used as received.

3.2 Sample preparation

3.2.1 Lipid films

Lipid films were prepared by dissolving all constituents in $CHCl_3$, stirring together and then evaporating the $CHCl_3$ with a N_2 stream. The compositions were then put under vacuum for a minimum of 24 hours before use. For NMR and X-Ray Diffraction analysis, the anhydrous sample mixtures were then hydrated with 60-70 % wt distilled water and heat cycled a minimum of five times (from 5-25 °C).

3.2.2 Preparation of Giant Unilamellar Vesicles (GUVs) by electroformation

The lipid mixtures were put in $CHCl_3$ to obtain a concentration of 2 mg/ml. To this, 0.2 mol% Rh-DHPE dye was added. ITO coated microscope slides (Sigma Aldrich, Gillingham, UK) were cleaned by a mild detergent and sonicated. The slides were then heated to 60 °C and 30 µl of solution was spread evenly on the conducting side of the slide. The slide was then placed under vacuum to evaporate off any residual solvent for 30 mins. A PDMS spacer with a central cut out was then placed on the lipid film and the resulting chamber was filled with 199 mM sucrose solution. Another ITO coated slide was placed on top, ensuring that both conductive sides were facing each other, and secured using crocodile clips. The chamber was then incubated at 60 °C and an alternating electric field of 1 V, 10 Hz was

applied using a function generator (Aim-TTi, TG315) for two hours. The field was then changed to 1 V, 2 Hz for 1 hour. From the resulting solution, 10 µl was extracted and dissolved in 90 µl of 200 mM glucose solution. This was then imaged on a BSA lined glass slide, using a fluorescent microscope within 48 hours.

3.2.3 Preparation of Droplet Embedded Vesicles (DEVs)

DEVs were prepared from GUV's by contacting them with an oil emulsion. 70 µl of HKM buffer (HEPES buffer with 1 mM $MgCl_2$ and 120 mM CH_3CO_2K) was added to 5 µl of triolein to form the oil emulsion. The HKM buffer (at pH 7.4) was vortexed with the triolein until a milky solution formed (approximately 10 s). 50 µl of this emulsion was then mixed with 50 µl of GUV solution and gently mixed on a rotating tube mixer for 5 min. The formation of DEVs was detected using a fluorescent microscope. For full details of the protocol, refer to Thiam et al.[66]

3.3 DSC Experiments

Anhydrous samples were weighed (8-12 mg) into stainless steel pans (TA Instruments, Elstree, U.K) and 60-70 %wt water was added before the pans were sealed. Three temperature cycles were taken from 25-75 °C, at a rate of 5 °C/minute (heating and cooling), of which the third cycle was used for analysis. This was done using a PerkinElmer Diamond DSC and the data was exported and analysed on Origin Pro software.

3.4 Solid state-NMR Experiments

All spectra were obtained on a Bruker 600 MHX NMR spectrometer (Avance III HD) operating at 14.09 T. The ^{2}H resonance was 92.1 MHz and ^{31}P was 242.9 MHz with a recycle delay of 0.5 s for all data acquisitions. For all spectra a minimum of 10,000 scans were taken. All hydrated samples were placed in 2.5 mm zirconium rotors. All powder patterns were analysed in Bruker Topspin software before being exported to Origin Pro.

^{2}H spectra were symmetrised on the Topspin software. They were also dePaked to remove the angular dependence of the quadrupolar splitting from each CD_2 group. This was done using the NMRPipe macro by Dr. Marc Antoine Sani (University of Melbourne). [64]

3.5 X- Ray Diffraction

SAXS and WAXS data were obtained at the Diamond Light Source, beamline I22 (Didcot). Samples were placed in glass capillaries and loaded into a temperature-controlled cell. Images were initially taken at 25 °C. For samples which were temperature scanned, the capillaries were initially heated up to 60°C and an x-ray pattern was taken. The capillaries were then gradually cooled back down to 25 °C and an x-ray pattern was taken at 10°C intervals. The X- ray beam had a wavelength of 0.69 Å (energy of 18 KeV). Typical acquisitions times were 1 s per 2D scattering frame. Silver behenate was used to calibrate the instrument. A Pilatus 2M detector was used to capture SAXs and WAXs patterns simultaneously, and the detector distance varied between 1-5 m. Images were processed using DAWN software and exported to Origin Pro 2016 for analysis. The WAXS data were fitted to a Gaussian function, and the peak centres and peak areas extracted.

3.6 Fluorescence Microscopy

GUVs were transferred to 1.5 mm deep polydimethylsiloxane wells on glass slides and sealed with coverslips. They were imaged on a Nikon Eclipse TE2000-E inverted microscope. A long working distance objective lens was used to image the sample in phase contrast and fluorescence mode. The lamp was turned off immediately after image acquisition to minimise photobleaching. The images were acquired on an Andor Zyla sCMOS or Ximea based camera and recorded using custom built software. The images were then processed using ImageJ. Contact angles were calculated using Matlab.

3.7 Polarising Microscopy

Polarised light microscopy provides information on absorption and colour between matters with differing refractive indices. It can distinguish between isotropic and anisotropic substances and reveal information regarding the structure of anisotropic materials. This is accomplished by exploiting the interference of split light rays after passing through the sample, and re-uniting along the optical path.

Samples in solvent ($CHCl_3$ or C_2H_5OH) were placed onto glass slides and imaged after the solvent evaporated and water was added. These samples were also heat cycled on a thermal stage. Images were taken with a Nikon Eclipse E600 polarising microscope, with a Nikon CFI Achromat 4X, 10X and 20X objective lens connected to a QICAM fast-1394 CCD camera (QImaging, Canada). Images were captured using a custom-made LabVIEW program and analysed using ImageJ.

3.8 Fluctuation Analysis

Fluctuation analysis measures the bending rigidity of vesicles that undergo thermal fluctuations. These undulating vesicles behave in a wave-like manner and therefore can be modelled to extract their intrinsic properties. Flaccid vesicles were imaged under phase contrast microscopy on a Nikon Eclipse TE-2000-E inverted microscope with a high speed Ximea camera (exposure of 1ms) and recorded using custom built software. The vesicles were then analysed by an image analysis programme using the LabView software package (National Instruments, Austin, Texas). The vesicle edges were detected and converted to polar coordinates relative to the vesicle centre for Fourier transform and further analysis. The vesicle edges from the phase contrast images were detected as maximum intensity points. The bending rigidity was then extracted using in-house software which has been developed using the method reported by Yoon et al.[67]

Chapter 4: DPPC interactions with α-Tocopherol

4.1 Introduction

The cell membrane is largely comprised of phospholipids, of which two commonly studied examples are DPPC and DOPC. This chapter explores the impact of the addition of α-Toc to the saturated DPPC (Figure 4.1). As DPPC is a saturated lipid, the concept of 'membrane fluidity' is explored in this work. Generally, the term 'fluidity' refers to the micro-viscosity of the acyl chains in a phospholipid bilayer, therefore DPPC forms an L_β gel phase at low temperatures and a fluid L_α phase at higher temperatures (T_m at 42 °C). However, it is also important to remember that motions such as rotational, translational and flip-flop also exist which govern the fluidity of a bilayer. [30]

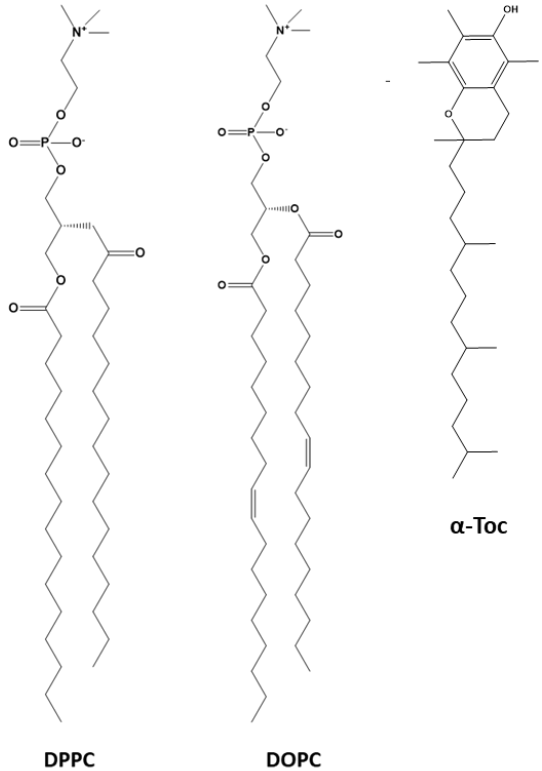


Figure 4. 1 Chemical structure of lipids: DPPC and DOPC and α-Toc

A property of α-Toc which has been commonly quoted in the literature is its ability to stabilise membranes. This refers to a reduction in fluidity rather than its antioxidant action. Diplock et al. [40]

were the first to report that α-Toc may be functioning effectively as an antioxidant by stabilising membranes, so the bilayer is less 'leaky' therefore less susceptible to oxidation reactions. Wassall et al. also reported the stabilisation impact of α-Toc on saturated bilayers using ^{2}H NMR. Above the transition temperature, the addition of 17-20 mol% α-Toc imparted an ordering effect on the fluid phase of d_{31}-DPPC. This same impact is explored in this chapter with mixed dispersions of DPPC, DOPC and α-Toc. [68]

It was reported that below the transition temperature, the addition of α-Toc induces a rippled gel phase with dilauroyl-, dimyristoyl-, dipalmitoyl-, and distearoyl-phosphatidylcholines.[69] X-ray diffraction showed that at temperatures below 30 °C, the $P_{\beta'}$ phase was dominant. Freeze fracture electron microscopy studies showed that the periodicity of the $P_{\beta'}$ phase decreased with increasing concentration of α-Toc. It was concluded that at concentrations of less than 10 mol% αToc, enriched domains were formed of a ripple phase coexisting with a planar gel phase. Kamal et al. have specified this rippled gel is a modulated phase which is like that of a ripple phase, however characterised by a rectangular unit cell as opposed to an oblique one and consists of bilayers with a periodic height modulation (Figure 4.2). [70]

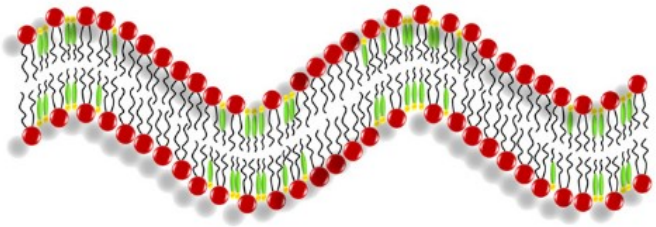


Figure 4. 2 Model proposed by Kamal et al. of the modulated phase where the α-Toc composition is coupled to the bilayer curvature. Taken from Kamal et al.[71]

This modulated phase has previously been proposed by Karmakar et al. [72] with the addition of cholesterol to a DPPC bilayer. The rippled phase has two different bilayer thicknesses because of the two arms of the ripple, which is partly accounted for by a tilt along the ripple wave vector. On the other hand, both arms of the modulated phase have a comparable bilayer thickness. This suggests

that the tilt in the rippled phase is decreased in the modulated gel phase, giving rise to a rectangular lattice structure. [73]

This work compares the impact of α-Toc to that of cholesterol with DPPC bilayers. It is known that cholesterol imparts an ordering effect on DPPC and other saturated lipids. This is because cholesterol's fused ring structure restricts the reorientation in the upper part of the phospholipid chains, which then propagates to the lower. Theoretically α-Toc's chromane ring could also be imparting such rigidity, however this depends on various factors such as location in the bilayer and concentration. [74] [36] [75]

Alongside α-Toc interactions with DPPC, mixed dispersions of DPPC, DOPC and α-Toc are also analysed. The original fluid mosaic model assumed a homogenous distribution of phospholipids, however the existence of domains within cell membranes is now more widely accepted. Microscopic domains occur due to headgroup charges, or acyl chain lengths. It is known that cholesterol partitions into more saturated domains and therefore imparts lateral segregation. This work compares the phase behaviour of α-Toc to that of cholesterol. It is known that cholesterol induces the formation of the liquid ordered phase. This phase occurs upon the mixing of cholesterol and a saturated phospholipid, cholesterol closely packs with the acyl lipid chains and limits the trans-gauche isomerisation. Due to this constraint, the acyl chains become more ordered therefore restricting translational movement, however lateral and rotational diffusion still occurs. Although cholesterol exhibits this ordering effect on both saturated and unsaturated phospholipids, due to the cis-double bond on unsaturated acyl chains, cholesterol is able to order saturated lipids to a greater extent. This leads to phase separation of the liquid ordered (L_o) and fluid lamellar (L_α) or liquid disordered (L_d) phase, in mixtures of cholesterol, saturated and unsaturated lipids. [76] [77]

Phase separated domains in giant unilamellar vesicles by the addition of cholesterol to mixtures of DPPC and DOPC have been widely reported. The formation of microdomains in GUVs is visualized

under fluorescence microscopy, using a fluorescently tagged lipid with an affinity to one phase. The observation of bright and dark regions, or microdomains has given rise to the lipid raft theory. These are localised regions within cell membranes, in which certain proteins and lipids are concentrated. These rafts are associated with important biological processes such as cell signalling, endo- and exocytosis, and protein transport. [78]

This chapter describes the effects of replacing cholesterol by α-Toc in GUV's and assesses the impact of the addition of α-Toc to DPPC bilayers by DSC, ^{31}P NMR and X-ray diffraction techniques.

4.2 Results

4.2.1 DSC of fully hydrated mixtures of DPPC and α-Toc

DSC can be used to identify the thermotropic behaviour of lipid systems. In this case it was used to identify the thermally induced phase transitions of DPPC in excess water, and how they are altered by the addition of α-Toc.

The DSC thermograms of DPPC with α-Toc clearly depict that α-Toc interacts with DPPC and has an impact on its phase behaviour. The DSC thermogram of pure DPPC (in excess water) shows a pre-transition at 36.3 °C and a main transition peak at 42.7 °C (Figure 4.3). This pre-transition is indicative of a gel-to-gel phase transition, and in the case of DPPC is already established to be a $L_{\beta'}$ (tilted flat) to $P_{\beta'}$(rippled) gel state phase transition. [79]

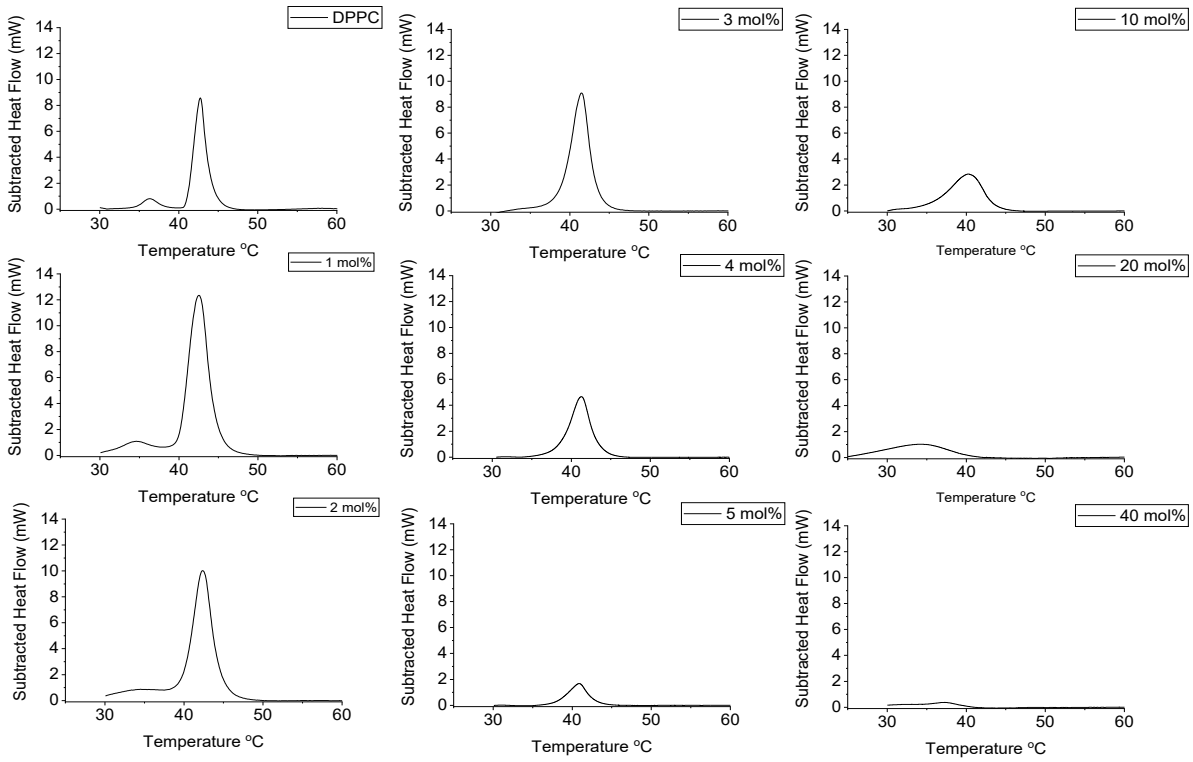


Figure 4. 3 The smoothed DSC thermograms of DPPC and DPPC with α-Toc mixtures in excess water. The molar percentage of α-Toc is given in the figures. The sequential addition of α-Toc eradicates the pre-transition and broadens and flattens the main transition until it is entirely suppressed. Graph adapted from MRes dissertation.[80]

The addition of 1-3 mol% α-Toc wipes out this pre-transition suggesting that even small amounts of α-Toc sufficiently disrupt the gel phase packing of DPPC. It can be concluded that α-Toc induces the $P_{\beta'}$ (rippled) gel phase in DPPC at temperatures below the pre-transition temperature, however further studies have shown a different gel phase. Kamal et al.[71] have reported that this is a modulated phase as electron density profiles have shown the DPPC bilayers have a periodic height modulation (Figure 4.2). This demonstrated α-Toc's ability to not only disrupt gel phase bilayers but also induce a long range order. [70 6]

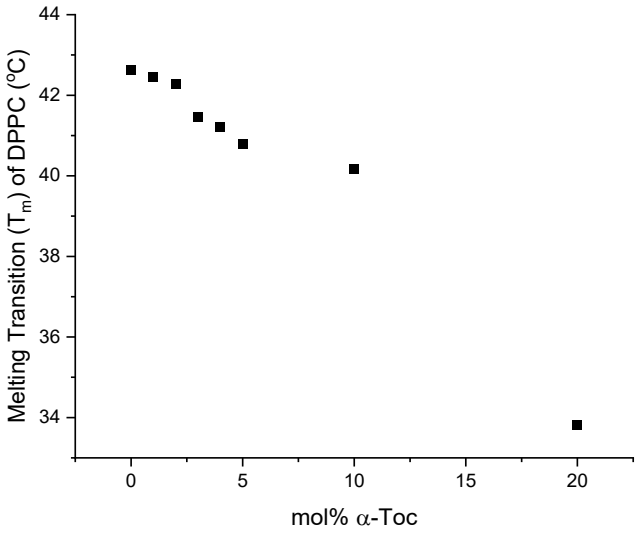


Figure 4. 4 The melting transition temperature (T_m) of DPPC at various compositions of α-Toc

The main peak transition of DPPC is indicative of a gel to fluid phase transition. The transition temperature shifts from 42.7 °C to 42.5 °C, 42.3 °C and 41.4 °C with the addition of 1,2 and 3 mol% α-Toc respectively (Figure 4.4). Although the transition temperature is not altering significantly at low concentrations of α-Toc, there is an increase in peak width (Figure 4.3). The full width half maximum (FWHM) increases from 1.62 °C for pure DPPC to 2.52 °C for 3 mol% α-Toc with DPPC. This could signify co-existence of gel-like with fluid-like phases. Neunert et al.[81] report the broad peak could be indicative of multiple overlapping peaks, which arise from phase separation and separate phase transitions within the membrane. The increase in FWHM could be attributed to the main DPPC transition and membrane complex/complexes formed between α-Toc and DPPC.

The addition of 4-10 mol% α-Toc results in more significant alterations to the main peak height and widths. The transition temperature continues to decrease, and the height of the peak also becomes flatter. At 10 mol% α-Toc, the peak height also significantly decreases. The height of the peak is almost 4-fold lower than that of pure DPPC (Figure 4.3) showing that the transition enthalpy is decreasing dramatically. The peak continues to broaden and flatten with the addition of 20 and 40 mol% α-Toc to a point where it is no longer discernible. The T_m also continues to decrease at higher α-Toc compositions.

The peak area of the DSC thermograms can be used to determine the molar entropy change. A decrease in transition entropy with increasing amounts of α-Toc is apparent (Figure 4.5). The change in entropy for each composition is an indication of the entropy (and enthalpy) difference between the L_β phase and the L_α phase. The molar entropy progressively decreases with the addition of α-Toc from 93 $JK^{-1}mol^{-1}$ to 0.4 $JK^{-1}mol^{-1}$ (Figure 4.5).

The decrease in entropy could be attributed to one of three processes: i) the gel phase is becoming more fluid with the addition of α-Toc, ii) the fluid phase is becoming more gel-like i.e., more ordered, iii) both processes are occurring together. In any case, the DSC thermograms confirm that the entropy (and enthalpy) gap between the gel and fluid phase of DPPC is reduced with the addition of α-Toc.

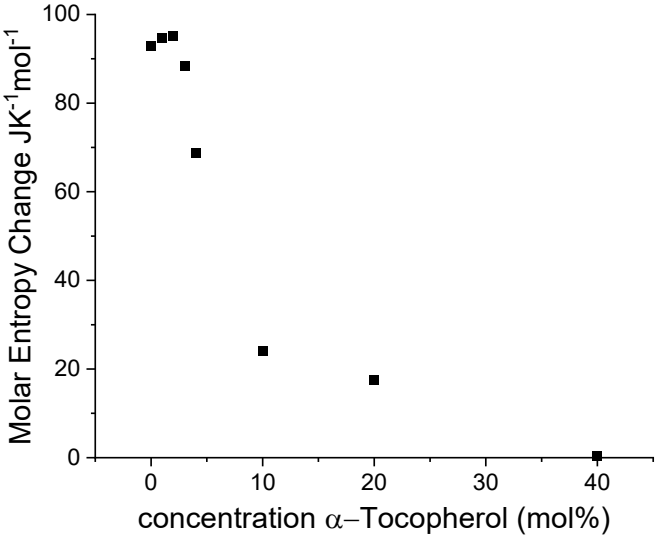


Figure 4. 5 The change in molar entropy with the addition of α-Toc to DPPC, calculated from DSC thermograms. The change in entropy dramatically decreases with the addition of α-Toc.

DSC thermograms show a similar trend with the addition of cholesterol to DPPC. The total enthalpy decreases linearly with increasing cholesterol composition, and the transition peak broadens and flattens out. Cholesterol can perturb the phospholipid chain packing and weaken the intermolecular forces produced by the all-trans conformation of the acyl chains. Increasing the concentration of the molecule causes enough disruption within the acyl chain packing to eventually eradicate the enthalpy of transition. Therefore, this data suggests that α-Toc is behaving in the same manner. [82] [83] [84]

4.2.2 Small Angle X-ray Diffraction of DPPC and α-Toc

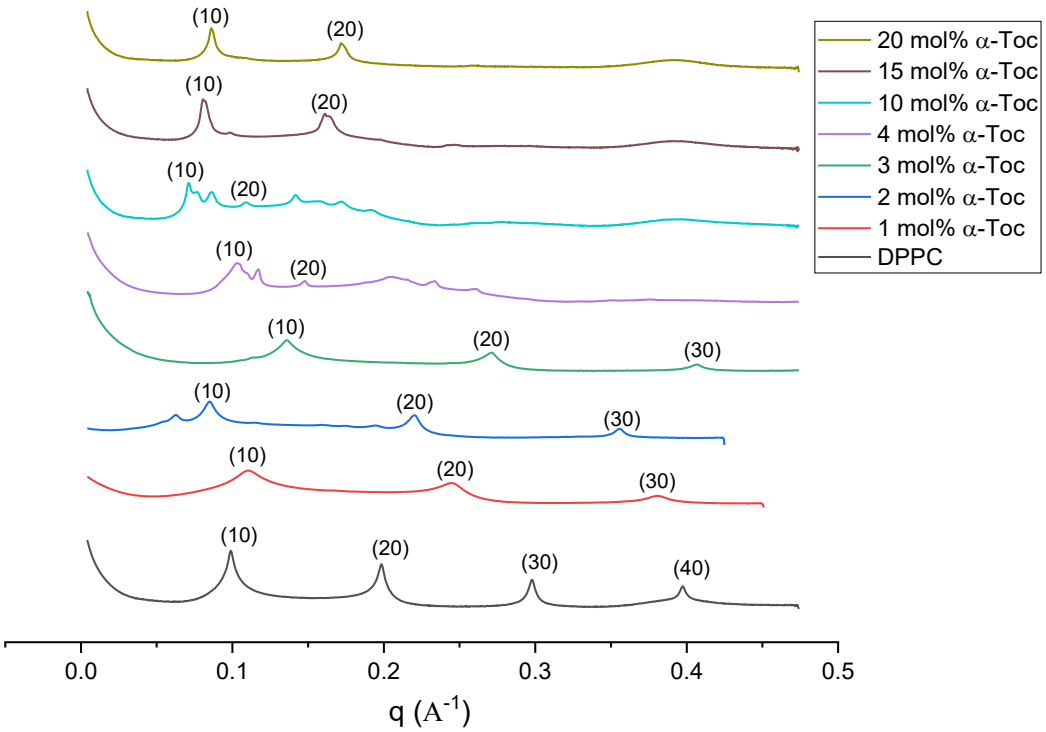


Figure 4. 6 SAXS data of various compositions of α-Toc with DPPC in excess water at 25 °C. The lamellar phase is retained at all compositions with a change in in d spacing at various compositions

The long-range order of DPPC can be probed by SAXS and indexed to determine the mesophase of the liquid crystal. DPPC alone gives rise to sharp peaks occurring at a 1:2:3:4 ratio which correspond to a lamellar phase of d spacing of 65.4 Å (Figure 4.6). SAXS does not differentiate between fluid, gel, crystalline or ordered phases. The addition of α-Toc results does not result in a phase change however, the peaks become more diffuse and the d spacing changes. The addition of 3 mol% results in a decrease in d spacing to 46.3 Å. At higher compositions of 15 and 20 mol% α-Toc, the d spacing increases to 72.9 Å. This variation in d-spacing is due to dehydration of samples resulting in a shrinking of the d-spacing. This is likely as α-Toc is highly hydrophobic.

It is important to note that the addition of 4 and 10 mol% α-Toc, although still forms peaks which correspond to a lamellar phase, also exhibit multiple other peaks. These peaks are better analysed when compared to the SAXS profile of DPPC alone at around 45 °C.

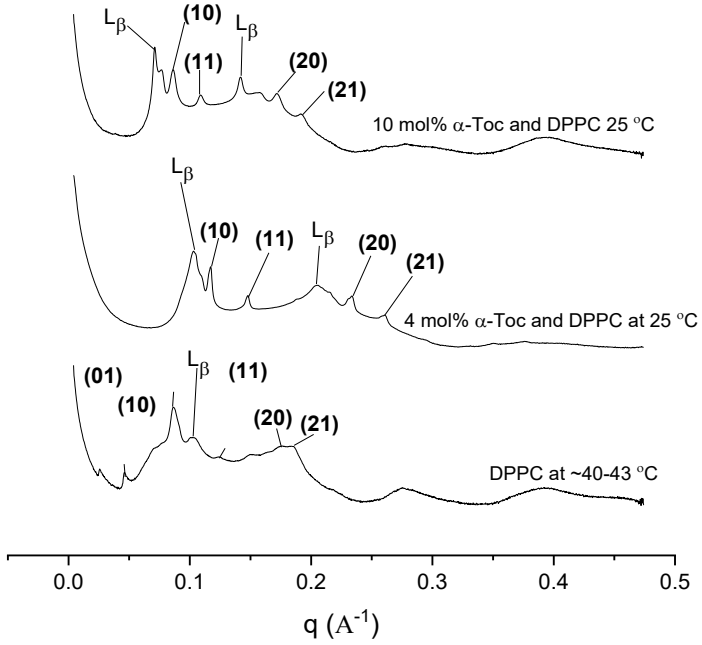


Figure 4. 7 Assignment of ripple diffraction peaks for DPPC at around 40-43 °C (near the pre-transition temperature), 4 mol% α-Toc and 10 mol% α-Toc with DPPC at 25 °C.

The pre-transition temperature (T_m) occurs at approximately 37 °C which is the transition from the tilted flat gel phase to the rippled gel phase ($P_{\beta'}$). These Bragg peaks arising from the rippled gel phase have already been well characterised by Yao et al.[85] (Table 4.1) for DPPC. The d_{obs} peaks for DPPC at 40-43 °C (Figure 4.7) agrees well with these literature values. It should be noted, that although this reading was taken when the water bath was set to 45 °C, the temperature of the sample was likely 40-43 °C therefore the appearance of the $P_{\beta'}$ phase is expected at this temperature.

Table 4. 1 The indexing of the 2D ripple phase with the d_{cal} taken from Yao et al. The d_{obs} for DPPC at 45 °C, 4 mol% and 10 mol% α-Toc fits well with calculated literature values.[85]

Peak (hk)	d_{cal} (nm) for DPPC (by Yao et al.)	d_{obs} for DPPC at 40-43 °C (nm)	d_{obs} for 4 mol% α-Toc and DPPC (nm) at 25 °C	d_{obs} for 10 mol% α-Toc and DPPC (nm) 25 °C
(01)	14.0	13.67	-	-
(10)	7.06	7.25	5.37	7.284
(11)	6.18	5.07	4.25	5.77
(20)	3.53	3.57	2.69	3.66
(21)	3.38	3.42	2.41	3.27

The Bragg peaks of the DPPC ripple phase occur at a ratio of 4: 2: 1.75 :1 :0.95. The ratio of the additional peaks occurring in the SAXS profiles for 4 and 10 mol% also align with the ratio of the rippled phase therefore can be assigned to the $P_{\beta'}$ phase diffraction pattern (Figure 4.7 and Table 4.1). Therefore, the SAXS data suggests that α-Toc promotes the formation of a $P_{\beta'}$ phase at temperatures below the pre-transition of DPPC. It should be noted that the (01) peak is missing for the α-Toc with DPPC compositions. This could be because this rippled gel structure is more like the one proposed by Kamal et al.[71] (Figure 4.2). The lack of an oblique unit cell may be the reason for the disappearance of the (01) peak in the SAXS diffraction pattern.

The $P_{\beta'}$ of DPPC alone is characterised by two repeat distances, the interlamellar distance (a) and the ripple period (b). The angle (ϒ) between these is what defines the obliquity of the lattice (Figure 4.8). Using the d_{obs} values for DPPC at 40-43 °C (Table 4.1), the lattice parameters are a= 104 Å, b=197 Å and ϒ = 136°. These lattice parameters have been calculated from equations taken from literature [86] (Supplementary Information Equations 4.1-4.6).

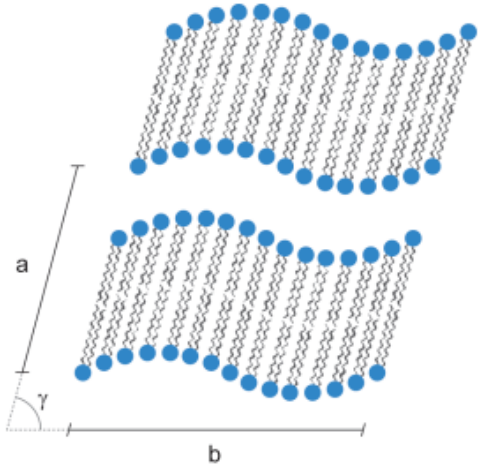


Figure 4. 8 The schematic for the ripple phase of DPPC illustrating the lattice parameters. Taken from Shaw et al.[86]

From the SAXS data it is difficult to distinguish whether compositions of 4 and 10 mol% α-Toc form the traditional $P_{\beta'}$ phase (Figure 4.8) or a structure more like the modulated phase (Figure 4.2). If it is to be assumed that the traditional oblique lattice of DPPC is still forming, then equations from literature (Supplementary Information Eq. 4.1-4.7) can be used to calculate the lattice parameters. For 10 mol% α-Toc with DPPC (using the peak assignments for Table 4.1) gives lattice parameters a=116 Å, b=62 Å and ϒ = 39°. The decrease in the ϒ angle suggests that α-Toc's inducing curvature in the gel phase bilayers of DPPC.

4.2.3 Wide Angle X-ray Diffraction of DPPC and α-Toc

Wide-angle X-ray scattering probes the short-range order of a system and therefore can be used to provide an indication of the in-plane packing of the lipid acyl chains. The size and position of the WAXS peak allows for the differentiation between the L_α and L_β phases.

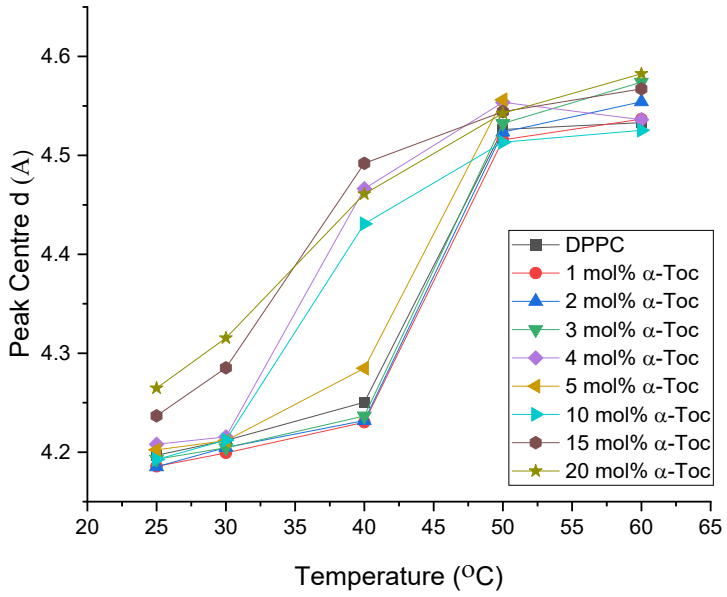


Figure 4. 9 The position of the peak centre arising from the WAXS peak, taken at various compositions of α-Toc with DPPC, and at various temperatures. The DPPC transition from the gel to fluid phase is shown to shift to lower temperatures with the addition of α-Toc. Some data points have been taken from Mres dissertation[80] although most of this WAXS data was consequently repeated. The lines in this graph are a guide to the eye.

At 25 °C, DPPC alone in excess water conditions forms an L_β phase, the corresponding WAXS peak is a sharp peak centred at around 4.2 Å (S.I Figure 4.1). Conversely, above the transition temperature of DPPC, a broad peak around 4.6 Å is indicative of the L_α phase. The fluidity or the high level of disorder and rapid trans-gauche isomerisation of the acyl chains, results in a broad diffraction peak.

The addition of α-Toc results in a change in the WAXS peak of the DPPC system. A plot of the peak position vs. temperature at various compositions of α-Toc with DPPC shows the impact of the change (Figure 4.9). At 25 °C, DPPC and compositions of up to 10 mol% α-Toc with DPPC depict a peak at 4.2 Å. The addition of 15-20 mol% α-Toc causes a deviation from 4.2 Å which highlights α-Toc's ability to disorder this gel packed system. At 60 °C, a broad WAXS peak is seen centred around 4.6 Å for all compositions of α-Toc with DPPC which is typically associated to the L_α phase. It is however difficult to distinguish between the L_α and the L_O phase. The L_O phase also exhibits fast lateral diffusion and therefore is also characterised by a broad peak between 4.2 and 4.6 Å.

The WAXS data does mirror the results from the DSC data. The addition of α-Toc shifts the gel to fluid transition temperature of DPPC to a lower value. At 40 °C (slightly below the T_m of pure DPPC which is 42 °C), higher compositions of α-Toc with DPPC exhibit a WAXS peak at around 4.5 Å which is more indicative of a fluid-like phase than a gel-like one. This once again suggests that α-Toc is reducing the enthalpy and entropy change between the L_α and L_β phase of DPPC.

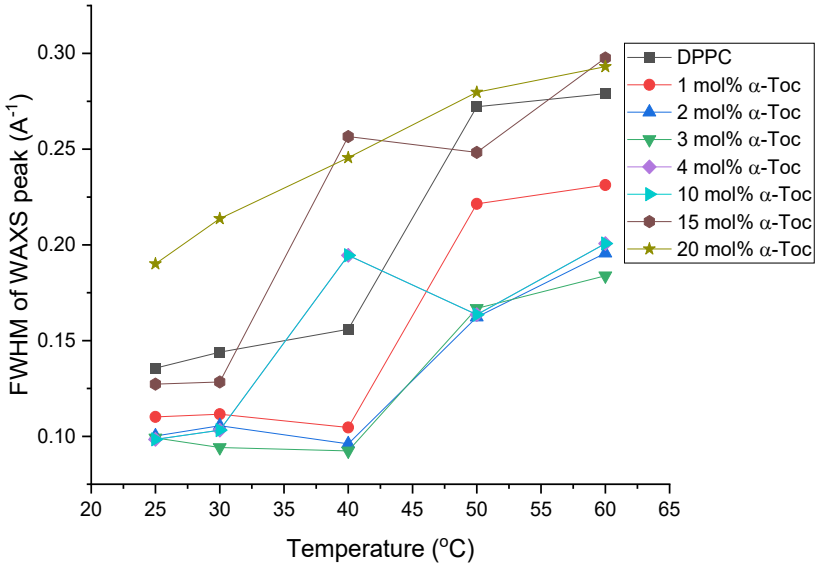


Figure 4. 10 The FWHM (full width half maximum) of the WAXS peak of various compositions of α-Toc with DPPC, and at various temperatures. The DPPC transition from the gel to fluid phase is shown to shift to lower temperatures with the addition of α-Toc. Some data points have been taken from MRes dissertation[80] although most of this WAXS data was consequently repeated. The lines are a guide to the eye.

Additional information can be derived from the shape of the WAXS peak. The width is indicative of the disorder within the system as a wider WAXS peak suggests the acyl chains are further apart therefore the X-rays diffract from a wider range of angles. At 25 °C i.e., when DPPC is in the L_β phase, the addition of 1-15 mol% α-Toc does not result in a drastic change in the FWHM of the peak (Figure 4.10). At 20 mol% the peak width increases to 0.19 $Å^{-1}$ from 0.14 $Å^{-1}$ of DPPC alone. This suggests that the system is more disordered at this composition. This disorder of 20 mol% α-Toc with DPPC is retained at all temperatures.

On the other hand, at 60 °C, when DPPC is in the L_α phase, the peak width is 0.27 $Å^{-1}$. The addition of 2-10 mol% α-Toc actually results in the width of the peak decreasing to 0.17 $Å^{-1}$. This sharp decrease

in WAXS peak width is a strong indication that the fluid system of DPPC is becoming more ordered with the addition of α-Toc. This is the same impact that cholesterol exhibits on phosphatidylcholine bilayers. [87]

4.2.4 Solid state ^{31}P NMR of α-Toc and DPPC

Phospholipid membranes spontaneously form unilamellar or multilamellar vesicles which are usually spherical in an aqueous medium. The addition of a molecule such as α-Toc may modify their shape, and the addition of a magnetic field can probe their orientation. Solid-state ^{31}P NMR is the perfect way to follow the orientation of the phospholipid molecules as DPPC molecules only have one phosphorous atom each, and α-Toc does not contain any. The resulting NMR spectrum line shape provides an indication of the average orientation and therefore phase of the DPPC molecules.[88]

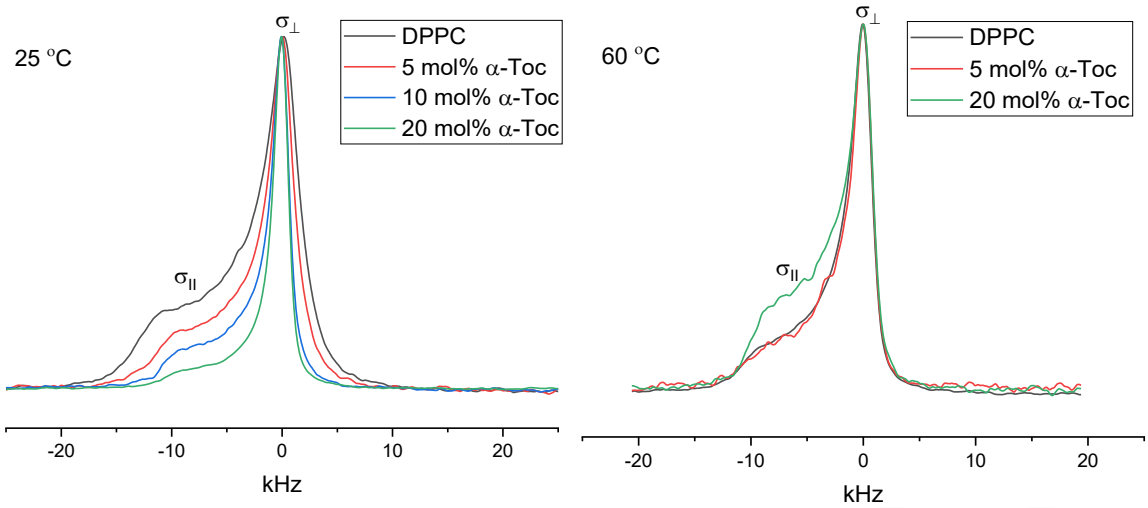


Figure 4. 11 ^{31}P NMR spectra of DPPC with various concentrations of α-Toc (on Figure) at 25 °C (left) and 60 °C (right). The addition of α-Toc to gel phase DPPC results in peak narrowing. The opposite is observed to for fluid phase DPPC, as α-Toc addition results in peak broadening

^{31}P NMR spectra were taken at 25 °C (below the transition temperature of DPPC) and 60 °C (above the transition temperature of DPPC) with compositions of 0-20 mol% α-Toc (Figure 4.11). The pure DPPC spectra at 25 °C (black line on left graph) is indicative of a standard gel phase peak. The asymmetry of this peak can be described by the populations of phospholipid molecules at a certain orientation with respect to the magnetic field. In a spherical vesicle or an ellipsoid, there are a small number of

molecules, which align parallel to the magnetic field ($\sigma_{\parallel}$) and a large population, which align perpendicular to the magnetic field ($\sigma_{\perp}$) (Figure 4.12, A). The gel phase is characterised by broad peak molecules in a vesicle occupy multiple orientations with respect to the magnetic field, and the rate of diffusion between these orientations is slow with respect to the timeframe of the NMR experiment. The resulting DPPC peak at 25 °C is broad (Figure 4.11, left) with a CSA of approximately 30 kHz. [89] [90]

At 25 °C, the addition of α-Toc progressively decreases the ΔV_Q (Figure 4.11, left). This is indicative of an increase in molecular motion within the system, resulting in an increase in anisotropy and partial averaging of the system. A decrease in linewidth suggests that the system is becoming more fluid, and the vesicle is distorting from its spherical structure so there is a larger population of molecules at oriented σ_{II}. Like the results of the DSC and X-ray diffraction studies, this further demonstrates that the addition of α-Toc causes a fluidisation effect on the gel phase membrane of DPPC. On the other hand, at 60 °C (Figure 4.11, right) the opposite trend is can be seen. When DPPC is in the fluid phase, the addition of 20 mol% α-Toc results a change in the line shape. The shoulder of the peak increases which suggests that the ellipsoidal vesicle is becoming distorted, or more compressed and the molecules are becoming more gel-like.

The ^{31}P NMR spectra mirror the conclusions drawn from DSC and X-ray diffraction studies: α-Toc causes the gel-phase of DPPC to become more fluid and the fluid-phase to become more gel like. This suggests that a L_o- type phase may be forming as the same trend is seen with the addition of cholesterol to DPPC bilayers.

It should be noted that the shape of the spectral line of the 20 mol% α-Toc with DPPC at 25 °C (Figure 4.11, left) and 20 mol% α-Toc with DPPC at 60 °C is not a standard shape for a powder pattern of a spherical vesicle i.e., an ellipsoid.

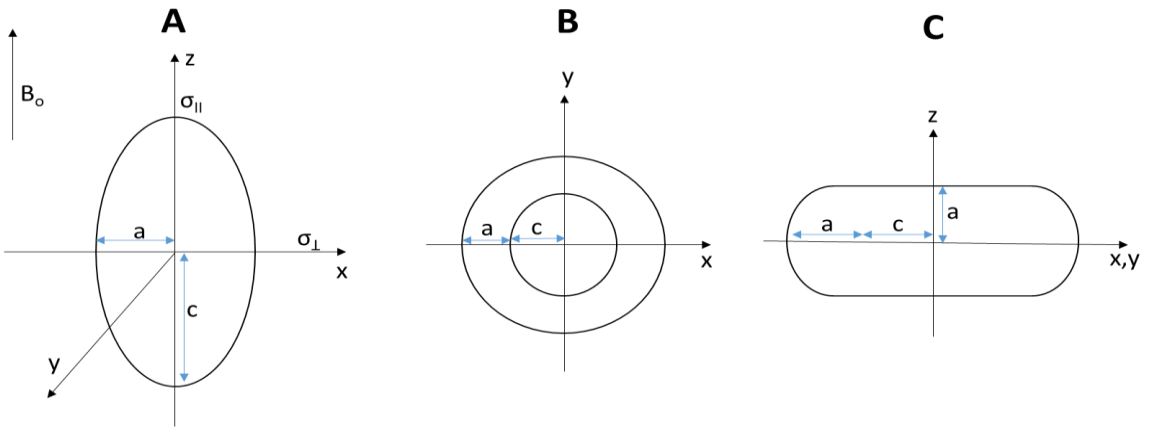


Figure 4. 12 Geometrical representations of (A) an ellipsoid, (B) a bicelle in the x-y plane and (C) a bicelle in the x-y-z plane. Adapted from Picard et al. [88]

Using order parameters Picard et al. have simulated the ^{31}P NMR spectral line shapes of structures with various r values. The r value is defined as:

$$r = \frac{a}{c} \qquad \text{Equation 4.1}$$

Where a and c are the lengths within ellipsoids and bicelles (Figure 4.12). According to reported simulated spectra, the line shape of 20 mol% α-Toc with DPPC at 25 °C (Figure 4.11, left) is indicative of an ellipsoid structure where r = 1.67. For the standard DPPC gel phase peak, r=1.00. This means the addition of 20 mol% α-Toc results in an elongation along the x-axis of the ellipsoidal vesicle (Figure 4.12, A). [88]

The line shape of 20 mol% α-Toc with DPPC at 60 °C (Figure 4.11, right) is replicated in simulated spectra of a bicelle where r= ∞. A bicelle is defined as a structure with two circular planes which is usually made of long acyl chain phospholipids, and the outer part of a torus (the rim) which is usually made of shorter acyl chain lipids (Figure 4.12, B and C). In this case it can be hypothesised that α-Toc is facilitating the formation of a bicelle- like stucture by behaving as a short chain lipid congregating on the rim of the structure.

4.2.5 Fluorescence Microscopy of Giant Unilamellar Vesicles of α-Toc, DPPC and DOPC

Much of biomolecular research involves the development and application of artificial membranes as a model for complex biological membranes. The formation of giant unilamellar vesicles (GUVs) provide one such model whereby a single bilayer is enclosed in a spherical structure, and the curvature is a close match to a cell membrane. Furthermore, the size of GUVs is ideal for visualisation under optical microscopy. [91]

These model systems have typically been used to visualise the formation of domains using fluorescence microscopy. Various compositions of an unsaturated lipid, a saturated lipid, and a derivative of a sterol (typically cholesterol) form domains within GUVs. This is due to the lateral segregation of two different liquid phases and can be visualised by staining one of the phases with a fluorescent dye. In this case the sterol has been substituted for α-Toc, and DOPC and DPPC have been used as the unsaturated and saturated lipids (at compositions depicted in Figure 4.13). Rhodamine-DHPE (Rh-DHPE) has been used to stain vesicles, it has an affinity for the more disordered liquid phase.

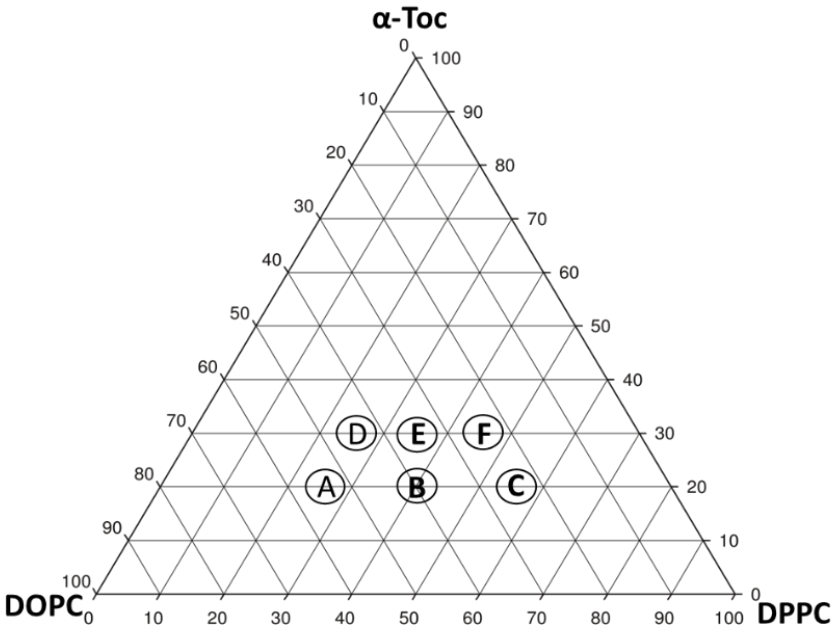


Figure 4. 13 Composition dependence of phase behaviour in GUVs of DPPC/DOPC/α-Toc is visualised using fluorescence microscopy at room temperature. Compositions of vesicles are A (4:8:3), B (2:2:1), C (8:4:3), D (7:14:9), E (1:1:1), F (14:7:9). Phase separation can be visualised for compositions B, C, E and F.

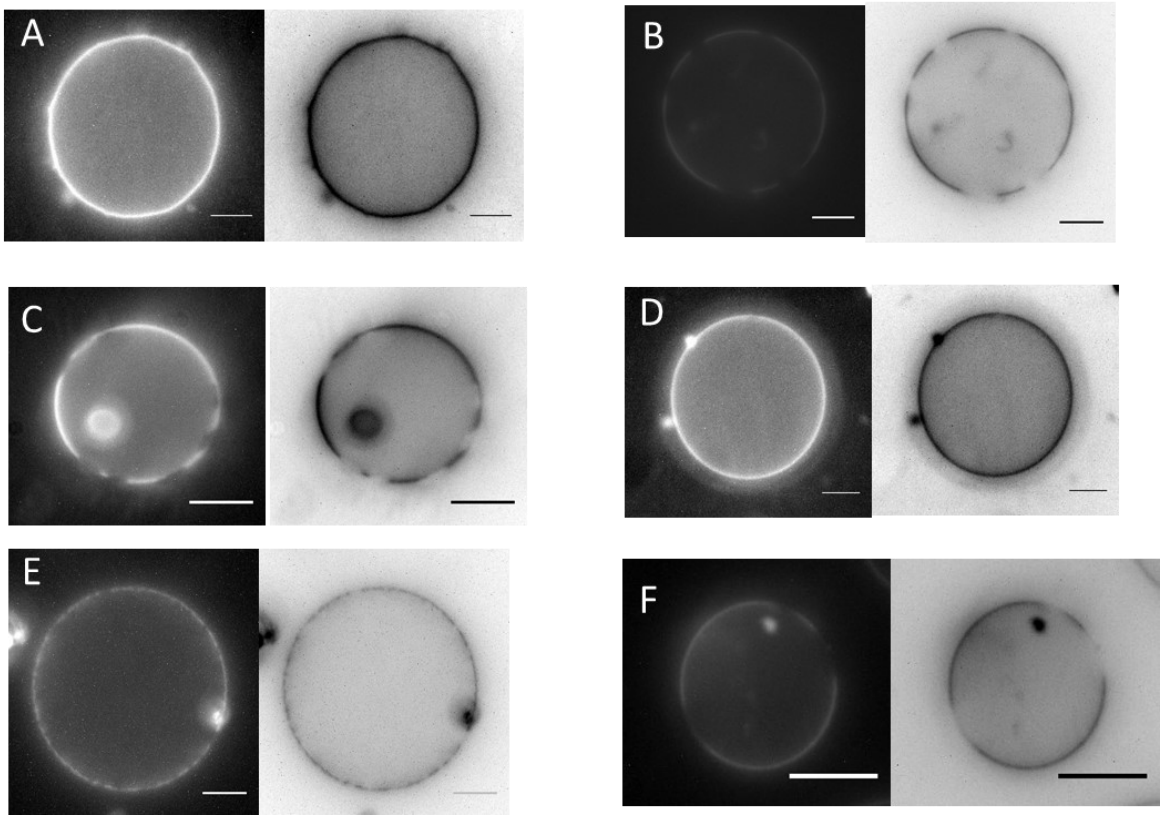


Figure 4. 14 The original images (bright GUVs with dark backgrounds) have also been inverted (dark GUVs with a light background) to easily visualise membrane phase separation. Phase separation is best visualised in static images by examining the continuity of the vesicle edges. The lack of uniformity in compositions B, C, E and F are an indication of phase separation. Scale bar= 10 µm

Fluorescence microscopy shows that vesicles of certain compositions of α-Toc, DOPC and DPPC exhibit phase separation (Figure 4.14). This is a novel and remarkable property of α-Toc as prior to this, phase separated vesicles have only been seen to be induced by a sterol or a stanol. The fact that α-Toc can also induce lateral segregation in bilayers provides a powerful indication that its function in cell membranes is not solely limited to its antioxidant function.

Typically, an equimolar composition of DPPC and DOPC yields a fluid lamellar phase, experimental results have shown that the GUV is not phase separated (S.I Figure 4.2). However Suga et al. have reported that equimolar DPPC:DOPC mixtures may form nanodomains which are not visible on a microscope.[92] The addition of α-Toc at 20 and 30 mol% induces domain formation which is visible to the eye (Figure 4.14, images B and E). The images clearly show domains forming on the vesicle edge as they are not uniformly stained by the dye. To probe this further, a video of composition (2:2:1) DPPC: DOPC: α-Toc (composition B, Figure 4.15) shows clear bright and dark domains when the GUV is out of focus. Each consecutive image is the next image from a video stack, it depicts the GUV moving out of the plane of focus in the z-stack. This serves as a z-stack of images at slices within the 3D GUV structure. From this, the bright and dark domains can clearly be seen showing evidence of phase separation.

It should be noted that with ternary mixtures of cholesterol, DPPC and DOPC, phase separated domains are very easily visualised. Bright and dark domains are clearly visible in static images. This could be because cholesterol is able to promote phase separation to a much greater extent. DiPasquale et al. [93] have reported that α-Toc does not induce domain formation up to a concentration of 10 mol%, however, as the level of phase separation is not as obvious at that of cholesterol, it is plausible that at lower α-Toc concentration it is difficult to image. The data presented here makes it difficult to conclude that at physiological conditions (10 mol%) of α-Toc, the lipid phase behaviour remains unperturbed. It is very likely that even at lower compositions (< 20 mol%, Figure 4.13), α-Toc is responsible for some phospholipid lateral re-organisation. [82] [78] [94]

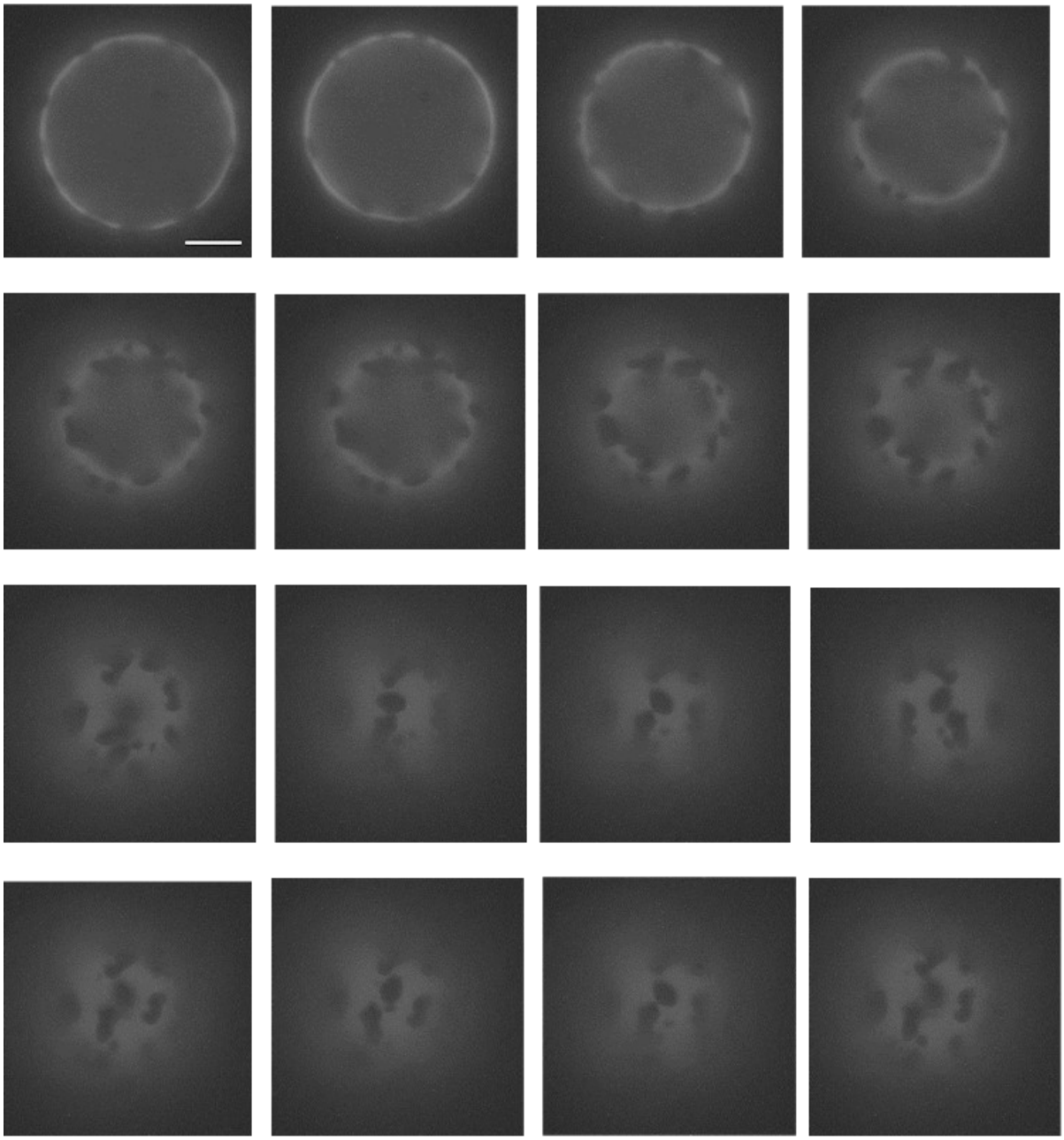


Figure 4. 15 A series of images which are a consecutive image stack for a video. It is of a phase separated GUV of composition B (Figure 2.12) which is moving in the z-axis i.e., moving out of the plane of focus. Clear bright and dark domains can be visualised

Compositions of equimolar DPPC: DOPC with 20 and 30 mol% α-Toc (Figure 4.14, B and E) show phase separation. This is also true for compositions of (2:1) DPPC: DOPC with 20 and 30 mol% α-Toc (Figure 4.14, C and F). However, compositions where the unsaturated lipid is greater than the saturated, DPPC: DOPC (1:2), the addition of α-Toc does not induce phase separation. This may be because α-Toc is unable to have an ordering impact on unsaturated lipids due to the 'kink' from the double bond promoting disorder within the system. [9]

The formation of domains is attributed to cholesterols ability to induce the L_o phase. In the present case, it is difficult to identify whether this is gel and fluid phase separation, or fluid and L_o phase separation. It can be concluded that α-Toc is inducing a phase which is unlike the fluid lamellar phase, and a combination of the DSC, WAXS and ^{31}P ss-NMR data suggests that it could likely be a L_o- type phase. From the data presented here, it is also difficult to distinguish which phase α-Toc is associating to. Cholesterol is well known to associate to the saturated lipid phase and promote the L_o phase within the DPPC-rich phase. However, α-Toc could be promoting lateral segregation by associating to the more disordered phase i.e., DOPC, which then induces ordering within the DPPC-rich phase. Previous SAXS studies suggest that α-Toc may have an affinity for unsaturated phospholipids. [82 34 78 95]

4.2.6 Solid state ^2H NMR of α-Toc, d_{62}-DPPC and DOPC

^2H solid-state NMR allows for the characterisation of bilayers containing deuterium-labelled lipids. In this case the DPPC was replaced for d_{62}-DPPC in the ternary system of α-Toc, DPPC and DOPC (Figure 4.13, composition B). For chain deuterated lipids in randomly oriented bilayers, the resulting ^2H NMR spectrum is reflective of the extent of averaging of the quadrupole interaction by the deuterated segment relative to the bilayer normal within the timescale of the ^2H NMR experiment. For a perdeuterated lipid (d_{62}-DPPC), each C-D bond along the chain is constrained to a segment orientation in a spherical vesicle, therefore it's quadrupolar splitting is reflected in the ^2H spectrum. The superposition of doublet components provides information about the bilayer organisation and phase behaviour by reflecting the constraints to segment reorientation. [96]

At 25 ^oC (below the transition temperature), the ^2H-NMR powder pattern of DPPC alone is indicative of a gel phase which lacks a fine structure from individual chain methylenes (Figure 4.16, bottom left). This is due to incomplete averaging within the NMR timescale as lipid molecules are constrained to an ordered structure with restricted movement. The addition of unsaturated DOPC, at equimolar amounts with DPPC, results in a fluid phase powder pattern with a maximum quadrupolar splitting

(ΔV_Q) ~30 kHz (Figure 4.16). This more resolved structure is indicative of rapid re-orientation of lipid molecules within a disordered phase. The addition of 20 mol% α-Toc to this system (composition B, Figure 4.13) results in an increase of the maximum quadrupolar splitting to 40 kHz. [97]

Above the transition temperature, an L_α phase is observed for DPPC-d_{62} with a ΔV_Q of 34 kHz. Equimolar mixtures of DPPC-d_{62} and DOPC, result in a ΔV_Q of approximately 25 kHz. The addition of 20 mol% α-Toc to the system results in a slight broadening of the powder pattern with a ΔV_Q of 27 kHz (Figure 4.16, right). Similar results have been reported by Wassall et al. to binary systems of only DPPC and α-Toc. The addition of 20 mol% α-Toc to d_{31}-DPPC increases the ΔV_Q from 67 kHz to 73 kHz in the gel phase. Above the transition temperature however, the ΔV_Q remained at 25 kHz even with the addition of α-Toc. [98]

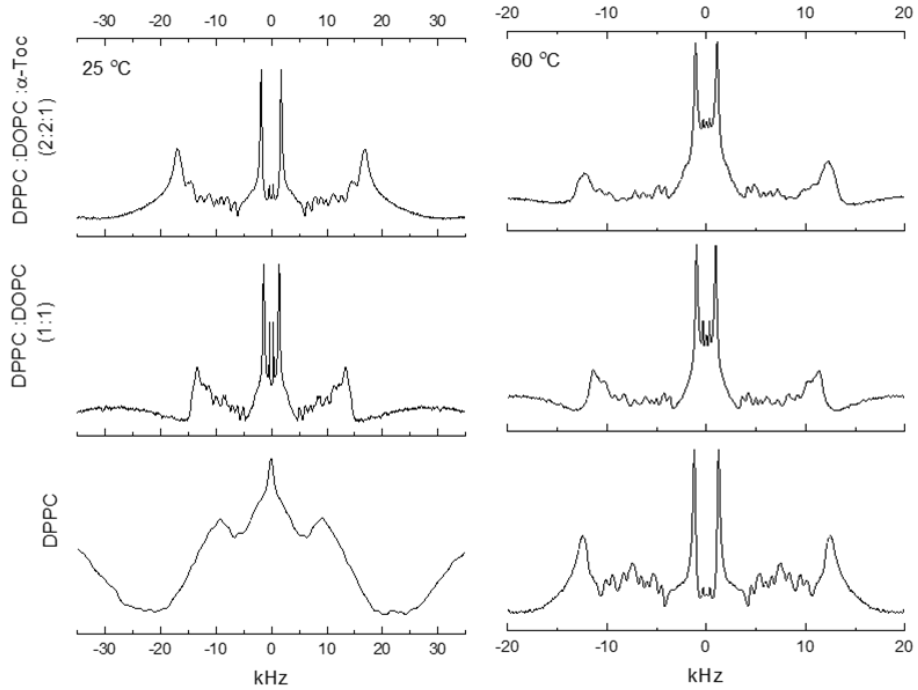


Figure 4. 16 ^{2}H-solid state NMR powder patterns of DPPC, DPPC: DOPC (1:1) and DPPC: DOPC: α-Toc (2:2:1) in excess water at 25 ^{o}C (left) and 60 ^{O}C (right). The quadrupolar splitting of DPPC-d_{62} increases with the addition of α-Toc to the system.

The increase in ΔV_Q is indicative of the system becoming more ordered. To analyse the acyl chain ordering impact of α-Toc to DPPC-d_{62}, the NMR spectra have been dePaked. This removes the anisotropy of the system resulting in greater resolution of the powder pattern. DePaked ^{2}H NMR

spectra are essentially equivalent to spectra from well-aligned stacked bilayers. The well resolved spectra allow for the calculation of the order parameter with respect to segment position of the methyl groups on the DPPC-d_{62} chain (Figure 4.17 and SI Figure 4.4-4.5). The quadrupolar splitting can then be related to the order parameter using the equation:

$$\Delta\nu_Q = \frac{3}{2}\chi_Q S_{CD}\left(\frac{3cos^2\theta-1}{2}\right) \qquad \text{Equation 4.2}$$

where $\Delta\nu_Q$ is the quadrupolar splitting, χ_Q is the quadrupolar coupling constant with a value of 170 kHz, and S_{CD} is the order parameter. In this case θ was 0° i.e. the magnetic field of the spectrometer is parallel to the bilayer normal (as set by the dePaking protocol). [99] [100]

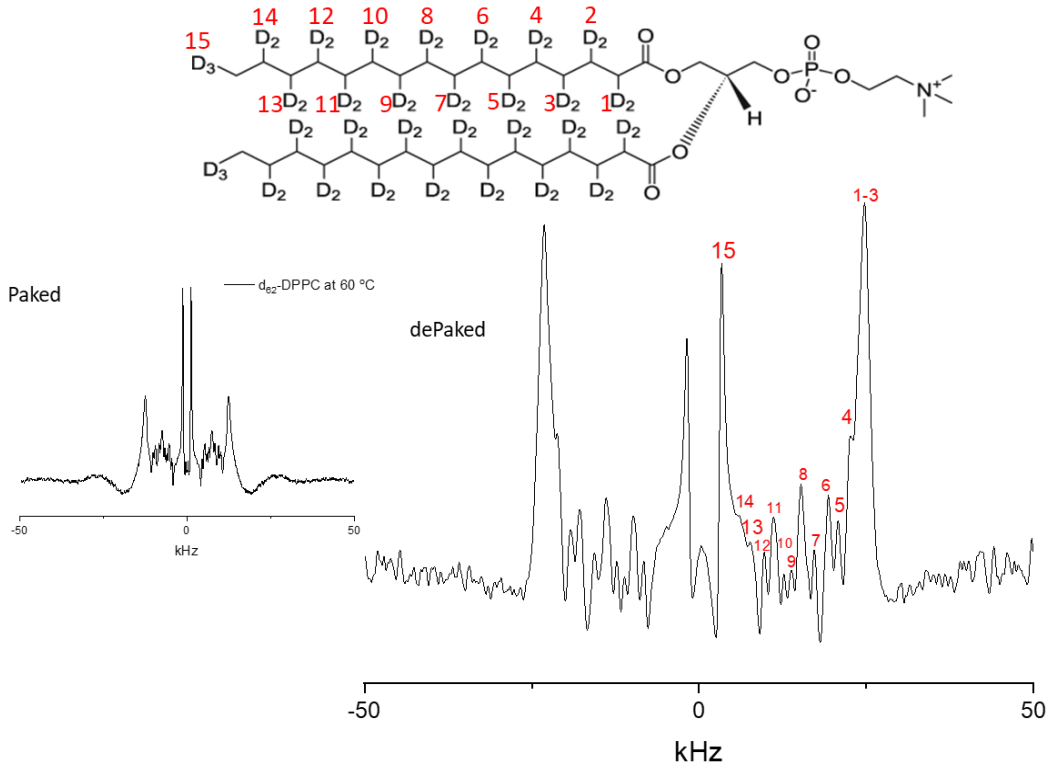


Figure 4. 17 Paked vs. DePaked ^{2}H NMR spectra of DPPC at 60°C. The dePaked NMR peaks allow for the designation of ΔV_Q with respect to the segment position.

Order profiles for DPPC-d_{62} have been calculated for binary DPPC-d_{62}: DOPC (1:1) mixtures and ternary DPPC: DOPC: α-Toc (2:2:1) mixtures at 25 °C and 60 °C (Figure 4.18). At 25 °C the equimolar DPPC: DOPC shows a 'plateau' region at S_{CD} = 0.17. This is indicative of the methylene groups closest to the

phospholipid headgroup region, as expected they exhibit the highest level of order as their rotational movement is most restricted due to their proximity to the anchored headgroups.

The addition of the α-Toc to the system increases the 'plateau' region to S_{CD} = 0.20, the increase in order parameter is an indication of an increase in constraints to the segment of C-D bonds closest to the headgroup. This shows that α-Toc is imparting an ordering effect to this segment position and therefore further restricting rotational movement with respect to the NMR spectral timescale. This is mirrored at 60 °C as the addition of α-Toc increases the order parameter from 0.21 to 0.26 for this 'plateau' region. As a reference an S_{CD} value of 0.5 corresponds to perfect alignment of the lipid tail to the bilayer normal i.e., the C-^{2}H bonds are fixed in an all trans state. The addition of α-Toc brings the S_{CD} closer to 0.5 meaning that α-Toc is ordering the methylene groups of the phospholipid closest to the headgroup. [101] [102] [103]

In contrast to this α-Toc does not have any impact on the chain-end methyl groups. At 60 °C, the S_{CD} for DPPC alone and equimolar DPPC and DOPC is approaching 0.0 for the end methyl group. The addition of α-Toc does not have any impact on the ordering at these positions. This trend is also mirrored at 25 °C (it should be noted that gel phase spectra cannot be dePaked so the order parameter for DPPC cannot be calculated). The difference in S_{CD} between the DPPC: DOPC and DPPC: DOPC: α-Toc decreases with increasing segment position. This means that although α-Toc has an ordering impact, it is only efficient in ordering methylene groups closer to the phospholipid headgroup region of the membrane bilayer i.e., closer to the outer leaflets. It should be noted that the topological (bond-to-bond) length of DPPC is 27 Å and of α-Toc is 19 Å. If α-Toc's chromane ring anchors itself near to the headgroup region of DPPC, then its length would end near to C-D bond 11 of DPPC (Figure 4.17). This would mean that α-Toc would not be long enough to impart rigidity on segment position 12 and

onwards as reflected in the order parameter (Figure 4.18). Thus the ^{2}H data not only reveals the order inducing ability of α-Toc but also, its likely location within bilayers. [38]

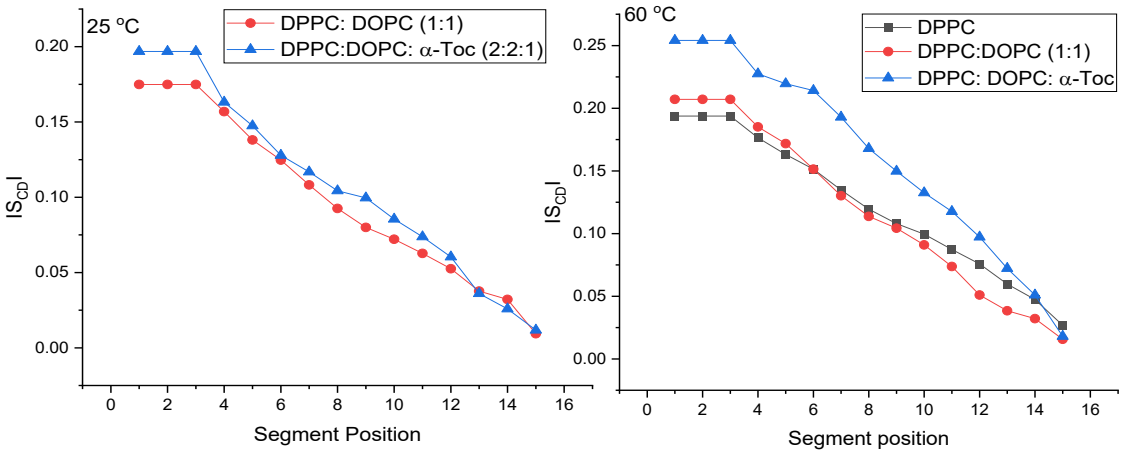


Figure 4. 18 Order profiles for DPPC: DOPC (1:1) and DPPC: DOPC: α-Toc (2:2:1) at 25 C (left) in excess water. It should be noted that order parameters of gel phase DPPC cannot be deduced. Order profiles for DPPC, DPPC: DOPC (1:1) and DPPC: DOPC: α-Toc (2:2:1) at 60 ^{O}C (right) in excess water.

The order profile of ternary mixtures of cholesterol : DPPC :DOPC also shows a similar trend however at a much larger scale (Figure 4.19). Below the transition temperature of DPPC, the addition of 33.3 mol% cholesterol to binary mixtures of DPPC:DOPC results in an S_{CD} value of 0.39. This is much closer to 0.5 meaning the lipid molecules are nearly in an all-trans state. This is confirmation of the formation of the L_o phase. Furthermore, the 'plateau region' is retained until segment position 10, indicating that not only does cholesterol induce order to a greater degree, it also orders more of the length of the DPPC lipid. [104] [26]

Above the transition temperature, at 60 ^{o}C, the ternary cholesterol system yields an S_{CD} value of 0.25. This is the same as the S_{CD} value for α-Toc at 60 ^{o}C. This shows that in highly disordered systems, α-Toc and cholesterol impart the same amount of order on the lipid chains, although cholesterol imparts it deeper into the bilayer.

From the data presented here, it is clear that α-Toc is having some ordering effect on DPPC, although not to the same extent to that of cholesterol. By combining ^{2}H NMR data with the results of phase

seperated GUVs, it is reasonable to postulate the formation of the L_o phase which is perhaps not as large as that which is induced by cholesterol. [76] [105]

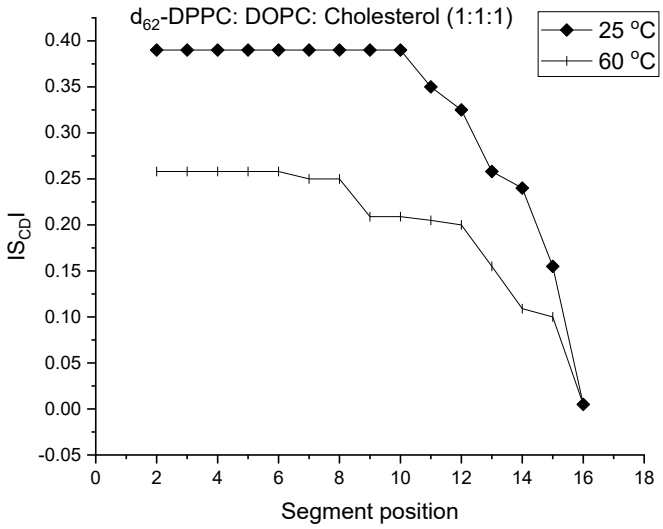


Figure 4. 19 The order profile for DPPC in d_{62}-DPPC: DOPC: CHOL (1:1:1) at 25 °C and 60 °C. Reproduced from Clarke et al. [76]

4.3 Chapter Summary

The data presented in this chapter shows that α-Toc associates with DPPC to form a phase which is more ordered than the fluid phase and less ordered than the gel phase. DSC, WAXS and ^{31}P NMR data show that α-Toc reduces the energy gap between the L_β and L_α phase of DPPC, therefore is either having a fluidising or ordering impact on DPPC, depending on whether the temperature is below or above its gel-fluid transition temperature.

GUVs of α-Toc, DPPC and DOPC show phase separation which is evidence that α-Toc induces lateral segregation within lipid bilayers. It is unknown whether this is fluid-fluid phase separation or fluid-gel, however ^{2}H NMR suggests that a L_o-type phase is likely forming. Therefore, this chapter highlights the similarity of α-Toc to cholesterol in its ability to induce a more ordered phase than the L_α phase.

Chapter 5: DOPC interactions with α-Tocopherol

5.1 Introduction

The phase behaviour of phospholipids can be tuned by several manipulations. The most common is through a change in temperature, pressure or by the addition of molecule(s). This chapter initially focuses on the addition of α-Tocopherol (α-Toc) to an unsaturated phosphatidylcholine, DOPC, and observes the change in phase behaviour using SAXS techniques. The second focus is looking at the phase behaviour of hydrated ternary mixtures of α-Toc, saturated PC (DPPC) and unsaturated PC (DOPC) (Figure 5.1).

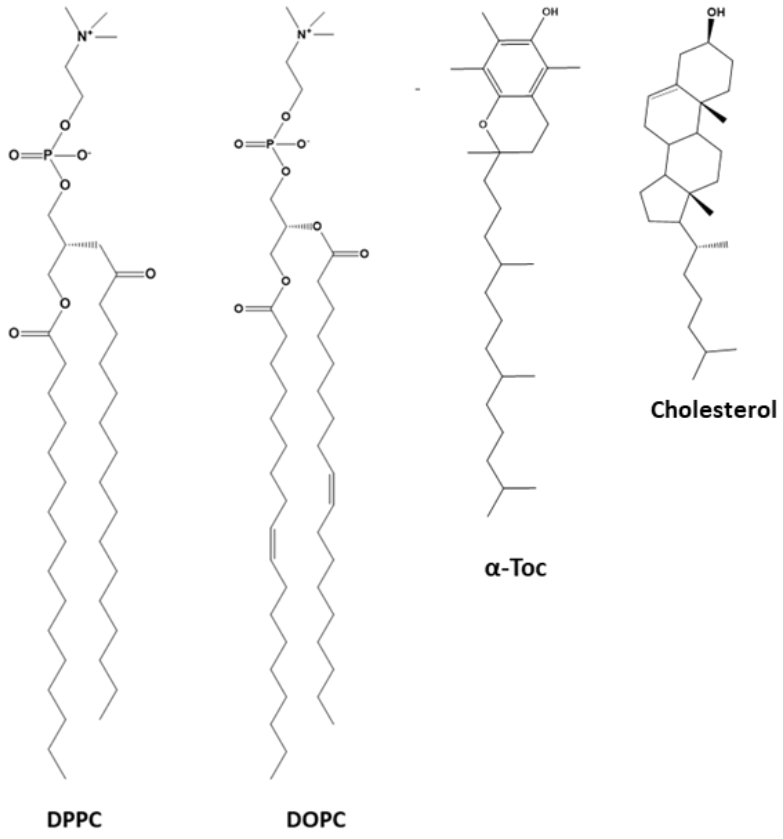


Figure 5.1. Chemical structure of lipids: DPPC and DOPC, α-Toc and Cholesterol

In nature, phosphatidylcholines (PC) are the most ubiquitous lipids in cell membranes, forming an effective barrier separating the inside of a cell from the extracellular environment. To retain this integrity, it is important for PC to retain its structure under a wide range of physiological conditions.

All pure PC lipids form lamellar mesophases at room temperature, but whether fluid (L_α) or gel (L_β) is dependent on the degree of acyl chain saturation. Previous studies have shown that non-lamellar mesophases only form at high temperatures, in saturated lipids, meaning a large perturbation (thermal energy or packing) is required to destabilise the planar bilayers. One molecule which can cause sufficient bilayer perturbation is cholesterol. [106]

Tenchov et al. have reported the formation of Im3m and Pn3m inverted bicontinuous cubic phases at certain compositions of DOPC with cholesterol mixtures.[107] At higher cholesterol content, the H_{II} phase was observed using X-ray diffraction. Other modifiers which have been reported to induce curvature within PC bilayers include limonene and cyclohexane, which form Fm3m and hexagonal phases respectively when added to soybean PC.[108] It should be noted that the compositions at which these phases are formed are unlike physiological conditions in cell membranes. However due to the compositional asymmetry across a membrane i.e., PC and sphingomyelin (SM) lipids being located predominantly on the outer leaflet and phosphatidylethanolamine (PE) and phosphatidylserine (PS) on the inner, spontaneous curvature is naturally induced. The variation in lipid composition, and presence of molecules such as cholesterol, tunes membrane curvature in such a way as to promote cellular processes such as fusion and endocytosis. For this reason, understanding α-Toc's impact on phase behaviour is equally important to understanding it's antioxidant activity. Furthermore, if α-Toc is to be used as an additive in skin, food and drug formulations then it is vital to know what effects on the phase behaviour will be induced by various compositions. [77]

Although the effect of α-Toc on the phase behaviour of lipid membranes is less well known than that of cholesterol, studies have found a membrane curvature inducing impact. Quinn et al. [5] found the appearance of the bicontinuous cubic phase Pn3m at compositions of approx. 15 mol% α-Toc with DLPE, which then transitions into the H_{II} phase. Barauskas et al. [109] reported that higher compositions of α-Toc have a strong influence on the phase behaviour of soybean PC. At a composition of 40 mol% α-Toc, an H_{II} phase was detected using SAXS, whereas at 70 mol% an inverse micellar cubic mesophase,

Fd3m was formed. It was further shown that this Fd3m phase could be dispersed, by sonicating with a secondary emulsifier, into well-defined and stable micellar cubosomes. From the observed broadening of the Bragg peaks, the domain size of these nanoparticles was calculated using the Scherrer equation. It was found that increasing the α-Toc concentration within the Fd3m range, did not have an impact on the lattice parameter but significantly sharpened the Bragg peaks and increased the ordering within a single lipid cubosome. From this it was concluded α-Toc not only promotes local inverse curvature but also has an influence on the long-range order. [108]

This chapter mainly focuses on the interactions of phosphatidylcholines with α-Toc, with the unsaturated lipid DOPC. However, it is useful to first look at previous work of PE with α-Toc to gauge the likely impact on the phase behaviour. X-ray diffraction data of DPPE with α-Toc has shown that the addition of 5 mol% α-Toc results in an α-Toc enriched lamellar phase which is separate to the normal lamellar phase of DPPE. This is indicated by the broad diffraction band on the shoulder to the sharp lamellar peak. At higher temperatures this is then converted to the H_{II} phase. [5 110]

The idea that α-Toc forms enriched domains has been suggested by many previous studies. Ortiz et al. studied the impact on phase behaviour of the addition of α-Toc to equimolar mixtures of DMPC/DSPC. DSC studies showed that the addition of 20 mol% α-Toc broadened and shifted the DSPC endotherm, whereas the DMPC endotherm weakened until it disappeared (as observed with DPPC, see chapter 4). From this it was deduced that α-Toc preferentially interacts with DMPC, which is the lower melting lipid component. Similarly, the effect of α-Toc on equimolar mixtures of saturated PE and PC have been studied. It was found that α-Toc again preferentially partitioned to the more fluid phase. This finding however is contradicted by studies showing that in co-dispersions of DSPC and DLPE, α-Toc preferentially interacts with DSPC, which in this case was the higher melting point lipid. Irrespective of fluidity or chain interaction, it has been repeatedly demonstrated that α-Toc partitions into PC enriched domains as opposed to PE when co-dispersed with PC/PE mixtures. [111 35 69 112 34]

This chapter solely focuses on the interactions of PC with α-Toc. The sequential addition of α-Toc to DOPC was studied by X-ray diffraction, ^{31}P ss-NMR and fluctuation analysis methods. Then the pseudo-ternary (in excess water) phase diagram of DPPC, DOPC and α-Toc was explored using SAXS to distinguish other phases.

5.2 Results and Discussion

5.2.1 X-Ray Diffraction Data of DOPC and α-Toc

Various compositions of α-Toc and DOPC were studied by X-ray diffraction in excess water to determine the effect of α-Toc on the phase behaviour. DOPC alone (in excess water conditions) forms a fluid lamellar (L_α) phase due to the unsaturation in the acyl chains which lowers the gel to fluid transition temperature to below 0°C. This conformation is only altered in extreme conditions (i.e., the addition of certain destabilising molecules or lipids such as PE), as PC molecules have the ability to form a hydrogen bonding network with water which contributes to the stability of the lamellar phase. Furthermore, due to the bulky PC headgroup, DOPC is not readily susceptible to negative curvature. [113] [114] [115]

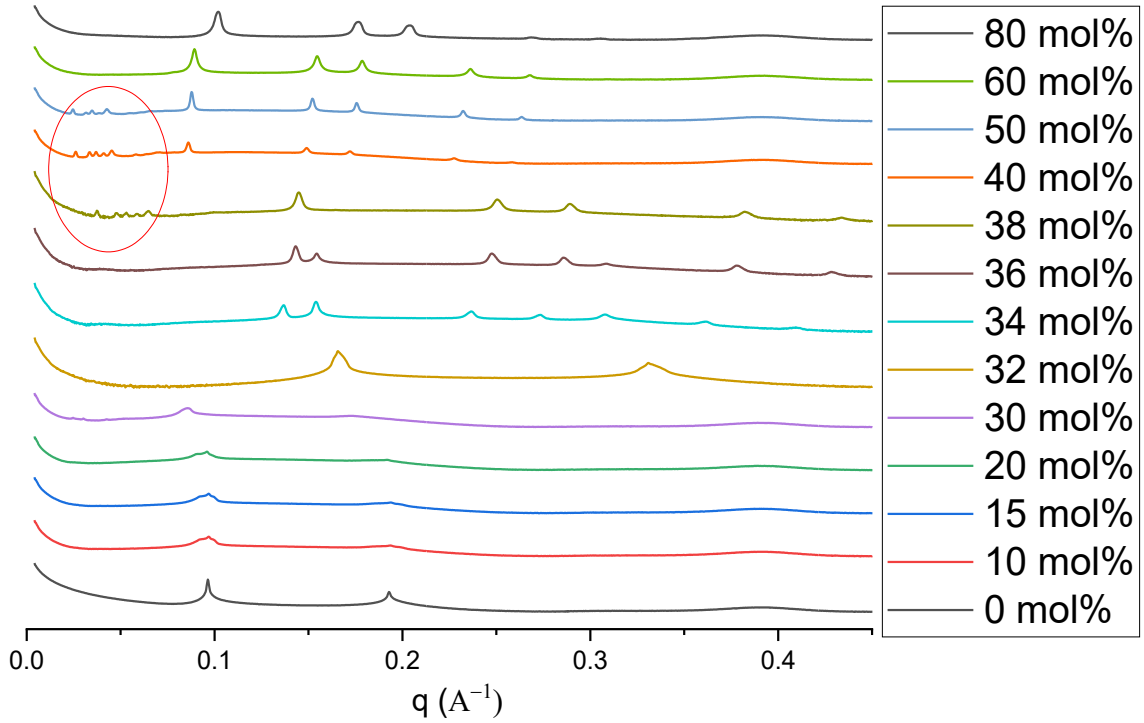


Figure 5.2. SAXS data of DOPC with α-Toc (molar amount of α-Toc given in figure) in excess water conditions at 25 °C. The L_α phase of DOPC can be seen altering with sequential addition of α-Toc. At lower compositions phase coexistence between the H_{II} and L_α phases can be seen whereas higher compositions depict a sole H_{II} phase. At compositions between 38-60 mol% phase coexistence between a H_{II} and a cubic phase (highlighted by the red circle) is also present.

SAXS experiments between 10 – 80 mol% α-Toc with DOPC show significant changes in phase behaviour (Figure 5.2). DOPC alone exhibits an L_α phase with two peaks occurring at q-values of 0.0964 and 0.1928 $Å^{-1}$ which are at the characteristic 1:2 ratio for a lamellar phase. The d spacing is 65 Å which is in accordance with literature values. The addition of 10 mol% α-Toc does not have an impact on the peak positions or d spacing however, a splitting of the peaks can be seen.

At 34 mol% a phase change is observed to the H_{II} phase, which is retained until 40 mol% at which point the d spacing is altered. Additional peaks in the range of 0.01-0.05 $Å^{-1}$ occur for compositions between 38-50 mol% which indicate the presence of a highly swollen phase. In order to analyse the data presented (Figure 5.2) in greater detail, it will be easier to simplify the data into three sections: i) 0-32 mol% α-Toc with DOPC ii) 32-38 mol% α-Toc with DOPC and iii) 38-80 mol% α-Toc with DOPC.

5.2.2 Interactions of 0-32 mol% α-Toc with DOPC

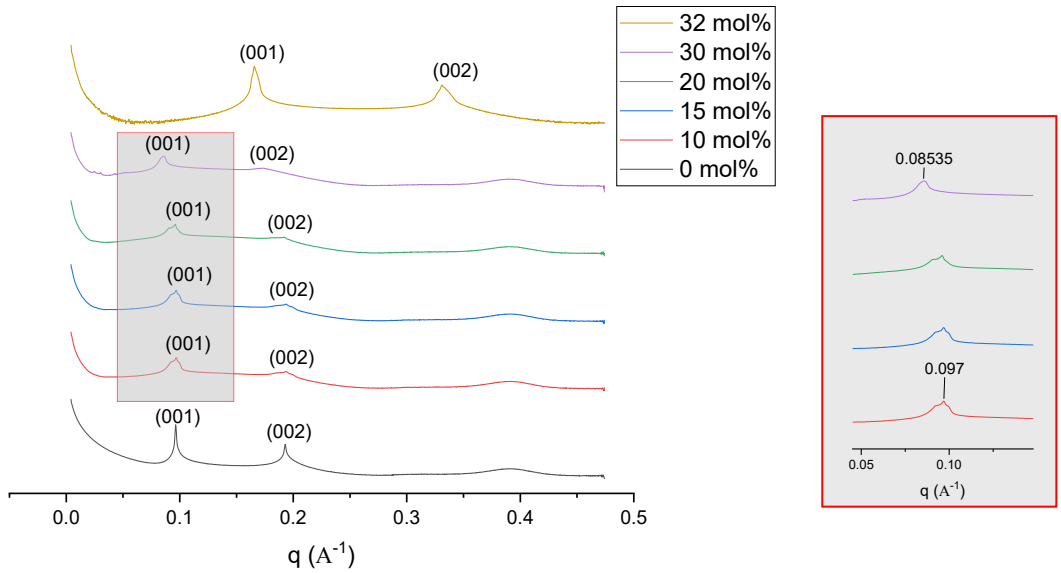


Figure 5.3. SAXS data of DOPC with 0-32 mol% α-Toc in excess water conditions at 25 °C. All plots depict a L_α with the d_{hk} positions labelled. A drastic change in the L_α phase of DOPC can be seen at 32 mol% α-Toc. The box on the right is a zoomed in depiction of the (001) peaks.

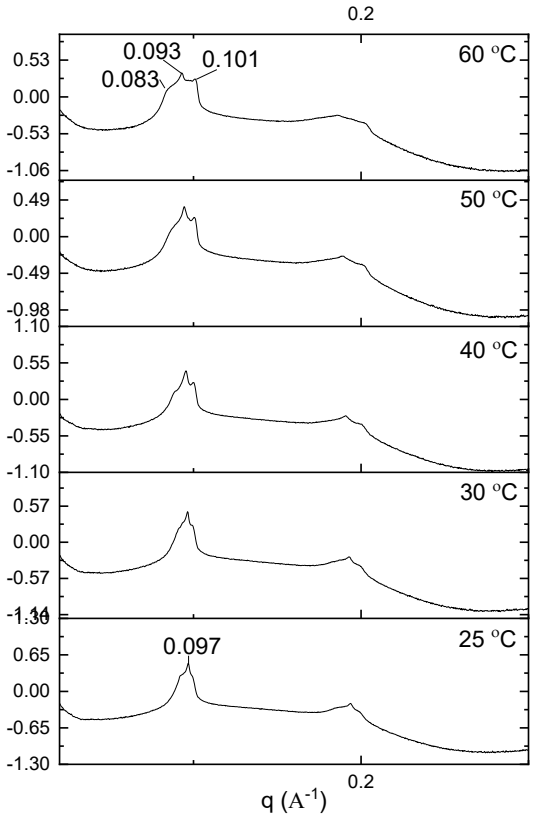


Figure 5. 4 Temperature scan of 10 mol% α-Toc with DOPC in excess water. The broad (001) peak can be seen to split into three separate peaks with increasing temperature.

The L_α phase of DOPC is perturbed by the initial addition of 10 mol% α-Toc (Figure 5.2). The sharp lamellar peaks appear to broaden until 30 mol% α-Toc. A closer look at the d_{10} peak at 10, 15, 20 and 30 mol% α-Toc (Figure 5.3, right) shows the main peak at 0.097 $Å^{-1}$ with a broad shoulder. A temperature scan of 10 mol% α-Toc with DOPC shows that this broad peak at 0.097 $Å^{-1}$ splits into three separate peaks at 0.0928, 0.083 and 0.101 $Å^{-1}$ (Figure 5.4). The peak splitting can be attributed to α-Toc forming complexes with DOPC within α-Toc rich domains. The ability of α-Toc to enable domain formation has been previously explored in the literature.[116] [34] In this case, with DOPC alone, it is reasonable to postulate that α-Toc does not randomly disperse within the DOPC bilayer structure, rather it forms aggregates within α-Toc rich domains which results in a non-homogenous mixture.

The SAXS peak at 0.09282 $Å^{-1}$ (Figure 5.4) is consistent with the lamellar d_{10} peak of DOPC alone (Figure 5.2). From this it can be deduced that the 0.10058 $Å^{-1}$ peak at 10 mol% α-Toc, 60 ˚C is arising from the α-Toc rich domain (Figure 5.4). At a higher composition of 30 mol% α-Toc (Figure 5.3), this α-Toc enriched domain is the dominant diffraction pattern, as a single broad (001) peak centred around 0.08568 $Å^{-1}$ is detected which is retained even at higher temperatures (Supplementary figure SI 5.1). The shift in the q values is indicative of a change in the d spacing.

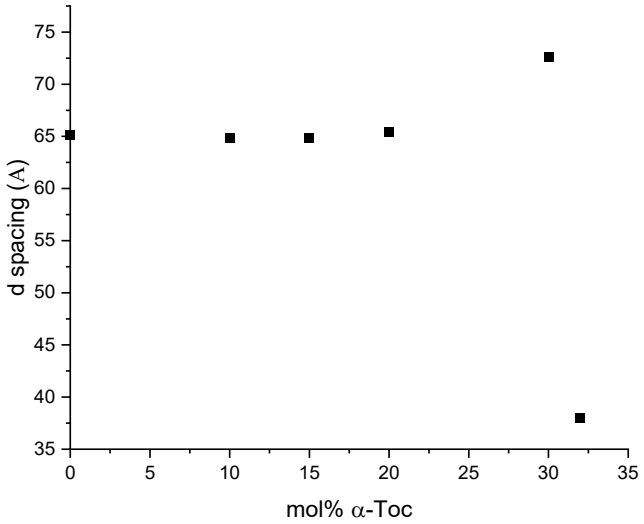


Figure 5.5. The change in d spacing of the L_α phase of DOPC by the addition of α-Toc

Although a lamellar phase is retained at compositions between 0-32 mol% α-Toc with DOPC, the change in d spacing is apparent at 30 mol% (Figure 5.5). Between 0-20 mol%, the d spacing of ~ 65 Å is retained. This may be because the original DOPC phase is the more dominant phase. The addition of 30 mol% α-Toc causes an increase in the d spacing to 72 Å. Simultaneously it can be seen that the d_{10} peak shifts from a peak with a shoulder at 20 mol%, to a single broad peak at 30 mol% (Figure 5.2). This suggests that the α-Toc rich domain is now the dominant domain and initially has a d spacing which is larger than that of the DOPC phase. There is a possibility that the 32 mol% diffraction pattern is indicative of a H_{II} phase with the (11) peak missing. This possibility has been cancelled, as higher compositions of 34 and 36 mol% α-Toc show H_{II} and L_{α} phase co-existence, therefore it is very unlikely for a sole H_{II} phase to form at 32 mol%.

This d spacing drastically decreases at 32 mol% α-Toc to 38 Å which indicates a new L_{α} phase with sharper lamellar peaks and a more compact bilayer (Figure 5.3). This effect has been mirrored by cholesterol on fluid bilayers and is known as the 'cholesterol condensing effect'. Using molecular dynamic simulations, Huang et al. [117] have shown that the average bilayer height significantly decreases at 35% cholesterol with DOPC. It was concluded that the decrease in bilayer thickness was due to the movement of DOPC headgroups towards the bilayer-aqueous interface to protect the hydrophobic cholesterol. [118]

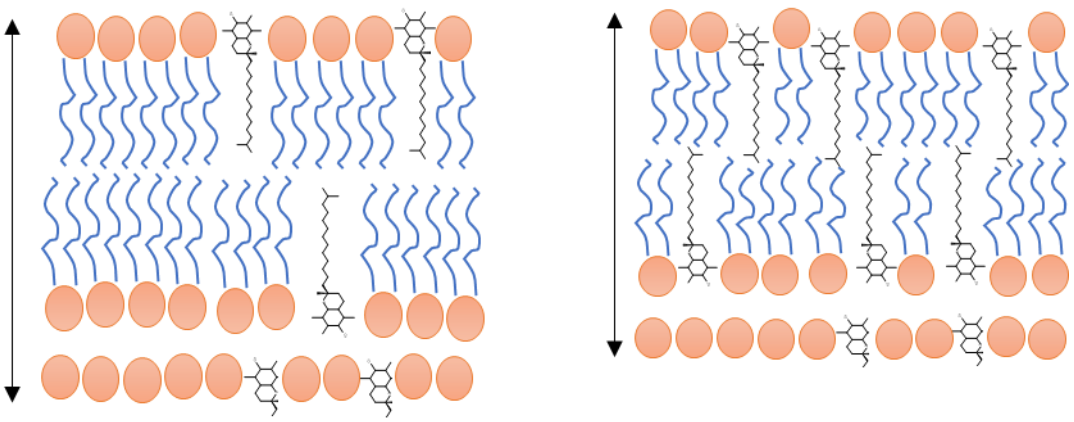


Figure 5. 6 Schematic showing a shift in decrease in d spacing as the a-Toc sit deeper into the bilayer. Hypothetically this could be this could be the conformational structure of 32 mol% α-Toc with DOPC (right), it should be noted that although in this schematic α-Toc is upright, it is likely that it adopts a more curved conformation in reality

Previous work by Marquardt. et al [38] has shown that in unsaturated lipid environments, α-Toc can sit deeper within the membrane depending on the composition (Figure 5.6, right). It could be deduced that the decrease in d spacing at 32 mol% occurs because the new L_α phase is encapsulating the entire α-Toc molecule rather than α-Toc sitting at the interface. To effectively incorporate the molecule within the bilayer, the DOPC molecules need to pack in closer together which results in a decrease in d spacing. This is somewhat reminiscent of the 'cholesterol condensing effect' whereby the surface area of a cholesterol-containing bilayer is less than the sum of the areas of the individual bilayer components.[117]

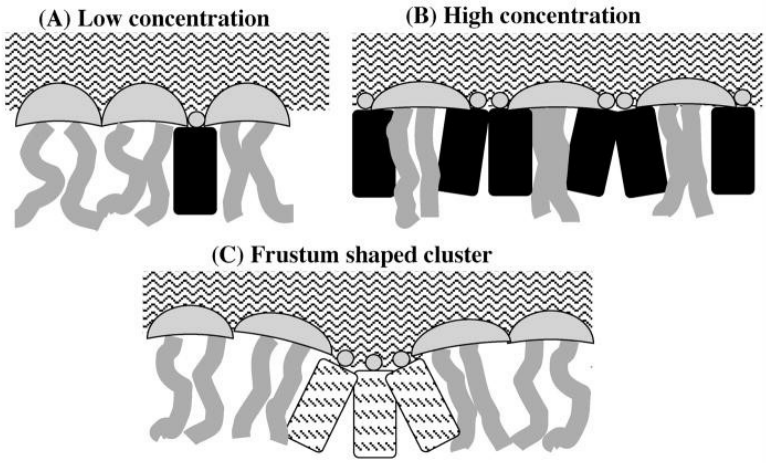


Figure 5.7. The Umbrella model. (A) low cholesterol concentration, PC headgroups can pack together cover the hydrophobic cholesterol body (B) At high cholesterol concentration, headgroups of PCs work together to cover more cholesterol. (C) The frustum shaped cluster: A cholesterol cluster adopts the "frustum shape" to reduce water penetration between cholesterol headgroups. Taken from Huang et al.[119]

Cholesterol decreases the bilayer thickness of the L_d phase while it increases the bilayer thickness of the L_o phase. Therefore, in disordered (unsaturated) PC systems, the 'umbrella model' is repeatedly hypothesised (Figure 5.7). In this, the large headgroups of PC provide coverage as an 'umbrella' to the non-polar bodies of cholesterol by packing closely together. In doing so, cholesterol exerts ordering or a rigidity impact to the lipid chains. It should be noted that the high cholesterol composition 'frustum shaped cluster' is also slightly curved. [120] [121] [122]

It can be hypothesised that the decrease in d-spacing at 32 mol% α-Toc with DOPC is due to the composition adopting an umbrella model- like structure, whereby the α-Toc sits deeper within the membrane (Figure 5.6). This is structurally viable for two reasons i) α-Toc is also non-polar with a

hydrophilic OH moiety which may sit at the lipid-water interface (Figure 5.1) ii) although α-Toc (end-to-end bond length, 19 Å) is longer than cholesterol (15 Å), it is still 'shorter' than DOPC (27 Å) therefore able to sit deeper within the membrane. [123]

To further explore the conformational order within the system, the WAXS data was studied. WAXS data provides an indication of the in-plane packing of the lipid molecules. A broad peak centred around 4.6 Å (1.36 $Å^{-1}$ in q) is indicative of a fluid phase (L_α or L_o). The WAXS data confirms that all compositions of 0-32 mol% of α-Toc with DOPC are in fact the L_α phase as the peak centres for all data are within 1.3-1.4 $Å^{-1}$ (Figure 5.8, left). [49] [124]

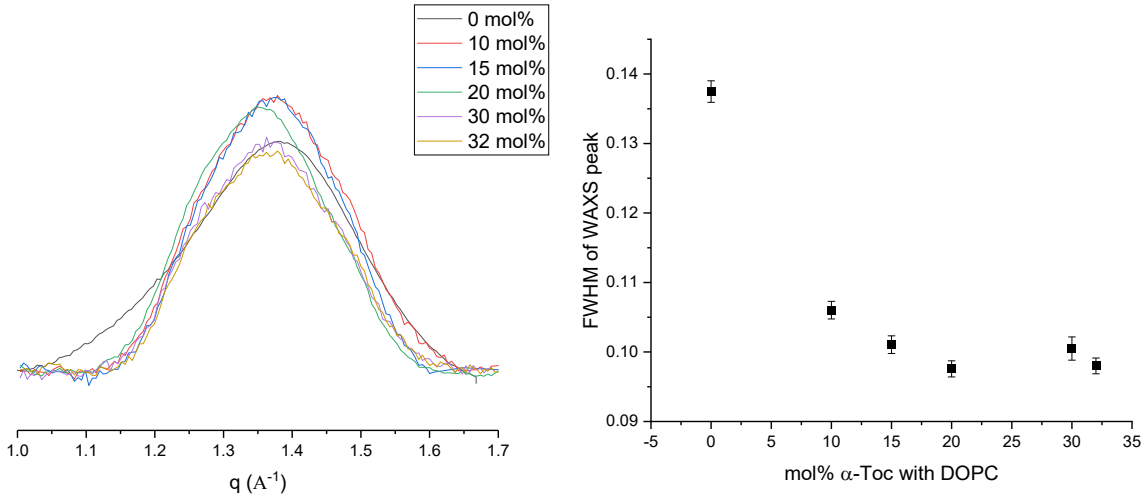


Figure 5. 8 WAXS data of α-Toc with DOPC (conc. of α-Toc on figure) (left). FWHM of WAXS peak with respect to α-Toc composition (right)

Additional information can be derived from the shape of the WAXS peak. In general, a broad peak is observed for L_α phases in the WAXS region because of the level of disorder within a fluid system. In a more disordered system, the acyl chains can move further away from each other, this increases the width of the peak as there is greater variation in the angles of diffraction. For this reason, a plot of the FWHM of the peak against concentration of α-Toc (Figure 5.8, right) provides an indication of the in plane-packing of the system. Although the difference in width is not large, addition of 10 mol% α-Toc does cause a decrease in peak width. This suggests that α-Toc is ordering the system. This would be consistent with the umbrella model theory as the chains would be packing closer together and α-Toc would be imparting rigidity. However, from the X-ray diffraction data it is difficult to conclude which

composition of α-Toc is adopting the 'umbrella-model'. It can be postulated that between 10-30 mol% α-Toc some molecules sit deeper within the membrane and are covered by the umbrella by the DOPC headgroups, therefore imparting rigidity, and some float nearer to the aqueous surface. At 32 mol% it is likely that most α-Toc molecules have adopted the umbrella model. [119] [117]

Another important factor to address when looking at the addition of α-Toc to a L_α bilayer system is the impact on the lateral stress profile. As discussed earlier (Chapter 1.4), bilayer lipids possess an inherent lateral stress profile due to various intermolecular forces. In the case of DOPC, this is counteracted by the ability of PC headgroups to form large hydrogen bonding networks at the lipid-water interface. The addition of α-Toc may disrupt this network. Furthermore, the addition of a non-lipid molecule exerts a stored curvature elastic stress on the bilayer. [14] [125]

Interactions that govern the shape of a lipid are expressed in their lateral stress profile π(z). The lateral stress can be related to the monolayer bending elasticity with the following equation:

$$\kappa_c c_o = \int_0^{d^m} \pi(z) z dz \quad \text{Equation 5.1}$$

where κ_C is the bending elastic modulus and c_o is the spontaneous curvature. This equation shows that the bending elasticity parameter is calculated according to the change in lateral pressure due to the change in curvature of the bilayer. In general, the lateral stress profile is a depiction of the packing constraints within a bilayer structure of the average area per molecules, a_o. The bending rigidity for any deformation, increases as the area per molecule decreases i.e., the addition of a shorter chain lipid to long chain lipid packing would relieve some of the lateral stress. [24] [126] [127]

The bending rigidity is defined as the energy required to bend or deform a bilayer and can be experimentally determined using the fluctuation analysis technique. This technique is also used to calculate the membrane tension which is defined by the force per unit length by which the membrane resists lateral expansion and is therefore a good indication of the stored curvature elastic stress of the bilayer.

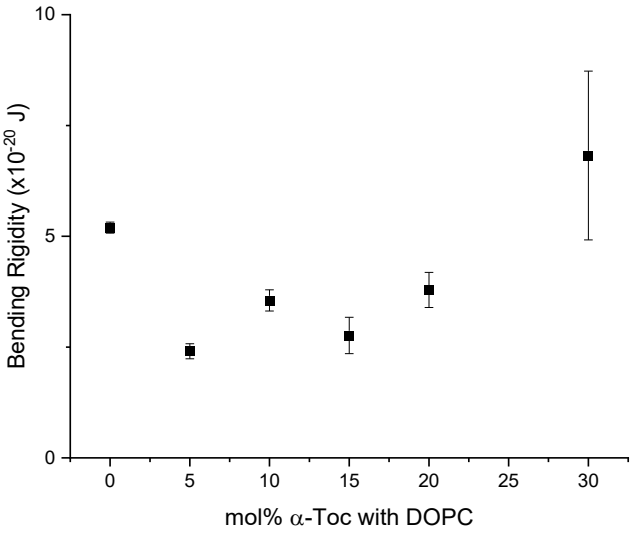


Figure 5. 9 The bending rigidity of GUVs comprised of varying compositions of α-Toc with DOPC. Between 5-20 mol% α-Toc the bending rigidity decreases, at 30 mol% α-Toc the bending rigidity increases.

The bending rigidity for purely DOPC containing vesicles was found to be 5.19 x 10^{-20} J which is slightly lower than the literature value of 8.5 x 10^{-20} J.[128] However, literature values also vary from one another within the same range. The addition of 5 mol% α-Toc decreases the bending rigidity to 2.41 x 10^{-20} J (Figure 5.9) which suggests that α-Toc initially relieves the chain packing stress. Between 10-20 mol% the bending rigidity slightly increases, however is still lower than that of pure DOPC. These results suggest that at compositions of 5-20 mol% α-Toc, the α-Toc molecules are still relieving the lateral stress of DOPC. They can do this by behaving like a short chain lipid, where its chromanol rings are aligned to the phospholipid headgroups in the bilayer (Figure 5.6, left) and its acyl chain is aligned to the phospholipid acyl chains. In this conformation, α-Toc behaves like a short chain lipid, as its length is shorter than that of the phospholipid and can relieve the lateral stress of DOPC by allowing more area for the acyl chains to splay. [25 129 130]

However, at 30 mol% α-Toc the bending rigidity increases to 6.83 x 10^{-20} J, which is higher than that of DOPC alone. This result fits with the earlier hypothesis, that at higher compositions (30-32 mol%) α-Toc adopts an 'umbrella-model' like conformation where the chromanol ring sits beneath the headgroups (Figure 5.6, right). In this conformation the α-Toc is acting more like a long chain lipid and therefore does not relieve the chain lateral stress, rather restricts DOPC acyl chain splay. This increases

the bending rigidity of the system. The large error bars are also to be considered with this measurement (Figure 5.9). These error bars are indicative of other biomechanical properties of the bilayer being more dominant within the system such as the interfacial curvature or membrane tension. This data is based on the GUV with the best fit of the frequency of its oscillations with respect to the amplitude of its oscillation (as a sine wave function), therefore is based on 1 GUV out of around 30 which were analysed at each composition (Supplementary Figures 5.2-5.7). The discarded GUVs showed a deviation from the line of best fit.

A plot of the membrane tension provides further insight on the impact of α-Toc. It should be noted that fluctuation analysis is performed on GUVs, meaning the lipids are forced to adopt a spherical shape despite their preferred conformation. The willingness of the lipid composition to conform is reflected in the membrane tension.

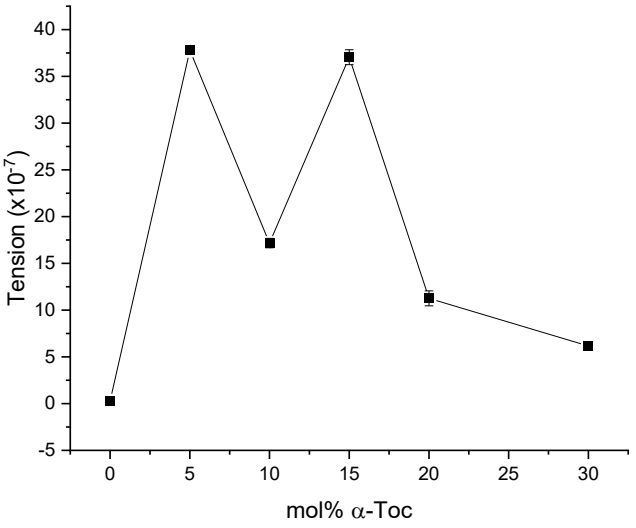


Figure 5.10 The membrane tension of GUVs comprised of varying compositions of α-Toc with DOPC. The line is a guide to the eye.

The initial addition of α-Toc causes an increase in the membrane tension as the bilayer resists the curved GUV conformation. At higher compositions (around 20-30 mol%) the tension decreases meaning the composition prefers to adopt a more curved conformation. The ability of α-Toc to induce curvature in the DOPC bilayer is highlighted further in the next section. [131]

5.2.3 Interactions of 32-38 mol% α-Toc with DOPC

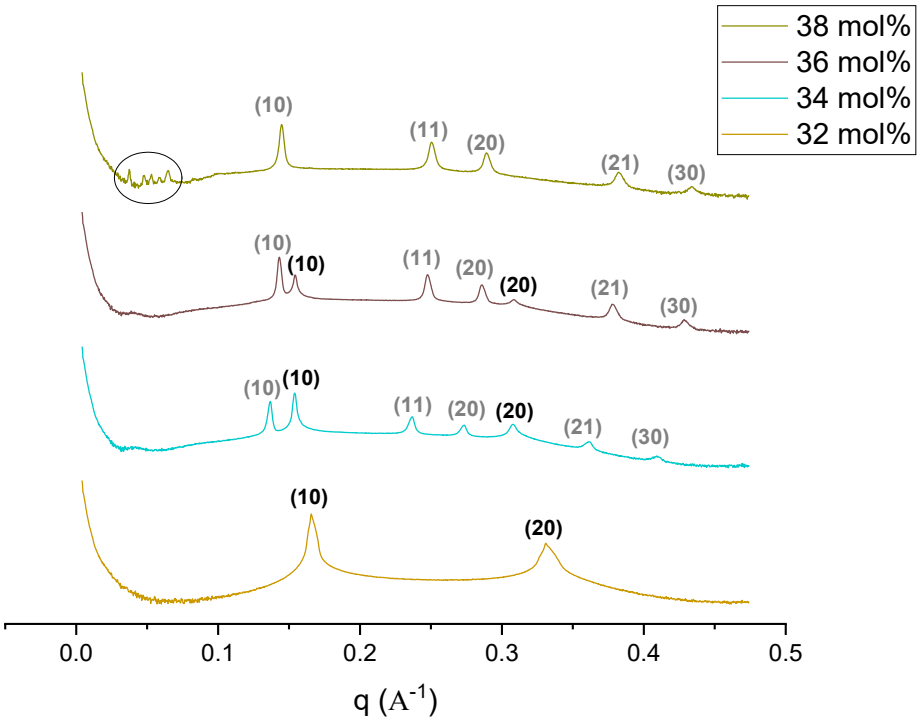


Figure 5. 11 SAXS data of 32-38 mol% a-Toc with DOPC in excess water. Labelled are the corresponding L_α peaks (black) and H_{II} peaks (grey). At 32 mol% only the L_α is present, 34-36 mol% shows phase co-existence of L_α and H_{II} and at 38 mol% it is only H_{II} with additional peaks (circled) corresponding to a cubic phase.

The SAXS data of 34 mol% α-Toc with DOPC shows the emergence of the H_{II} phase which coexists with the L_α phase (Figure 5.11). As the composition of α-Toc increases, the H_{II} phase becomes more dominant, until 38 mol% in which the L_α phase is no longer present. It should be noted that the d_{10} peak for the L_α phase is more intense than the d_{10} peak for the H_{II} phase at 34 mol%. At 36 mol% the H_{II} phase peak is more intense suggesting that this phase becomes more dominant. It should also be noted that the H_{II} phase peaks (particularly at 38 mol%) are relatively sharp suggesting that α-Toc is randomly dispersed within this phase. The ability to of α-Toc to promote curvature within unsaturated lipids has previously been reported widely in the literature. In this instance, it can be hypothesised that α-Toc sits deeper within the bilayer and promotes negative curvature as depicted in the 'frustum shaped cluster' of the umbrella model (Figure 5.7). This in turn induces the H_{II} phase. [112] [132] [30]

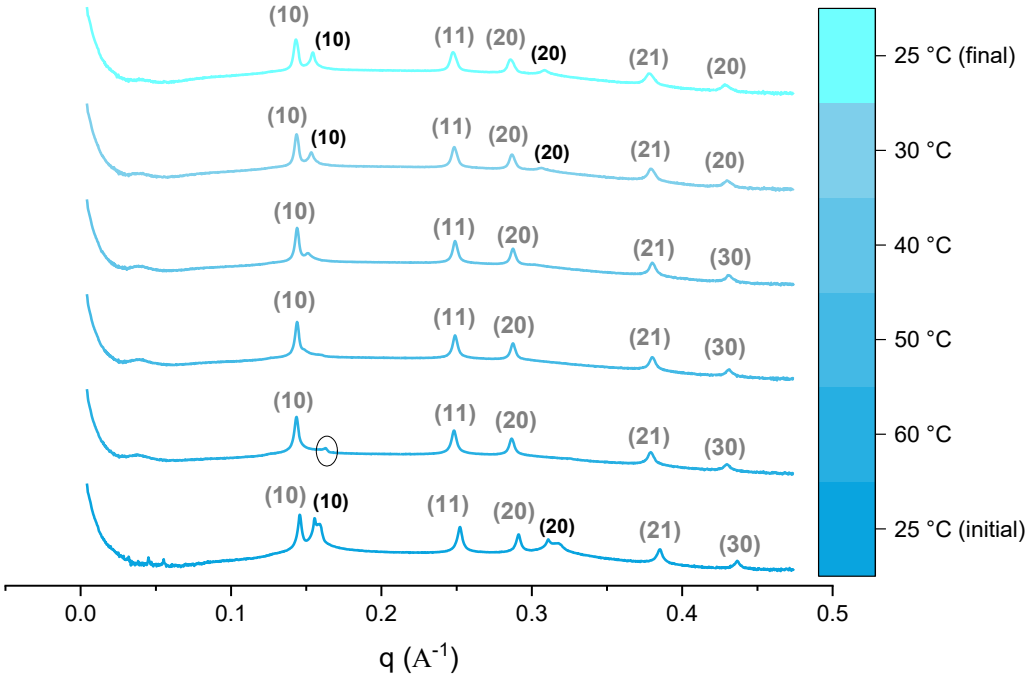


Figure 5. 12 SAXS temperature scan of 34 mol% α-Toc with DOPC. The initial reading was taken at 25C before the sample was heated to 60C and subsequent readings were taken at lower temperatures. Labelled are the corresponding L_α peaks (black) and H_{II} peaks (grey). The L_α only co-exists with the H_{II} at lower temperatures.

The ability of α-Toc to induce the inverted hexagonal phase in lipids has previously been shown by Quinn et al. with lipids such as DLPE, DMPE and DPPE. [34] [112] The phase co-existence of the L_α phase with the H_{II} prior to the formation of H_{II} alone is also consistent with previous findings. This has been attributed to the preferential partition of α-Toc into the H_{II} phase leaving the α-Toc depleted domain of lipids to form the L_α phase. [110]

It is important to note at higher temperatures, the phase co-existence of the L_α with H_{II} which is present at 34 mol%, is diminished (Figure 5.12). The initial reading at 25 ˚C shows phase co-existence of the H_{II} and L_α phase, although the L_α peaks are broad suggesting improper mixing. At 60 ˚C, only the H_{II} phase appears to be present, although a small peak (circled in Figure 5.12) could correspond to the L_α phase, it is highly diminished and not present at all at 50 ˚C. This suggests that at higher temperatures α-Toc disperses more evenly throughout DOPC. At lower temperatures, such as 30 ˚C and 25 ˚C, the L_α phase reappears suggesting it is a thermodynamic product.

At 38 mol% the L_α phase disappears altogether and H_{II} remains. There are however additional peaks occurring between 0-0.5 $Å^{-1}$ (circled in Figure 5.11) which are indicative of a highly swollen phase. These peaks become more apparent in a temperature scan of 38 mol% α-Toc with DOPC (Figure 5.13).

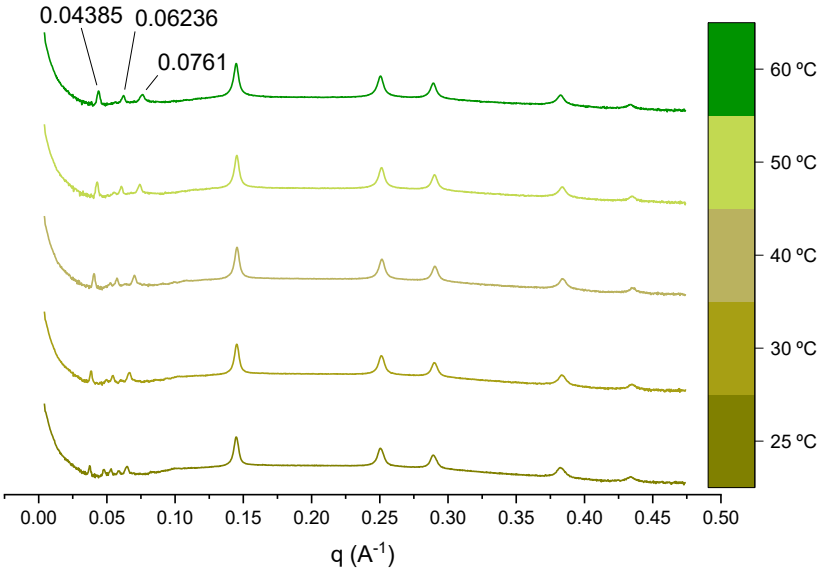


Figure 5. 13 SAXS temperature scan of 38 mol% a-Toc with DOPC (excess water). At 60 ˚C the peaks between 0-0.08 $Å^{-1}$ become more discernible and can be indexed to a corresponding cubic phase.

The peaks occurring in the range of 0-0.05 $Å^{-1}$ are low intensity, however, can be more easily identified at higher temperatures. The three main peaks, occurring at 0.044, 0.062 and 0.076 $Å^{-1}$ become more apparent at 60 ˚C (Figure 5.13). They are in the ratio of $\sqrt{2}$:$\sqrt{4}$:$\sqrt{6}$ which is indicative of the Im3m cubic phase with a lattice parameter a, of 202 Å at 60 ˚C, and 238 Å at 25 ˚C. The indexing of these peaks as a plot of the reciprocal d-spacing ($\frac{1}{d_{hkl}}$) versus m= $\sqrt{(h^2 + k^2 + l^2)}$, fits to a perfectly linear plot which passes through the origin and has a lattice parameter which is reciprocal to the gradient. This is proof of correct indexing to the Im3m phase (Figure 5.14).

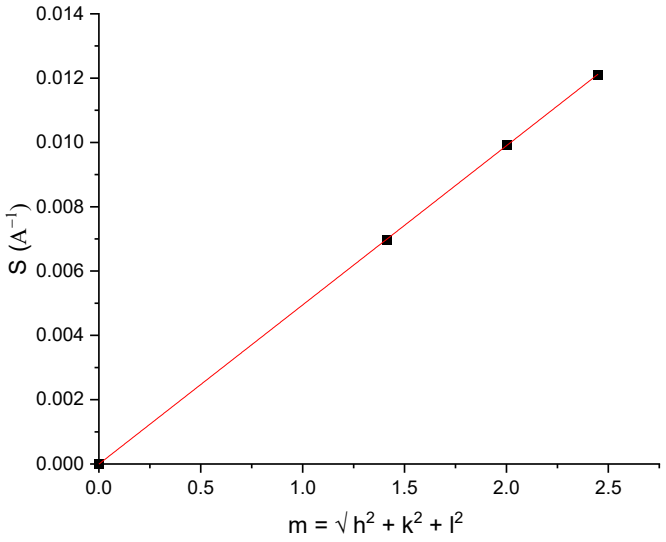


Figure 5. 14 Observed reciprocal spacings vs. $\sqrt{(h^2 + k^2 + l^2)}$ derived from SAXS data, which depicts a perfectly linear plot, confirming the presence of the Im3m phase of 38 mol% α-Toc with DOPC (excess water)

The finding with these SAXS profiles is that at 38 mol% α-Toc the highly curved H_{II} and Im3m phases co-exist. This a novel finding which within lipid systems due to the high energy cost required for both phases to co-exist. The H_{II} is associated to a large packing frustration caused by 'voids' within the structure, which are filled by lipid chains having to stretch or compress away from their optimal conformational state. This has an associated elastic energy cost (Figure 1.9) which can be alleviated by adopting a hexagonal cross-section as opposed to a circular one, however this also involves a packing frustration. [114] [133] [134]

Whilst the Im3m phase does not contain voids, since it is a bilayer draped on an infinite minimum surface, there is still a curvature frustration. This is because the gaussian curvature, K of a saddle structure is not constant along the surface. It is most negative at the saddle point and zero at the apexes, a constant thickness bilayer would have a non-uniform negative mean curvature at the polar headgroups. To counteract this the bilayer could adopt a non-uniform thickness, however in both cases, the energy of the system is raised. It is noteworthy that the co-existence of two different non-lamellar phases is indicative of the phase boundary. The epitaxy between the domains, and the domain boundary, is unclear. [17]

It is remarkable that α-Toc is able to facilitate the formation of both these phases, especially in PC lipids which are typically found in a lamellar conformation (unlike PE lipids which are more prone to curvature). Tenchov et al. have reported that cholesterol also forms the Im3m phase at very specific concentrations and temperatures with DOPC. This phase exists alone however and does not co-exist with the H_{II} phase (although at higher temperatures transitions to the H_{II} phase). From this it was concluded that cholesterol behaves as a membrane 'fusogen'. From the results presented here, it seems as though α-Toc destabilises the DOPC membrane. This destabilisation is required in vivo to facilitate processes such as fusion and protein translocation, therefore α-Toc could play a large role in mediating cellular events. [107]

5.2.4 Interactions of 38-80 mol% α-Toc with DOPC

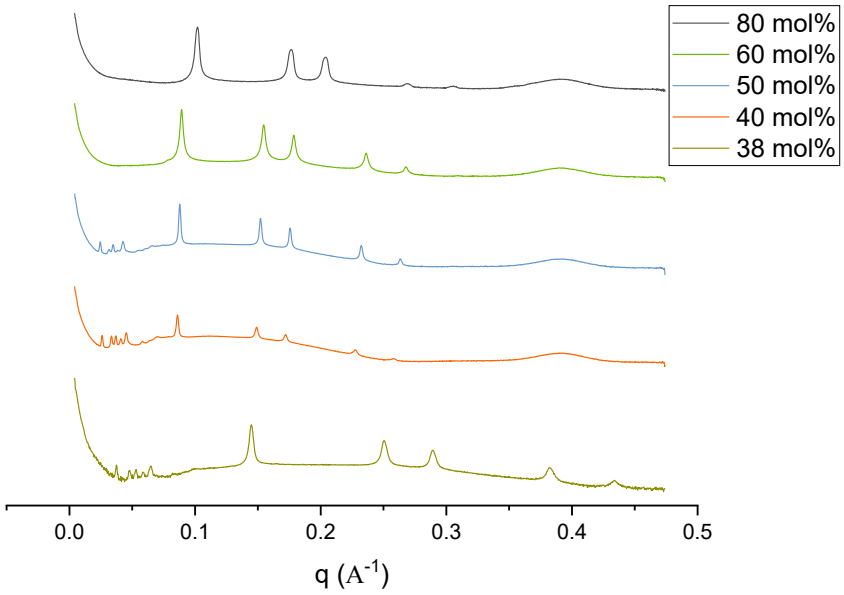


Figure 5. 15 SAXS patterns of 38-80 mol% α-Toc with DOPC in excess water at 25 ˚C

The phase co-existence of the H_{II} and Im3m phase is present up to concentrations of 50 mol% α-Toc in excess water (Figure 5.15). Beyond this point, only the H_{II} phase can be detected at concentrations of 60 and 80 mol%. It should be noted that an isolated Im3m phase has not been detected at any concentration, it only ever co-exists with H_{II}.

Previous work has found that α-Toc can induce cubic phases with other lipid mixtures. Barauskas et al. reported the formation of the Fd3m phase with α-Toc and soybean PC, whereas Quinn et al. have reported the formation of the Pn3m phase with DLPE. However, this is the first time the Im3m phase has been associated to α-Toc and PC. It is interesting that in the compositions studied, Im3m is not isolated, it only exists with the H_{II} phase. However the existence of the H_{II} phase at high compositions of α-Toc is consistent with previous literature comprising of other lipids with α-Toc. [109 112 35]

The lattice parameter of the H_{II} phase does however change between the 38-80 mol% range. An increase in the lattice parameter can be seen at 40 mol% α-Toc which coincides with the increase in the lattice parameter of the Im3m phase at the same concentration (Figure 5.16). This suggests that as the size of the H_{II} phase has an impact on the size of the cubic phase. Between 40-80 mol% the lattice parameter of the H_{II} phase remains fairly constant. However, at 60 mol%, when the Im3m phase is no longer present, the H_{II} peaks become broader (Figure 5.15). This could be attributed in many things such as disordering of the cylinders of the H_{II} phase, or diffusion within the H_{II} system. A common interpretation of line broadening comes from the Scherrer equation is the domain size of the H_{II} phase becoming smaller. It has been previously hypothesised that α-Toc has an impact on the long-range order of a system so this could be a reasonable contributing factor. [109]

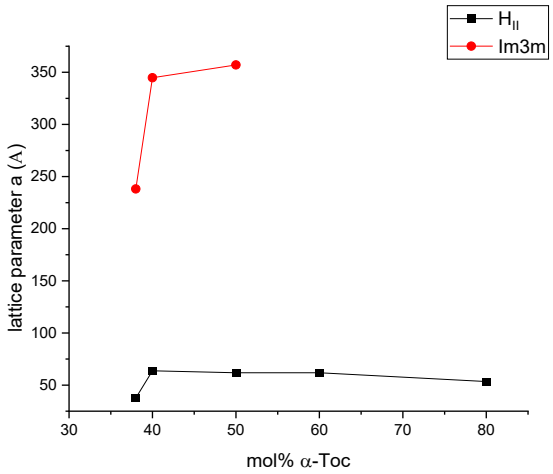


Figure 5. 16 lattice parameter calculation of the H_{II} and Im3m phases formed over the 38-80 mol% α-Toc with DOPC range. An increase in the lattice parameter is seen at 40 mol% for both H_{II} and Im3m phases.

5.2.5 Ternary Phase Diagram of α-Toc, DOPC and DPPC

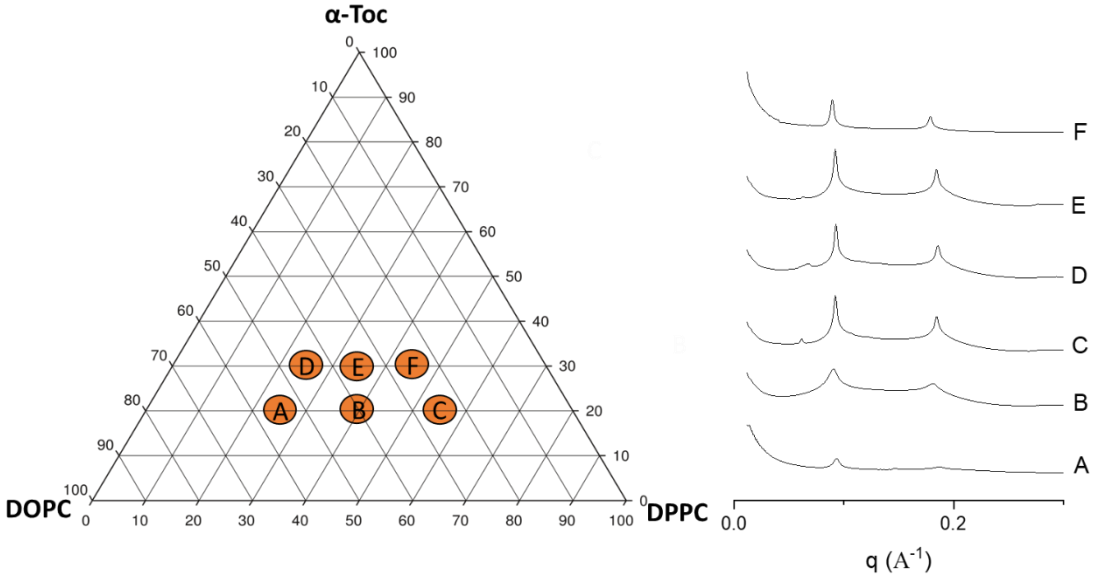


Figure 5. 17 Ternary phase diagram of DPPC/DOPC/α-Toc showing SAXS data of A (5:11:4), B (2:2:1), C (11:5:4), D (5:9:6), E (7:7:6), F (9:5:6) DPPC: DOPC: α-Toc compositions in excess water at 25 °C. All these compositions exhibit a lamellar phase.

The ternary phase diagram of α-Toc, DOPC and DPPC at 25 °C has been studied by SAXS. It has already been shown that compositions of 30 mol% α-Toc and less with DOPC (excess water) forms the L_α phase with SAXS data (Figure 5.3). This is also true for mixtures of DOPC: DPPC at compositions of (1:1), (2:1) and (1:2). The addition of up to 30 mol% α-Toc does not result in a phase change in DOPC and DPPC mixtures as the SAXS plots show a purely lamellar phase with a constant d spacing of 67 Å (Figure 5.17). However, this lamellar phase cannot wholly be characterised as L_α as previous work (see Chapter 4), shows phase separation of what can be assumed to be the L_o phase from the L_α. The compositions at which phase separation occurs has been characterised by fluorescence microscopy of GUVs (Figure 4.13).

At compositions above 30 mol% α-Toc the characteristic H_{II} phase begins to form. At an equimolar composition of DPPC: DOPC, the addition of 40 mol% α-Toc forms the H_{II} alone (Figure 5.18, composition I). At compositions of (1:2) or (1:5) DPPC: DOPC, the addition of 40 mol% α-Toc results in the formation of the H_{II} and Im3m phase (compositions G and H). On the other hand, the addition of

40 mol% α-Toc to a (2:1) composition of DPPC: DOPC forms a weakly scattered H_{II} phase (composition J, Figure 5.18).

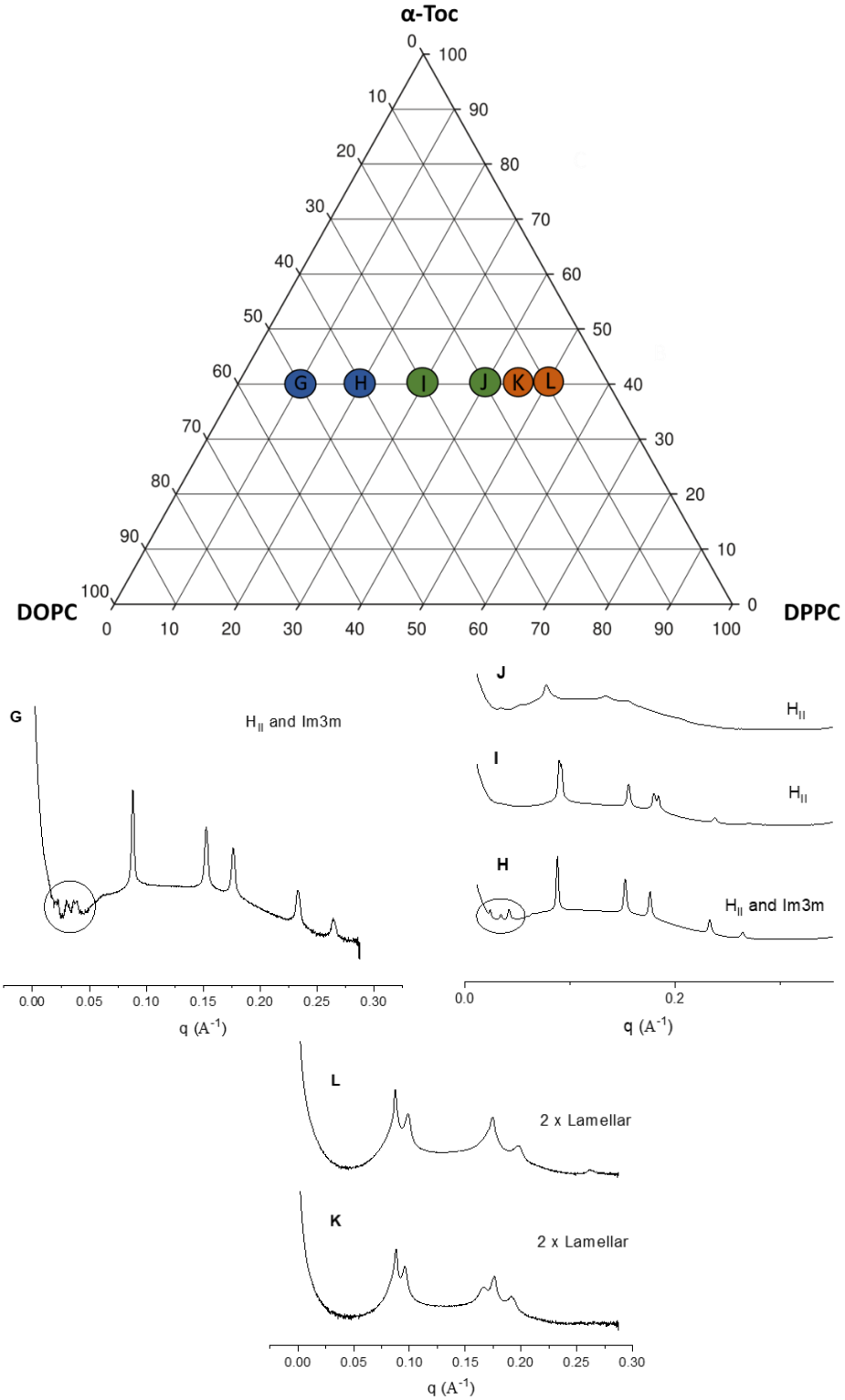


Figure 5. 18 The ternary phase diagram of DPPC/DOPC/α-Toc showing SAXS data of 40 mol% α-Toc with DPPC:DOPC ratio of G (1:5), H (1:2), I (1:1), J (2:1), K (3:1), L (5:1) in compositions of excess water at 25 °C. The H_{II} and Im3m phase co-existence is represented in blue, lamellar in orange and H_{II} in green.

It should be noted that DPPC alone with α-Toc does not form the H_{II} phase, it solely forms a lamellar phase (this is studied by various techniques in the chapter 4). It is interesting that at compositions of 2:1 DPPC: DOPC, the H_{II} phase still forms (composition J, Figure 5.18). The SAXS peaks are however very diffuse, which yields the possibility that a lamellar phase may also be present. This would imply phase separation of DOPC from DPPC to form the H_{II} phase in the presence of α-Toc. This is further shown in composition I, where the molar ratio of DOPC is increased, as the d_{10} and d_{20} peaks of the H_{II} phase are split. The split peaks are at the correct ratio to be indexed to a lamellar phase, so it is reasonable to postulate the phase co-existence of H_{II} and lamellar. However, at higher temperatures these peaks resolve to the H_{II} phase with the emergence of the Im3m phase (Figure SI.5.8). This suggests that above the transition temperature, DPPC does not phase separate from DOPC in the presence of α-Toc. [34 87 134]

The addition of more DOPC to the system (compositions H and G) results in sharp H_{II} phase peaks with co-existence of the Im3m phase without the lamellar phase present. This is expected as the composition of DPPC is considerably lower. At compositions of higher DPPC (compositions K and L), the addition of 40 mol% α-Toc forms more than one lamellar phase. The SAXS peaks for these compositions can be indexed to two lamellar phases suggesting phase separation. This is consistent with the findings of the previous chapter which showed that α-Toc promotes phase separation in GUVs. It is very likely that a disordered lamellar phase has separated from an ordered one.

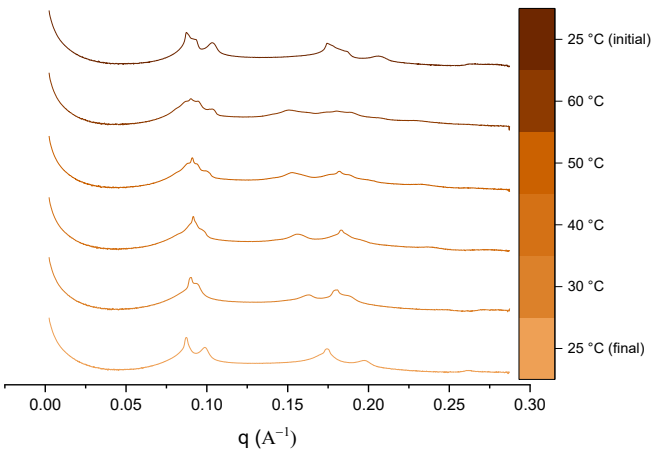


Figure 5. 19 SAXS temperature scan of composition (L) 40 mol% α-Toc with (5:1) DPPC:DOPC ratio. Two separate lamellar phases form which are less distinguishable at higher temperatures.

It is difficult to distinguish which lamellar phase α-Toc associates to however it is reasonable to assume (by combining the results Chapter 4) that the ordered lamellar phase (L_o) is enriched in DPPC (saturated lipid) and the disordered lamellar phase (L_α) is divided DOPC (unsaturated lipid). At temperatures above the transition temperature for DPPC, at 50 and 60 °C, the two lamellar phases become less distinguishable (Figure 5.19). This shows that the difference between the ordered and disordered phases is less, however a completely homogenous L_α phase is also not forming at higher temperatures.

Previous studies have shown that cholesterol promotes the formation of the L_o phase by associating strongly with the saturated lipid (DPPC) and less strongly with the unsaturated.[82] [135] This leaves cholesterol-rich L_o domains and cholesterol-poor disordered domains. Whilst it is difficult to conclude which phase α-Toc has an affinity towards, the SAXS data has shown that α-Toc has a significant impact on DOPC. At equimolar compositions of DPPC and DOPC (composition I), and even at compositions of greater DPPC and DOPC (composition J) the addition of α-Toc results in the H_{II} phase. It can be hypothesised that to induce this curvature, α-Toc must be associating more strongly to DOPC rather than DPPC. This would be congruent with the antioxidant function of α-Toc as unsaturated lipids are prone to oxidation reactions. This is because the double bond located on the lipid chains are more susceptible to reactions with free radicals. [136]

Upon the addition of 50 mol% α-Toc, an equimolar composition of DPPC and DOPC yields a H_{II} phase with sharp peaks, without the presence of any lamellar phase. It is likely that at this composition, the DPPC enriched phase has reached its α-Toc saturation limit and therefore yields an isotropic phase (micelles in solution) which does not appear on SAXS (Figure 5.20). At higher compositions of DPPC (composition O), the expected H_{II} and lamellar phase is present. At higher compositions of DOPC (composition M), only the H_{II} phase is present (although the Im3m phase is likely hidden underneath the noise). The combination of this SAXS data allows for the construction of a ternary phase diagram (Figure 5.21)

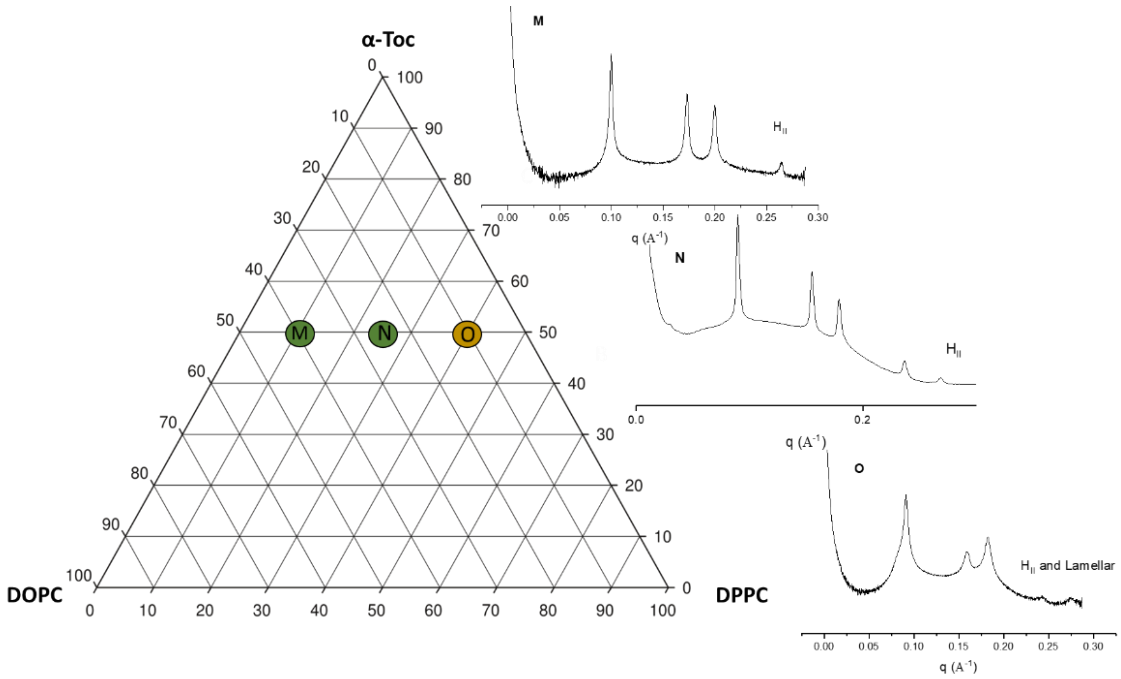


Figure 5.20 The ternary phase diagram of DPPC/DOPC/α-Toc showing SAXS data of 50 mol% α-Toc with DPPC:DOPC ratio of M (4:1), N (1:1), O (1:4) in compositions of excess water at 25 °C. The H_{II} phase is represented in green and lamellar and H_{II} phase co-existence in yellow.

The ternary phase diagram of α-Toc, DPPC and DOPC depicts clearly that α-Toc induces curvature, particularly in unsaturated lipid systems at compositions above 40 mol%. It can be combined with work in the previous chapter to gauge the difference between the lamellar phases at compositions below 40 mol% α-Toc, however more work is required within this area. It is interesting to note that the Im3m phase could not be isolated within this ternary diagram and exists over a small range with the hexagonal phase.

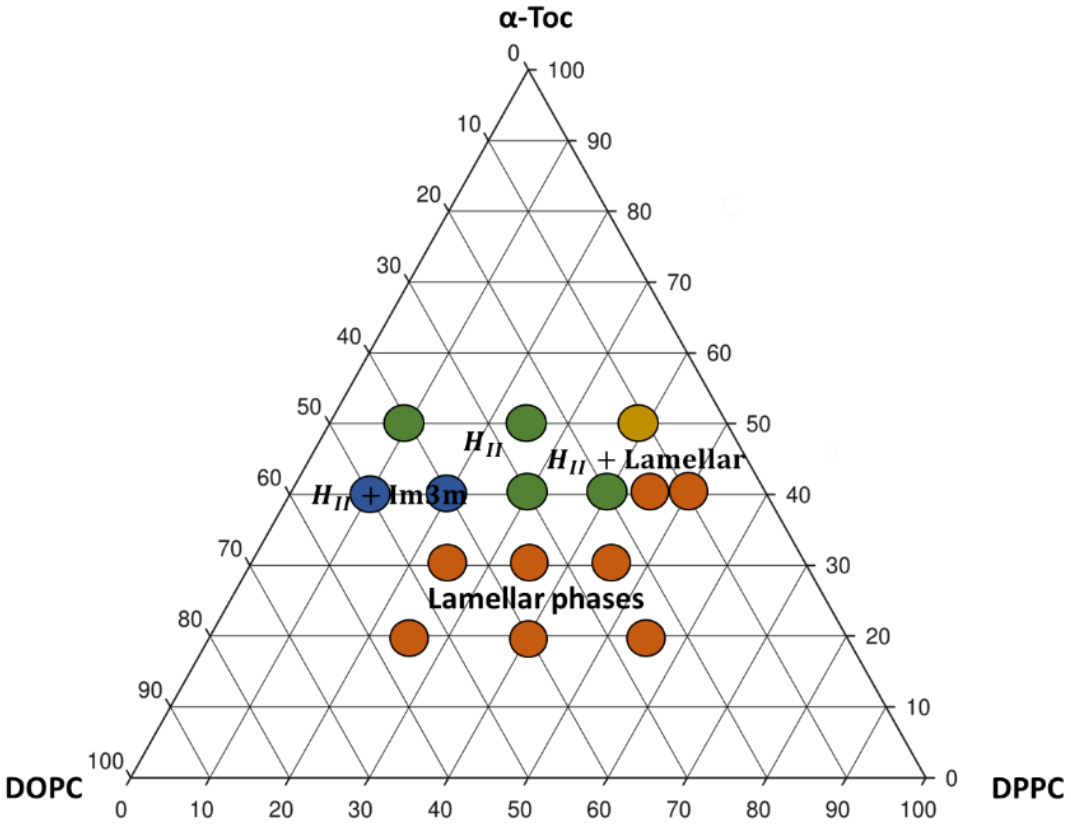


Figure 5. 21 The ternary phase diagram of DPPC/DOPC/α-Toc based on SAXS data in compositions of excess water at 25 °C. The H_{II} and Im3m phase co-existence is represented in blue, lamellar phase in orange, H_{II} in green and H_{II} and lamellar phase co-existence in yellow.

5.6 Chapter Summary

This chapter provides important insights into the phase behaviour of α-Toc with the unsaturated phospholipid, DOPC. The phase co-existence of the Im3m phase with H_{II} highlights α-Toc's ability to induce curvature and accommodate two lyotropic liquid crystal phases which don't typically co-exist over large concentration ranges (only at phase boundaries).

It also highlights the similarities and differences between α-Toc and cholesterol, as α-Toc also seems to be having a 'condensing effect' on unsaturated lipids, however unlike cholesterol, this does not occur over a large composition range with DOPC. Another difference is that cholesterol is often reported to have a preferential association to saturated lipids, it seems as though α-Toc may have a preference to partition into unsaturated lipids. Further work however is required to confirm this.

The ternary phase diagram of DPPC, DOPC and α-Toc provides important insights into the compositions at which curvature occurs. The presence of H_{II}, lamellar and Im3m phases depicts α-Toc's role as a membrane destabiliser. This has impacts in vivo in cellular functions such membrane fusion and protein synthesis but also ex vivo in skin care and food formulations.

Chapter 6: Triolein and DOPE interactions with α-Tocopherol

6.1 Introduction

This chapter explores the impact of self-assembled structures and antioxidants in food systems. Preventing degradation of unsaturated oil-based products is a huge challenge for the food and cosmetic industries. Lipid oxidation adversely affects flavour and quality of food products and could potentially produce toxic reactions. One way to retard peroxidation in oils is by the efficient incorporation of self-assembled products and by the addition of antioxidants. [137]

It has been claimed that bulk oils can no longer be considered fully homogenous liquids, rather water-in-oil nano emulsions, as even refined oils contain small but significant amounts of water and minor components which are amphiphilic. These include monoacylglycerols, phospholipids, sterols, and free fatty acids. It has been shown that these surface-active molecules self-assemble to form aggregates such as reverse micelles and therefore prevent the phase separation of trace water by enveloping it within their core. Previous work has found evidence of these self-assembled structures within bulk oil such as Sosaku et al.[138] found the formation of reverse micelles in fatty acid systems containing soy PC. More recently, Chen et al. [33] found association colloids comprised of DOPC in stripped soybean oil systems; furthermore, the unsaturated phospholipid was found to have a pro-oxidant effect. [32 139 140]

Previous research of oil-in-water emulsions has shown that the water-oil interface plays an important role in the lipid oxidation process since it governs the impact and location of antioxidants and prooxidants. As amphiphilic minor components, such as phospholipids, self-assemble at the interface, the analysis of phospholipids in water-oil systems is important in understanding the reactivity of the

system. Furthermore, the formation of non-lamellar mesophases is of particular interest as these dispersions within bulk oil can be used as delivery systems. [106]

Food oils are primarily composed of triacylglycerol, with monoacyl- and diacyl-glycerides present as minor constituents. The change in phase behaviour by the addition of PC and PE lipids to glycerides is currently very unclear. Unlike monoglycerides, diglycerides themselves do not exhibit lyotropic liquid crystalline behaviour; however, they have been found to influence the behaviour of surface-active lipids. For example, the addition of 60% dioleyl glycerol induces the formation of a reverse micellar Fd3m phase in both fully-hydrated DOPC and DOPE. [106 141 142 143]

Triacyl-glycerides are of particular importance as they are the main constituents of dietary fats. Preliminary work by Lei et al. [144] have analysed the ternary phase diagram of soybean PC, soybean oil and water found that triacyl-glycerides don't modify the lamellar phase of PC. This chapter explores the phase behaviour of triolein with DOPE (Figure 6.1), both in the presence of and without water, by SAXS techniques. Commercial lecithin is often added to triglyceride in food products therefore understanding the effect of different components (like DOPE) is important. Although DOPC and DOPE are both components in food systems which largely impact food reactivity, the interactions of DOPC with triolein have previously been analysed. [33 106]

The addition of α-Toc to this system was then explored to analyse the behaviour of antioxidants. Identifying the best antioxidants or compositions of antioxidant within these systems could be efficient in ensuring the delay of lipid oxidation. The use of synthetic antioxidants such as butylated hydroxyanisole is now discouraged due to concerns of adverse health effects in food. For this reason, natural molecules such as vitamin E (α-Toc) are of great interest in food systems. [37]

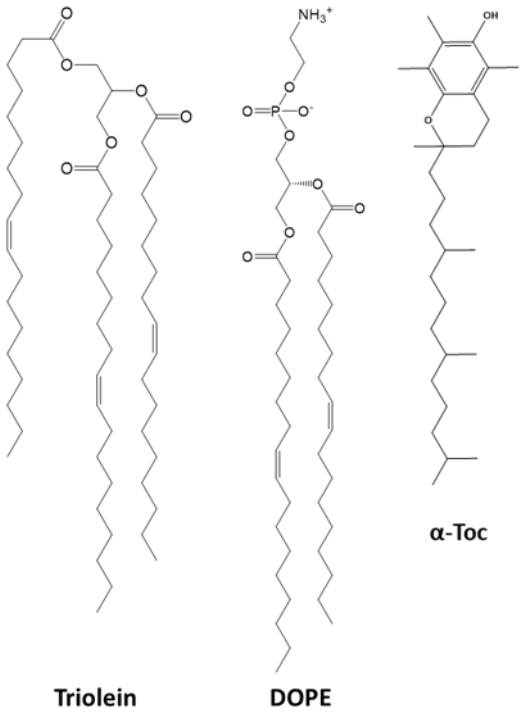


Figure 6. 1 Chemical structures of Triolein, DOPE and α-Toc

The interplay of antioxidants and amphiphiles has been shown to have both synergistic and antagonistic effects depending on concentration and microenvironment. Koga and Terao et al. [29] were the first to demonstrate that phospholipids enhanced the activity of α-Toc in stripped oil containing trace amounts of water. The phospholipid aggregates ensured α-Toc was exposed to the water-lipid interface which was the oxidation site. More recently Chen et al. [145] studied the activity of α-Toc (non-polar) and Trolox (polar) in stripped soybean oil in the presence and absence of DOPC micelles. It was found that at low concentrations of α-Toc and Trolox, DOPC increased the activity of the antioxidants, however at higher concentrations the effectiveness of the reverse micelles decreased. It is unclear how DOPC micelles could increase and decrease antioxidant activity.[146] [32]

This chapter explores the ternary phase diagram of triolein, DOPE and water with SAXS analysis, which is important in understanding food systems which contain both. After this the pseudo-ternary (in excess water) triolein, DOPE and α-Toc system is explored.

6.2 Results and Discussion

6.2.1 SAXS of Triolein and DOPE

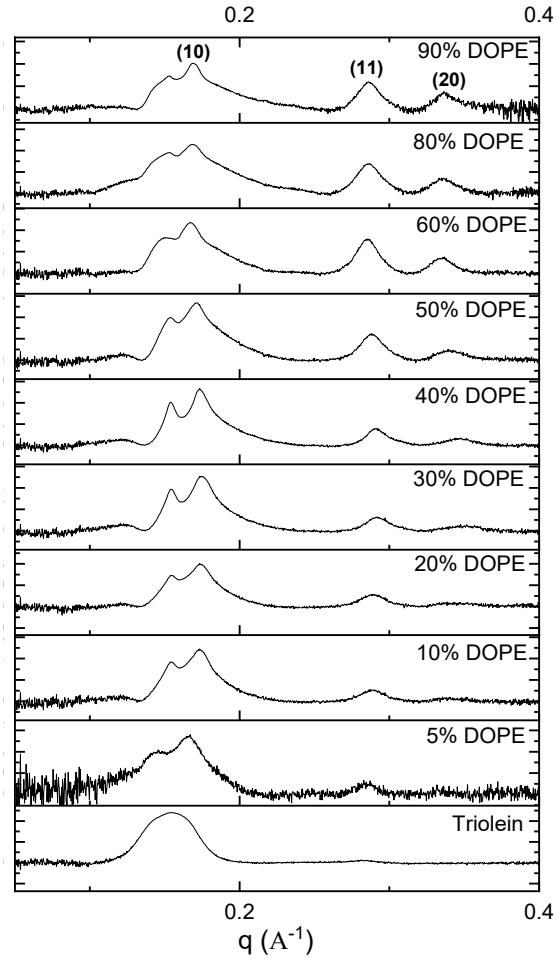


Figure 6. 2 SAXS plots of Triolein with DOPE (without water), showing phase separation of Triolein from the H_{II} phase of DOPE. The H_{II} phase peaks are labelled at the highest DOPE composition however are present in all the compositions containing DOPE.

Triolein alone exhibits a broad diffraction peak centred at 0.15 $Å^{-1}$ in q (40 Å in d). The large peak is indicative of an aggregate structure with a preferred centre to centre distance, however the lack of Bragg peaks indicates there is no long-range order. There have been three proposed structural models for triolein in its molten state: i) a smectic state where triolein forms a lamellar liquid crystalline phase with very loosely stacked bilayers accounting for the lack of Bragg peaks; ii) a nematic state whereby the triolein molecules have orientational order but are not confined to aggregates - this however would require the molecules to behave in a rod-like manner; iii) a discotic model, whereby the chains of a triolein molecule splay into a Y-conformer and assemble into flexible cylindrical rods or columns

via interdigitated stacking. More recently, Rappolt et al. proposed the lamellar TAG (triacylglycerol) assembly model whereby the molecules are stacked back-to-back as 2-D lamellar double layers with another outer layer of loosely attached triolein molecules (Figure 6.4). [147]

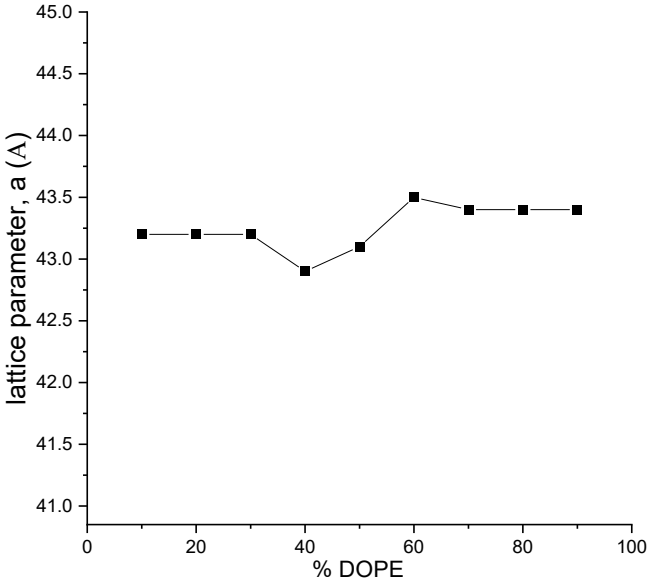


Figure 6. 3 The lattice parameter of the H_{II} phase with respect to percentage DOPE with triolein. There is not much change in lattice parameter with the presence of triolein suggesting phase separation of triolein from DOPE (absence of water). The line is a guide to the eye.

The H_{II} phase of DOPE is well established. The SAXS patterns depict the hexagonal Bragg peaks at 5-90% DOPE composition with triolein (no water) (Figure 6.2). This H_{II} phase with a lattice parameter 43.2 Å remains unchanged with the addition of triolein. Note that this lattice parameter is much smaller than the reported value of 71.9 Å for DOPE in excess water (Reference 22). The lattice parameter of DOPE remains constant at 43.2-43.5 Å suggesting that DOPE is unaffected by triolein addition. This suggests that when water is not added to the system, DOPE and triolein phase separate from one another.

It is however interesting to note that the (11) and (20) peaks of DOPE progressively diminish with the addition of triolein (Figure 6.2). This suggests the H_{II} phase is losing its periodicity as its more immersed within the triolein. If Rappolt et al.'s proposed triolein model is to be accepted (Figure 6.4), then it could be theorised that the pseudo-lamellar structures disrupt the H_{II} packing of DOPE.

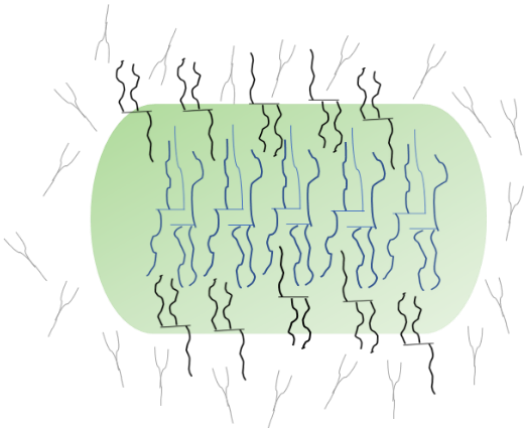


Figure 6. 4 The proposed lamellar TAG assembly model of triolein molecules where each structure (blue, grey and black) is representative of a triolein molecule. Adapted from Rappolt et al.[147]

6.2.2 Interactions of Triolein, DOPE and Water studied by SAXS

To gain a deeper understanding of food systems, the ternary Triolein, DOPE and water system was analysed at varying concentrations by SAXS analysis. It should be noted that although this provides a good indication of overall phase behaviour, it does not account for other interactions such as blister-like oil domains within the bilayer (discussed further in Chapter 7).

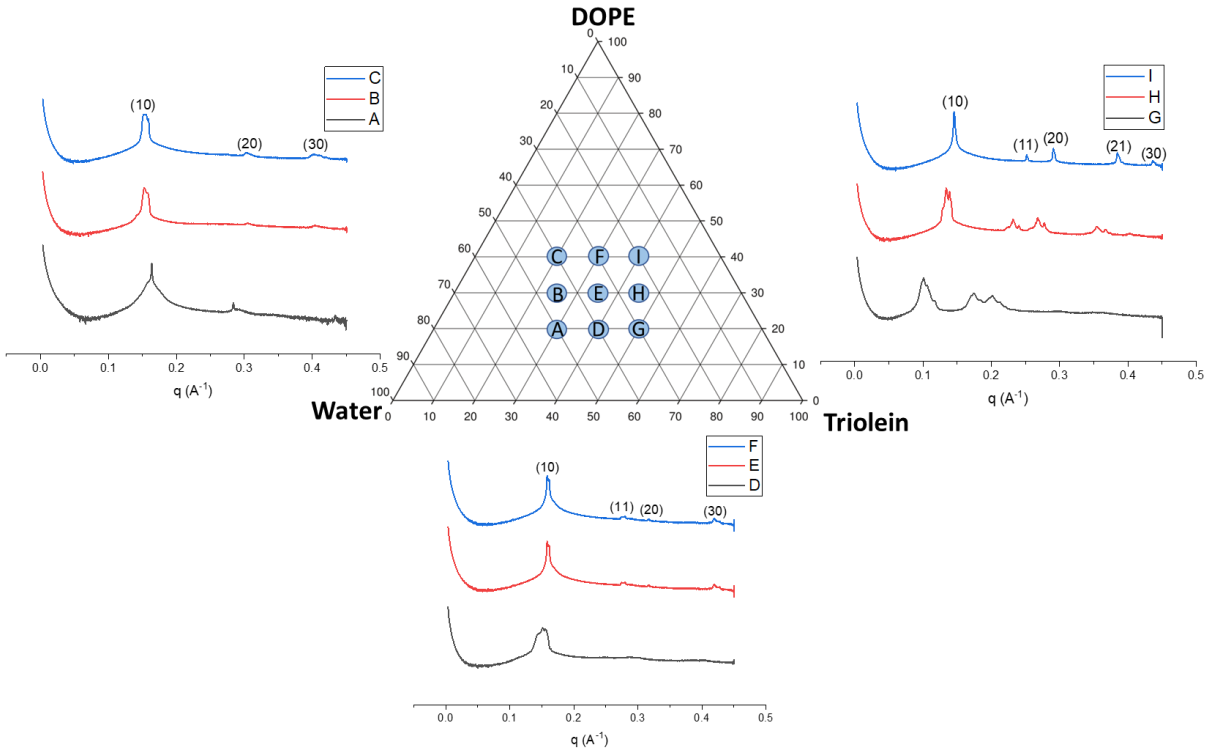


Figure 6. 5 Ternary phase diagrams of Triolein, Water and DOPE (wt%) with corresponding SAXS patterns depicting H_{II} phases. The compositions of Triolein: Water: DOPE is (A) 3:5:2, (B) 5:9:6, (C) 1:2:2, (D) 2:2:1, (E) 7:7:6, (F)3:3:4 (G) 5:3:2, (H) 9:5:6, (I) 2:1:2

The SAXS data at all compositions of DOPE, triolein and water depict a H_{II} phase (Figure 6.5). At equal weight compositions of water and triolein (compositions D, E and F), the addition of 20% DOPE (D, Figure 5.4) results in a single peak at 0.15 $Å^{-1}$ in q (40 Å in d). This peak is broad and occurs within the same range as pure triolein (Figure 6.2) however is asymmetrical. It could be indicative of triolein's self-assembled structure, or an inverse micellar structure (L_2) formed to separate the water from the oil. The shape of the peak indicates a broad peak superimposed on a (10) hexagonal Bragg peak. The addition of 30 and 40% DOPE (compositions E and F) form a H_{II} phase in which the (11), (20) and (30) peaks are largely diminished. This can be attributed to a disordering impact of triolein to DOPE, in the presence of water, which is likely causing a loss of periodicity.

At compositions in which the water ratio is higher than that of triolein (compositions A, B and C), the addition of 20, 30 and 40% DOPE results in a large peak centred around 0.15 $Å^{-1}$ with an additional peak occurring at 0.3 $Å^{-1}$ (Figure 6.5) The indexing of these peaks would result in a lamellar phase however this could be inaccurate. As results have shown that the (11) and (20) peaks of the H_{II} phase diminish with the addition of triolein, it is likely that intensity of the (11) Bragg peak is undetectable. Consequently, it can be deduced that the H_{II} phase is still forming, as binary DOPE and water forms H_{II}, however triolein is largely broadening the peaks. [20] [148]

The broadening of the Bragg peaks can be attributed to triolein disordering the periodicity of the lyotropic liquid crystal phase and damaging the degree of long-range order. If the lattice is broken-up, however local order is still present in the system, the SAXS pattern still depicts Bragg peaks which are broad. As a result, weak intensity peaks, such as the (11) peak, disappear into the noise.[20]

At compositions in which the triolein ratio is higher than that of water (compositions G, H, and I), the addition of 40% DOPE (composition I) results in sharp Bragg peaks which can clearly be indexed to the H_{II} phase. A decrease in DOPE content (composition H) results in broadening and splitting of the peaks. The splitting could be indicating two separate hexagonal phases: a water-rich H_{II} phase (water

molecules encapsulated at the core) and an oil-rich H_I phase (triolein molecules encapsulated within core). A further decrease in DOPE composition (composition G) results in further broadening of the Bragg peaks which still appear to be split. The lattice parameter also drastically increases from composition H to G as the composition of DOPE decreases (Figure 6.6). An increase in the lattice parameter in the H_{II} phase is congruent with a release in the packing stress (Figure 1.9). This is likely because a lower composition of DOPE results in enough triolein composition to sit within the H_{II} phase voids and relieve the stress.

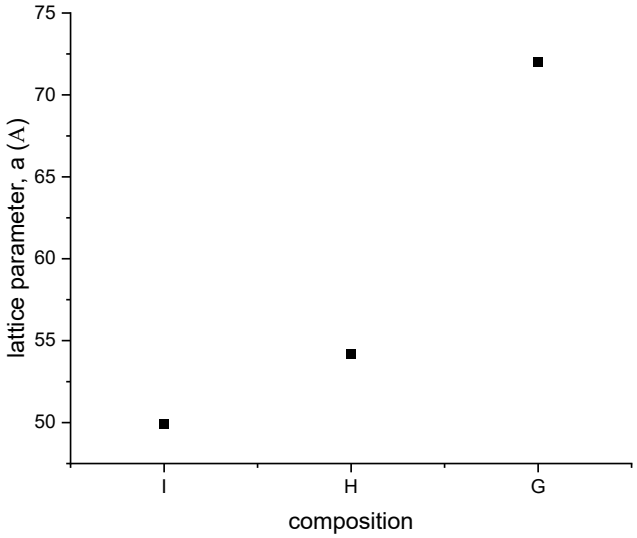


Figure 6. 6 The lattice parameter of the H_{II} phase at compositions I (2:1:2), H (2:1:1.3) and G (2:1:0.8) (Triolein: Water: DOPE). The lattice parameter is increasing as the DOPE: Triolein ratio is decreasing i.e., an increase in triolein content causes an increase in the lattice parameter.

It should also be noted that composition I has a lattice parameter of 50 Å, whereas compositions C and F have a lattice parameter of 46 Å (Figure 6.5). This again shows that increasing the triolein composition causes an increase in the lattice parameter. Additional SAXS measurements of compositions of the ternary phase diagram of triolein, DOPE and water were also taken at higher DOPE compositions. At these compositions, a well-defined H_{II} phase is seen (Supplementary Figure 6.1) and the lattice parameter ranges between 45-55 Å. At compositions in which the triolein content is higher than that of water (compositions P and Q, Supplementary Figure 6.1), the Bragg peaks are more diffuse and the (11) peak is again almost indiscernible.

6.2.3 Polarising Microscopy of Triolein and DOPE (in excess water)

SAXS data of various concentrations of triolein with DOPE in excess water have also been recorded (Supplementary Figure 6.2). In most cases an intense peak is apparent which can be attributed to the (01) peak of the H_{II} phase with peak broadening at higher compositions of triolein. The X-ray data depicts that triolein does not change the phase of DOPE, however in the presence of water, triolein and DOPE do interact with each other.

Lower compositions of triolein with DOPE in excess water have also been visualised by polarising microscopy. This is a technique in which birefringent samples can be analysed due to a change in polarisation state of the light by the samples. As liquid crystals are frequently anisotropic materials, they can polarise the light so it can pass through the analyser. [149]

Pure DOPE, 90% DOPE with 10% triolein and 80% DOPE with 20% triolein (wt%) in excess water were visualised under a polarising microscope (Figure 6.7). The image for pure DOPE is not indicative of any lyotropic liquid crystal phase although it is known by SAXS that the H_{II} phase forms. It is the image of 80% DOPE with triolein (excess water) which most clearly. depicts the presence of a H_{II} phase. The fan like structures are characteristic of the optical texture of an anisotropic H_{II} phase.

These images suggest that triolein improves the optical texture of the DOPE H_{II} phase by lowering the relaxation energy needed for elastic deformations such as bending, splaying, and twisting to occur. These deformations soften the 'stiffness' of a rigid H_{II} phase which is in fact optically isotropic in the x-y plane as the incoming beam of light encounters the same environment in every direction. Triolein reduces the viscoelasticity of this H_{II} phase and therefore helps to develop the characteristic optical texture. [150]

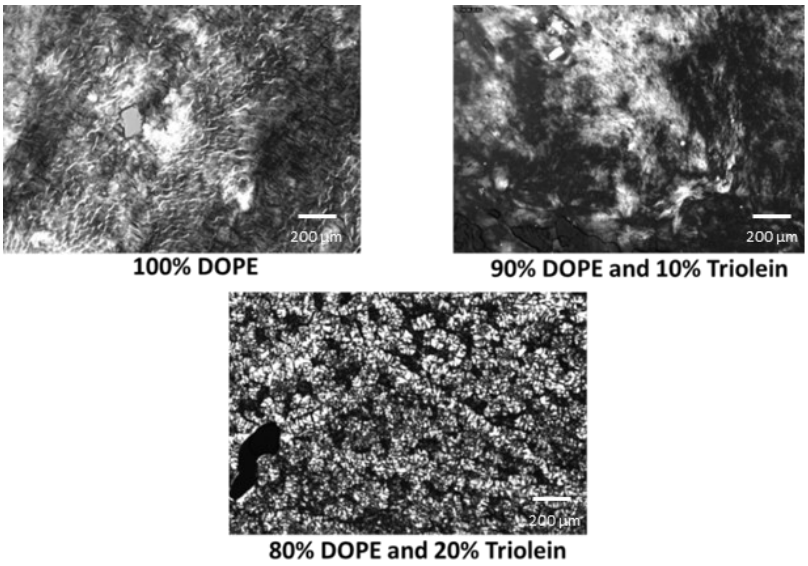


Figure 6. 7 Polarising microscopy images of DOPE with Triolein in excess water at 25°C.

6.2.4 SAXS of Triolein, DOPE, and α-Toc (excess water)

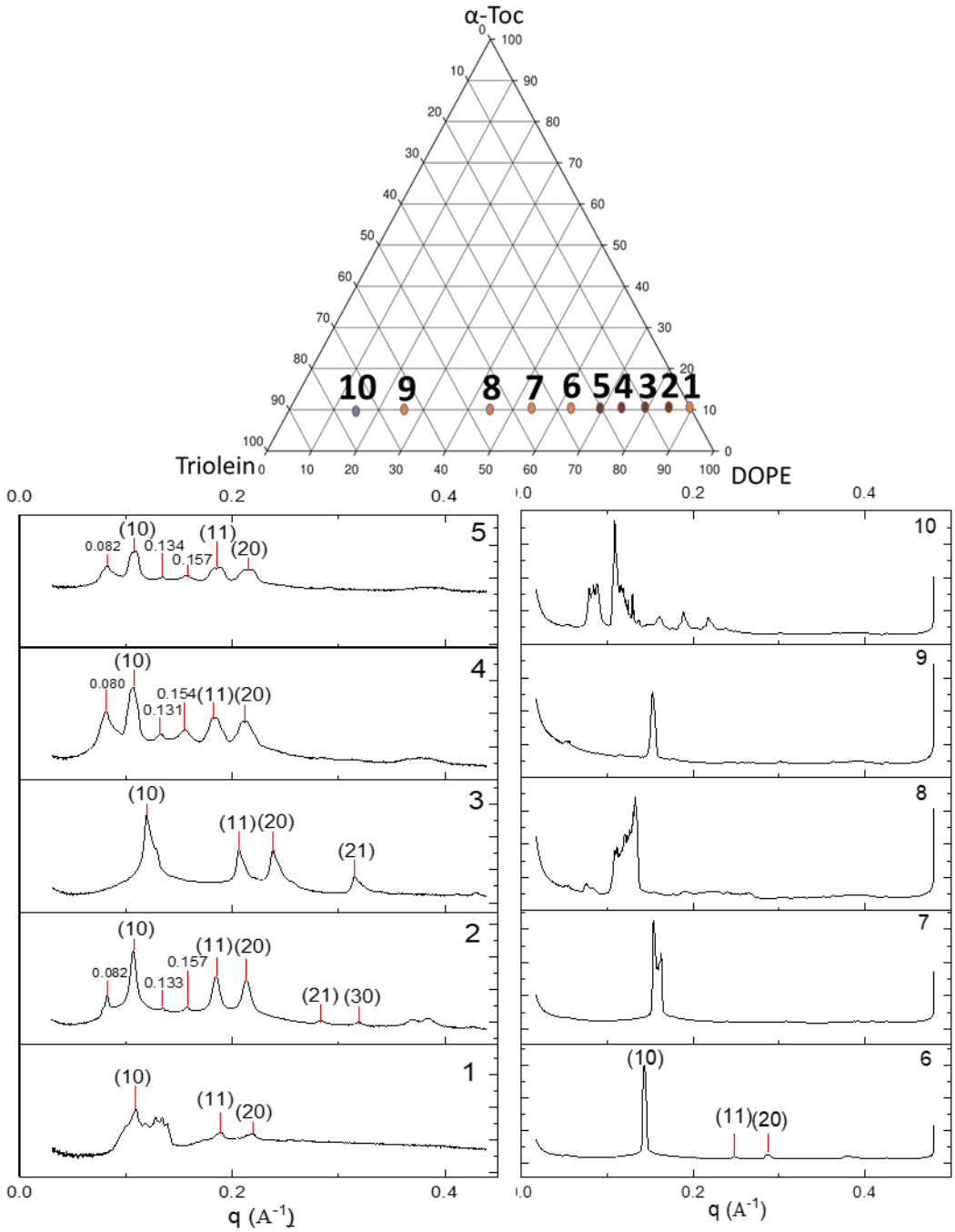


Figure 6.8 SAXS profiles of compositions of α-Toc, DOPE and Triolein (excess water, at 25 °C) with compositions depicted in ternary phase diagram (top). The proportion of α-Toc is constant at 10 mol% with varying amounts of DOPE: Triolein, (1) 90:0, (2) 85:5, (3) 80:10, (4) 75:15, (5) 70:20, (6) 62:28, (7) 53:37, (8) 45:45, (9) 26:64 , (10) 15:75 (mol%). The H_{II} phase has been labelled with its corresponding Bragg peaks whereas some additional peaks are labelled with their q values which can be indexed to the Fd3m phase. The orange represents the H_{II} phase, brown represents H_{II} and Fd3m phase co-existence and the grey represents the hcp phase.

The addition of α-Toc to the triolein and DOPE system is important in understanding how various components impact a food system. In this case, the phase behaviour has been analysed within a ternary phase diagram, at various compositions by SAXS analysis. The system was initially explored at

10 mol% α-Toc with varying compositions of DOPE: triolein (Figure 6.8). At a composition of 10 mol% α-Toc with 90 mol% DOPE (composition 1, Figure 6.8), the SAXS profile can be indexed to a H_{II} phase with additional peaks. These additional peaks are assigned to a phase further on within this chapter. The presence of these additional peaks however depicts that at even low compositions, α-Toc interacts and alters the phase behaviour of DOPE.

The addition of 5-20 mol% triolein to the α-Toc: DOPE system results in a more discernible H_{II} phase wherein the Bragg peaks can easily be assigned (Figure 6.8, compositions 2-5). The lattice parameter of this H_{II} phase remains constant at 66 Å, however increasing amounts of triolein does result in peak broadening depicting disordering of the H_{II} phase (composition 4 and 5). Additionally, three peaks occurring at 0.08, 0.13 and 0.15 $Å^{-1}$ can be seen at compositions 2,4 and 5. These peaks can be tentatively indexed to the cubic Fd3m phase suggesting the phase co-existence of a H_{II} and Fd3m phase (Figure 6.9).

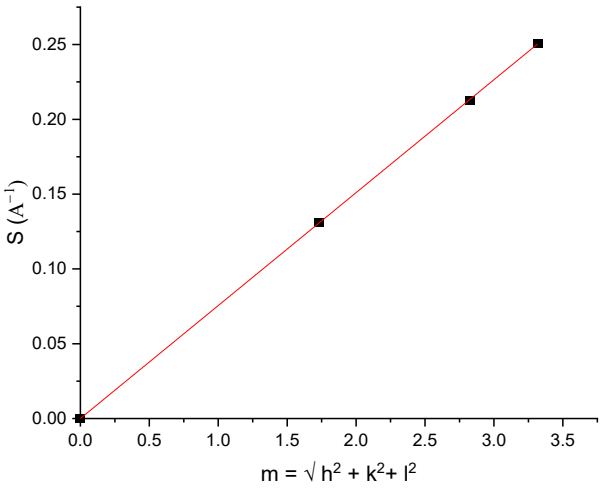


Figure 6. 9 Proof of the formation of the Fd3m phase from the additional Bragg peaks (equation from Table 2.1)

The Fd3m phase has previously been associated to α-Toc, however this was in soybean PC/water systems (without the presence of an oil) as reported by Martiel et al. [108] The formation of this phase was attributed to α-Toc inserting itself into the lipid-water interface and comprising of a bulky apolar moiety (Figure 6.1) which induces negative spontaneous curvature, forming small inverse micelles. These small inverse micelles assemble into an Fd3m phase which is considered the best compromise

between micelle packing, lipid tail frustration and interfacial curvature. This phase has a packing fraction for hard spheres of PF=0.71, which may be compared to face-centred cubic (*fcc*) or hexagonal close packing (*hcp*), both of which have a packing fraction for hard spheres of PF=0.74 (Figure 6.10) .
[151]

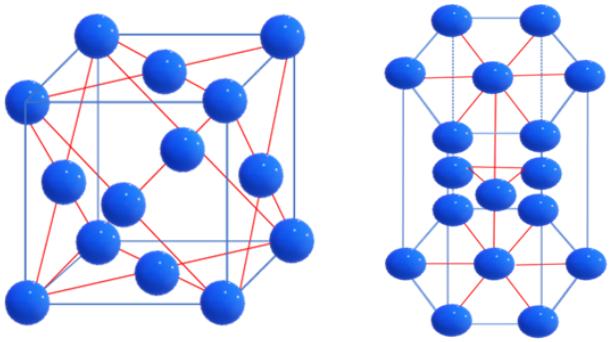


Figure 6. 10 Face centred cubic (fcc) and hexagonal close packed (hcp) conformations with a packing fraction of 0.74. In this case the hard spheres represent micelles or inverse micelles.

Although Chapter 5 has reported the phase co-existence of a hexagonal and cubic phase induced by α-Toc, this in general is rare. The Fd3m phase is coexisting with a H_{II} phase, and these phases only become apparent with the addition of triolein to the system. This is an indication of α-Toc's ability to separate water from oil as these phases can encapsulate the triolein within the cores. Not only does α-Toc intercept the free radicals produced from oxidation reactions, this SAXS data shows it is also a phase modifier which physically separates oil from water. The addition of lipids and α-Toc at the correct compositions in food systems can serve as powerful components to protect against food degradation. [152] [153]

At higher triolein compositions, only the H_{II} phase is present with an intense (10) peak and greatly diminished consecutive peaks (Figure 6.8, compositions 6-9). It is possible the Fd3m phase is still present, however the additional triolein content has disordered the system to the point that the low intensity Bragg peaks are diminished. The final composition (Figure 6.8, composition 10), with the highest triolein content depicts a different phase which is explored further in this chapter.

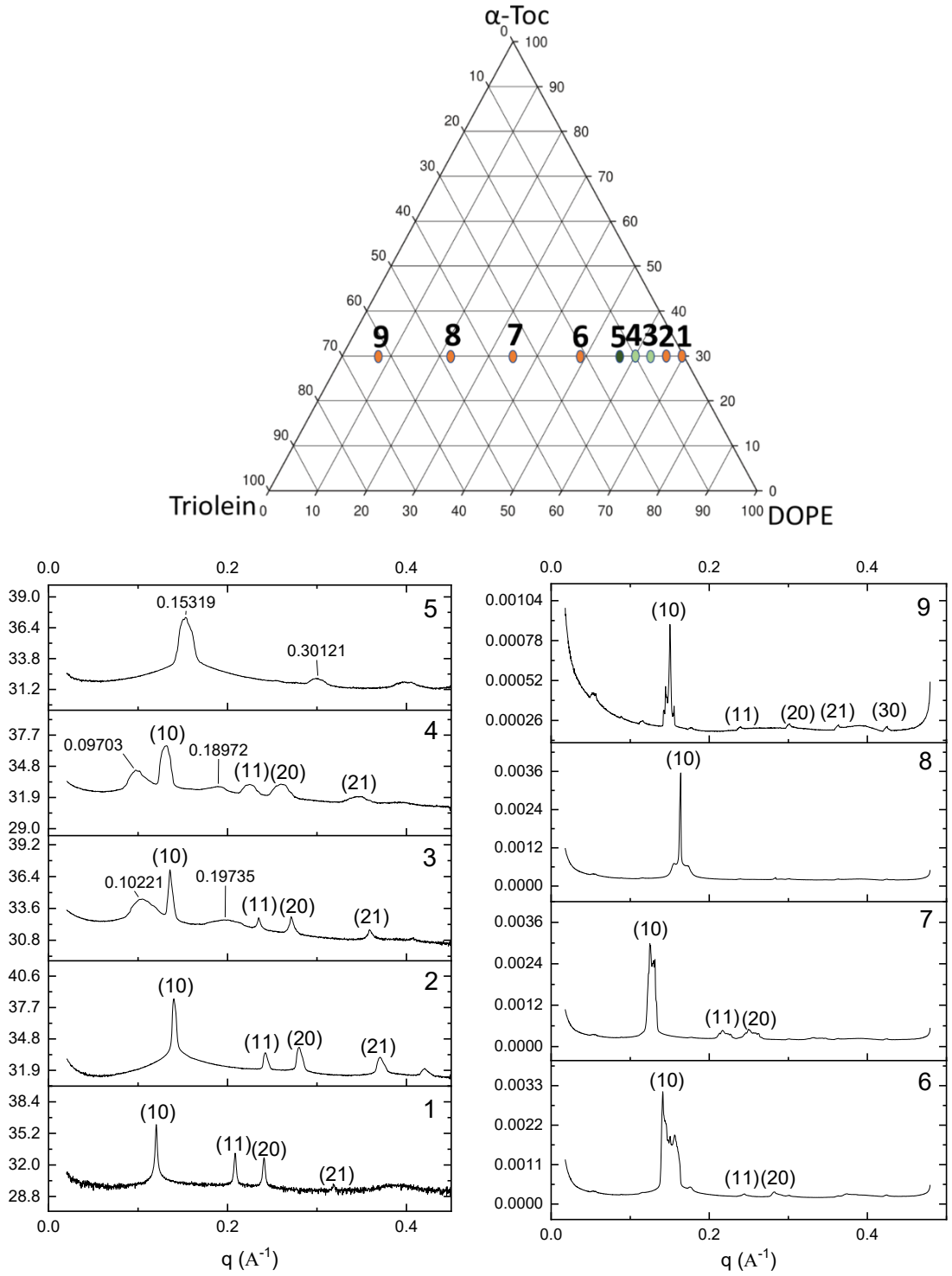


Figure 6. 11 SAXS profiles of compositions of α-Toc, DOPE and Triolein (excess water, at 25 °C) with compositions depicted in ternary phase diagram (top). The proportion of α-Toc is constant at 30 mol% with varying amounts of DOPE: Triolein, (1) 70:0, (2) 67.5:2.5, (3) 62.5:7.5, (4) 60:10, (5) 57.5: 12.5, (6) 49:21, (7) 35:35, (8) 22:48, (9) 8:62 (mol%). All studies are conducted in excess water. The H_{II} phase has been labelled with its corresponding Bragg peaks whereas some additional peaks are labelled with their q values. The orange represents the H_{II} phase. The H_{II} and lamellar phase co-existence has been represented in light green and the lamellar phase alone in dark green

The addition of 30 mol% α-Toc to DOPE alone in excess water (Figure 6.11, composition 1) results in a H_{II} phase with sharp well-defined Bragg peaks with a lattice parameter of 61.4 Å. The reported lattice

parameter of DOPE is 71.9 Å [154] meaning that α-Toc causes a decrease in lattice parameter of the H_{II} phase. Harper et al. have also found that α-Toc reduces the lattice parameter of DOPE but does not influence the average lipid length (calculated from electron density studies). From this, it was hypothesised that α-Toc relieves the compressive packing stress of the H_{II} phase via a novel mechanism. [155]

It is known that the H_{II} phase possesses an energetically costly packing energy caused by the extension of lipids in the long direction, and compression in the short direction (see Figure 6.12). The addition of hydrocarbons, such as dodecane or triglycerides, relieves this packing stress as the hydrocarbons fit deep into the tail regions of the lipid (Figure 6.12, middle). In the absence of hydrophobic components, the energetically costly extension of phospholipids in the long direction of the H_{II} phase, must be accompanied by an equally costly compression in the short direction (Figure 6.12, left). It is hypothesised that α-Toc replaces phospholipids and sits in the lipid-water interface of the H_{II} phase. As α-Toc's length is shorter than DOPE's, it relieves the compressive stress in the short direction (Figure 6.12, right). This results in an overall alleviation of the extensive stress and a reduction in the lattice parameter. [155]

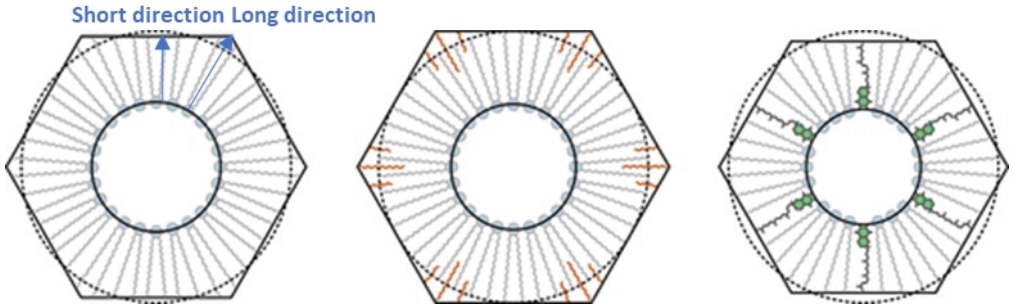


Figure 6. 12 Proposed models for DOPE alone, DOPE and dodecane (could depict any hydrocarbon) and DOPE and α-Toc taken from Harper et al.[155] Hydrocarbons alleviate H_{II} packing stress by filling the voids in the long direction. α-Toc however sits in along the short direction and reduces the unit cell size.

The addition of 2.5 mol% triolein to the α-Toc and DOPE system (Figure 6.11, composition 2) causes a decrease in lattice parameter from 61.4 Å to 53.0 Å. This is a drastic decrease and cannot be explained by the model proposed in by Harper et al. (Figure 6.12). Theoretically triolein would sit in the voids in the tail regions of the DOPE acyl chains to separate from the water due to its hydrophobicity. This

would also alleviate the stress associating to lipid chain stretching in the H_{II} phase. If anything, this would result in an increase in the unit cell size rather than a decrease. In fact, it has been shown that triolein does increase the lattice parameter of DOPE (Figure 6.6) in the absence of α-Toc. Therefore, the decrease in lattice parameter can be attributed to α-Toc further decreasing the unit cell of the H_{II} phase to better protect the triolein from oxidation. The mechanism by which α-Toc accomplishes this is unclear.

This same lattice parameter (53.0 Å) has been retained with the addition of 7.5 and 10 mol% triolein (Figure 6.11, compositions 3 and 4) with the peaks becoming broader with higher amounts of triolein. Additional broad Bragg peaks occur at these compositions, at a 1:2 ratio indicating that a lamellar phase is forming in co-existence with H_{II}. This lamellar phase is then the only phase remaining at 12.5 mol% triolein, however the diffuse Bragg peaks make it difficult to distinguish whether this is a true lamellar phase, or a separate H_{II} phase with the (11) peak diminished. Higher triolein compositions (Figure 6.11, composition 6-9) show SAXS profiles consistent with previous results; a H_{II} phase with largely diminished higher order peaks.

The addition of 50 mol% α-Toc yields to DOPE and triolein yields a phase which cannot be distinguished at low triolein compositions (Figure 6.13). The presence of 2-6 mol% triolein (Figure 6.13, compositions 1-3) yields a SAXS patterns with broad indistinguishable peaks which cannot be indexed. The addition of 8 mol% triolein (Figure 6.13, compositions 4), resolves the scattering pattern into identifiable Bragg peaks. Increasing the amount of triolein content has typically been broadening the peaks of the H_{II} phase of DOPE, in this case, the addition of triolein causes a sharpening of the Bragg peaks of this new phase.

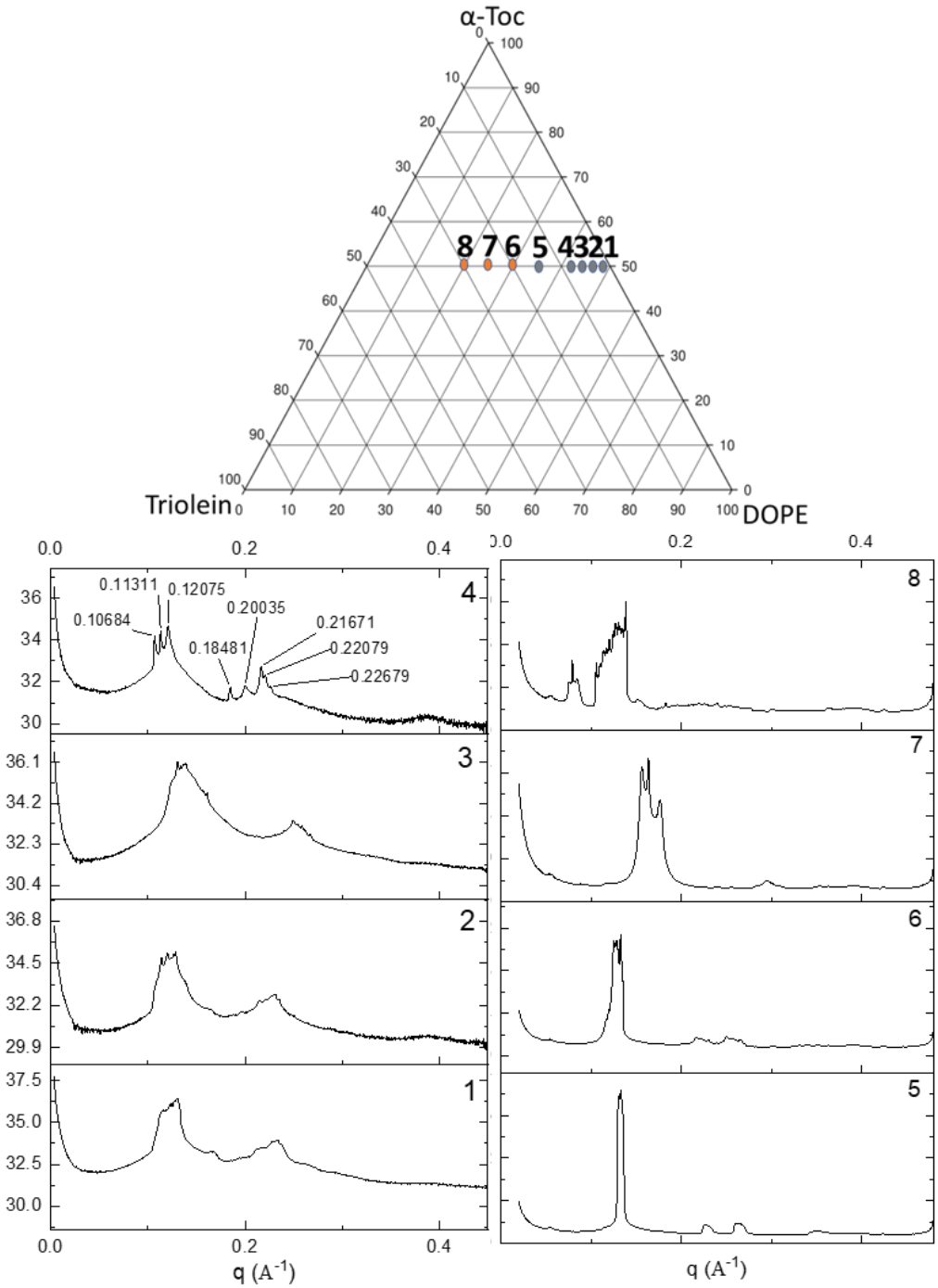


Figure 6. 13 SAXS profiles of compositions of α-Toc, DOPE and Triolein (excess water, at 25 °C) with compositions depicted in ternary phase diagram (top). The proportion of α-Toc is constant at 50 mol% with varying amounts of DOPE: Triolein, (1) 48:2, (2) 46:4, (3) 44:6, (4) 42:8, (5) 35:15, (6) 30:20, (7) 25:25, (8) 20:30 (mol%). All studies are conducted in excess water. Composition 4 is labelled with its corresponding Bragg peaks in q (Å^{-1}).). The orange represents the H_{II} phase, and the grey represents the hcp phase.

The Bragg peaks occurring at 50 mol% α-Toc with 8 mol% Triolein and 42 mol% DOPE (Figure 6.13, composition 4) can be assigned to the 3-D hexagonal close packed phase (hcp) (Table 6.1), where the d-spacing is related to lattice parameters, a and c and where R= $\frac{c}{a}$, by equation 6.1.

$$\frac{1}{d_{hkl}^2} = \frac{1}{a^2}\left(\frac{4}{3}(h^2 + k^2 + hk) + \frac{1}{R^2}l^2\right) \qquad \text{Equation 6.1}$$

The lattice parameters are a=67.9 and c = 110.8 Å (method detailed in Supplementary Information). The c/a ratio is 1.63 which is the same as the ratio found for a 3-D close packing of spheres (space group $P6_3/mmc$). The calculated d spacings fit well with the experimental d spacings (Supplementary Figure 6.3) and the experimental data can be indexed to show proof of the hcp phase (Figure 6.4). The data is also comparable to Shearman et al. (Table 6.1). Note that the (012) and (020) peaks are missing from experimental data. [19]

Table 6. 1 The indexing of the 3D-hcp phase with d_{cal} taken from Shearman et al. [156] The experimental d spacings fit well with the calculated d spacings

Index (hkl)	Calculated d-spacing (Å) (Shearman et al.)	Experimental q ($Å^{-1}$)	**Experimental d (Å)**	**Calculated d** (based on lattice parameters) **(Å)**
010	61.9	0.10684	**58.8**	**58.8**
002	58.3	0.11311	**55.5**	**55.3**
011	54.7	0.12075	**52.03**	**51.9**
012	42.4			**40.3**
110	35.8	0.18508	**33.9**	**34.0**
013	32.9	0.20035	**31.4**	**31.3**
020	31.0			**29.4**
112	30.5	0.21698	**29.0**	**27.7**
021	29.9	0.22079	**28.5**	**28.4**
004	29.1	0.22679	**27.7**	**27.7**

Shearman et al. have previously deduced that the indexing corresponds to a $P6_3/mmc$ phase, which is an inverse micellar phase with an *hcp* structure. The intensities of the observed reflections were similar to those corresponding to the 3-D hexagonal $P6_3/mmc$ phase obtained by Zeng et al.[157] This structure comprises of identical spherical micelles in an ABAB packing (Figure 6.14).

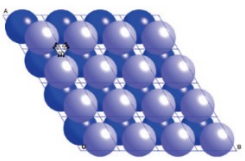


Figure 6. 14 The schematic structure of the 3-D hexagonal inverse micellar structure. The spheres represent the polar regions (water cores plus lipid headgroups) and the remaining volume is filled by hydrophobic regions (lipid chains and triolein). Taken from Shearman et al. [19]

Prior to the present work, only one case has been reported of the formation of lipidic inverse micelles with an *hcp* packing (space group $P6_3/mmc$). Shearman et al. reported it in hydrated diolein / DOPC mixtures with approx. 25 mol% cholesterol present. It was postulated that cholesterol migrated out of the densely packed micelles and functioned as a hydrophobic space filler to promote the formation of this phase. In the present case, it can be postulated that α-Toc promotes the formation of the Fd3m phase in DOPE by relieving the lipid tail frustration required for adopting a freely spherical shape at the most compact packing available. The addition of triolein can also function as a hydrophobic space filler which can fill the voids and to promote the hcp phase. This seems plausible as this hcp phase is also present at high triolein content with 10 mol% α-Toc present (Figure 6.8, composition 10). The energy difference between the Fd3m and *hcp* phases seems low so the precise factors favouring one over the other of these two phases is still elusive. [151] [108] [19]

At higher triolein contents (Figure 6.13, compositions 5-8), the hcp phase does not appear to be forming however the H_{II} phase seems prevalent. At the highest triolein content (composition 8), the three higher order Bragg peaks may correspond to the hcp phase, but it is difficult to distinguish from the SAXS pattern. Triolein could be disordering the long-range order of the *hcp* phase in the same way it disorders the H_{II} phase.

It is remarkable that the ternary system of DOPE: triolein: α-Toc is able to form an inverse micellar *hcp* phase, and this has implications including for food reactivity control, as well as for controlled release of drugs and nanoreactors.[19]

6.3 Chapter Summary

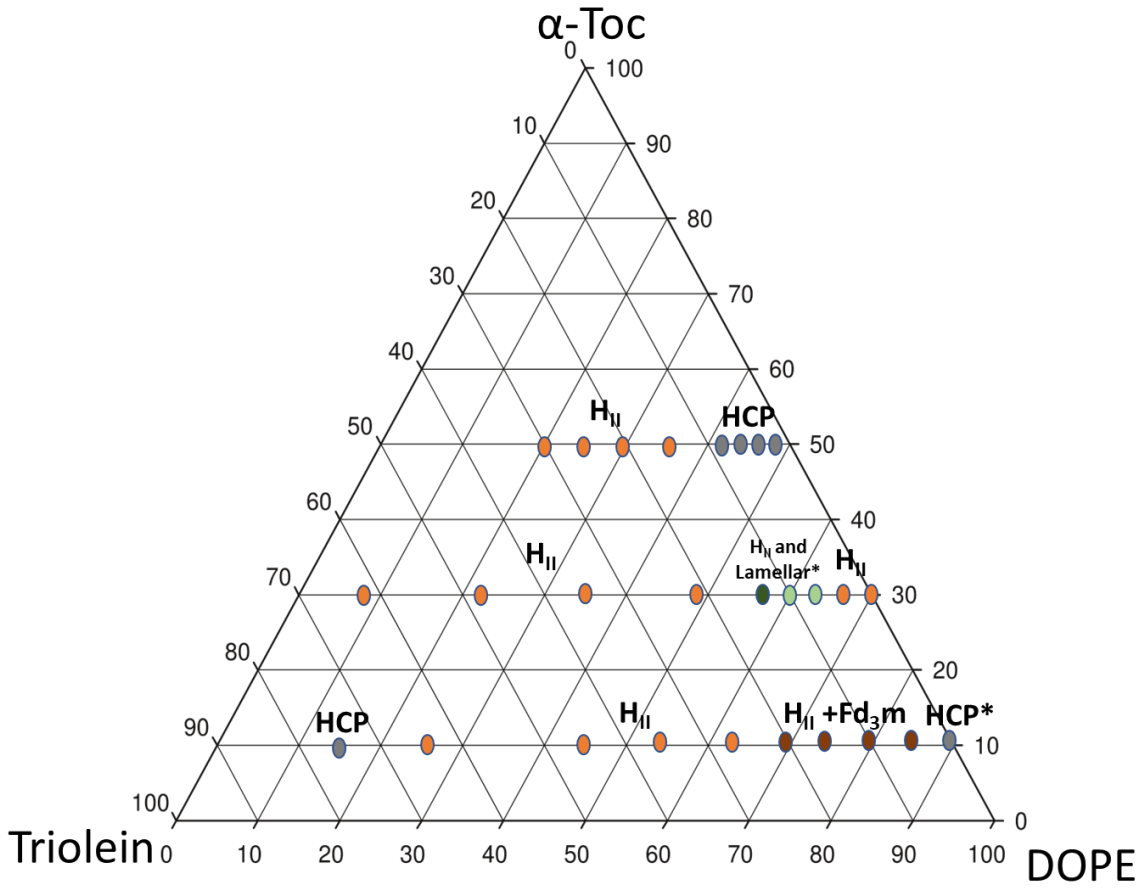


Figure 6. 15 The ternary phase diagram of DOPE: triolein: α-Toc (in excess water). The orange symbols represent the H_{II} phase, brown represents H_{II} and Fd3m phase co-existence, and grey represents the hcp phase. H_{II} and lamellar phase coexistence has been represented in light green, and the lamellar phase alone in dark green.
* These data points may not be indexed accurately: the lamellar phase could be an H_{II} phase with a peak missing, and the '*hcp*' phase at 10 mol% α-Toc does not have well defined Bragg peaks.

The ternary phase diagram of DOPE: triolein and α-Toc shows interesting features in regard to the phase behaviour (Figure 6.15). The very rare inverse micellar *hcp* phase (space group $P6_3/mmc$) can be seen at certain compositions. Other compositions form another rare H_{II} and Fd_3m phase co-existence. The presence and composition of these phases within the phase diagram is essential knowledge for harnessing the capabilities of cubic and hexagonal phases in food reactivity (or for pharmaceutical formulations).

Chapter 7: Analysis of Droplet Embedded Vesicles

7.1 Introduction

The previous chapter analysed the bulk phase of oil and lipid systems using SAXS measurements. This provides a good indication of lipid phase behaviour in oil and water environments; however, this does not depict all the interactions between oil and water. An important consideration is the formation of lens (Figure 7.1) which is the accumulation of triglyceride molecules between bilayer leaflets. Lenses are blister like domains within a bilayer, to which free oil molecules diffuse and create a 'nucleation site'. Depending on the amount of oil present and consequently the tension build-up within the membrane, the lens can bud off into a lipid droplet. Lipid droplets are inverted emulsions comprising of an oil core with an outer phospholipid monolayer. [158]

Lipid droplets are intracellular organelles which are produced in the endoplasmic reticulum and have a fundamental role in metabolism. Due to their unique architecture, lipid droplets require specialised mechanisms for formation, growth, and shrinkage, which allows the cells to regulate the emulsified oils when required for processes such as membrane synthesis. Consequently, the composition of phospholipids at the nucleation sites are crucial for lipid droplet growth and catabolism. To understand the formation of lipid droplets, it is important to understand the budding process. Phospholipid composition and surface tension are key parameters to induce budding, it has been found that a decrease in membrane tension, favours the formation of lipid droplets. [159] [160]

The process of lipid droplet biogenesis follows the process of i) nucleation: the initial accumulation of oil molecules within the bilayer leaflet ii) growth: due to ripening and fusion iii) budding: the

deformation of on the monolayer leading to an oil-filled protrusion. The initial nucleation site of a triglyceride site likely results from phase separation. For triglyceride molecules to globally reduce their interaction with the phospholipid bilayer they condense to form droplets. Nucleation can be favoured by i) membrane curvature ii) curvature inducing proteins or molecules iii) by proteins, lipids, or molecules with a favourable interaction with triglyceride (Figure 7.1). [161] [162]

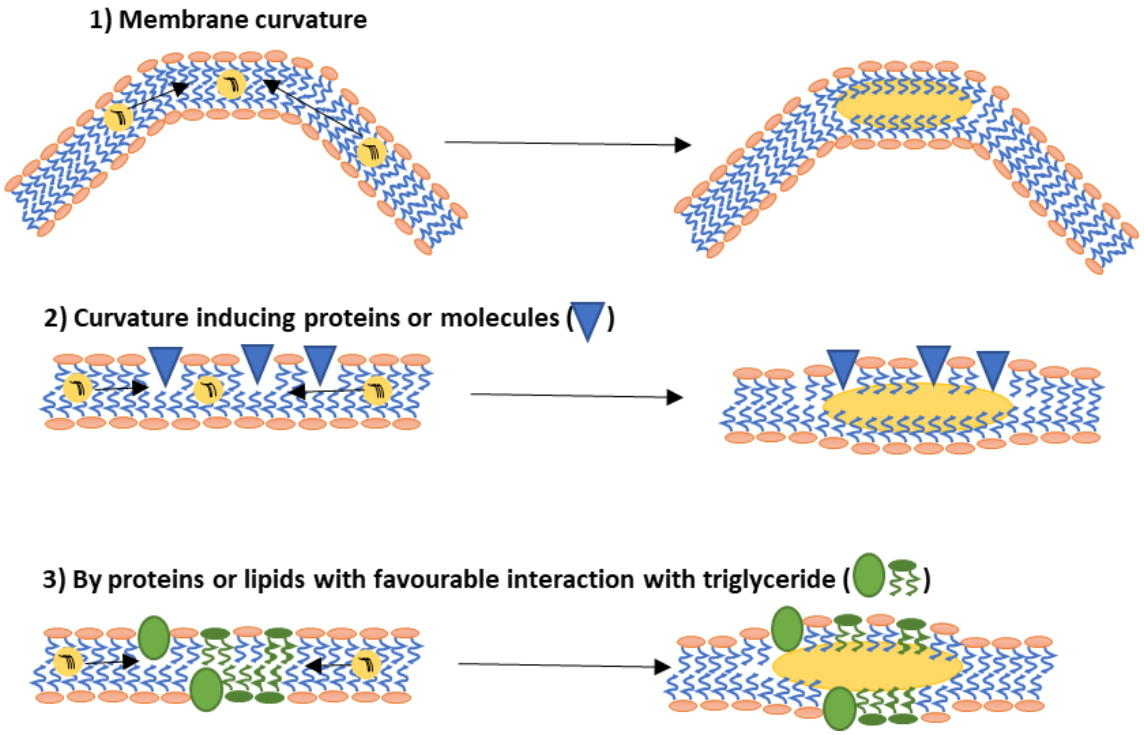


Figure 7. 1 Different mechanisms favouring the formation of the nucleation site. 1) local bilayer deformation caused by curvature results in the accumulation of triglyceride molecules. 2) the presence of curvature inducing proteins or molecules can cause defects within the bilayer to form a nucleation site 3) triglyceride aggregates in locations with favourable interactions with proteins or lipids. The yellow area represents triglyceride molecules (oil), the blue triangles represent curvature inducing proteins and the green molecules are indicative of molecules which interact favourably with oil. Adapted from Thiam et al.[163]

Depending on the rate of triglyceride diffusion (which is dependent on phospholipid composition), the nucleation sites can ripen into a droplet i) ripening: which involves diffusion of triglyceride from one nucleation site to another ii) fusion: which is the fusion of pre-droplets. Both fusion and ripening can generate supersized lipid droplets. In the endoplasmic reticulum (ER), proteins regulate these processes to stabilise or destabilise lipid droplet formation. [163]

The formation of a lipid droplet is caused by de-wetting of the oil phase from the substrate (Figure 7.2). In vivo, the substrate with be the endoplasmic reticulum membrane and the liquid would be the oil phase encapsulated in a monolayer of lipid. The likelihood of budding of the lipid droplet or dewetting is driven by the interfacial forces which originate from the surface tension of the phospholipid bilayer. In this chapter the surface tension has not been calculated, however the contact angle can be characterised which is determined by the surface tension. Small values of the contact angle i.e., close to 0° correspond to lens formation whereas larger values close to 180° are more indicative of budding. [163] [159]

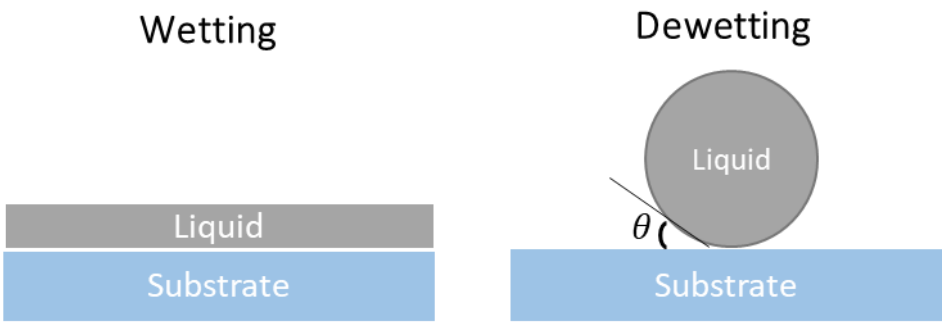


Figure 7. 2 Illustration of dewetting transitions. A liquid deposited on a surface can wet the surface or de-wet and form a droplet with a specific contact angle (Θ). The substrate is indicative of the lipid bilayer, and the liquid is the triglyceride encapsulated within a monolayer (when it forms a droplet). Adapted from Thiam et al.[159]

This chapter focusses on the formation of lipid droplets with DOPC/triolein and DOPC/DOPE/triolein and the likelihood of a lipid droplet budding from a phospholipid bilayer. This is synthetically replicated by forming giant unilamellar vesicles (GUVs) of the phospholipid and introducing triolein into the system (see chapter 3.2.3 for full details). It should be noted that DOPE is unable to form vesicles as it does not exist in a lamellar phase, therefore DOPC and mixtures of DOPC: DOPE have been used. The triolein is then encapsulated within the GUV vesicles to form a droplet embedded vesicle (DEV), of which the contact angle can be calculated. If the contact angle is close to 180° then there is a high chance of the lipid droplet budding of from the substrate. [161] [164]

Initially varying compositions of DOPC and DOPE are tested to measure the contact angle. Then α-Toc is introduced into the system to assess whether its membrane curvature inducing property, favours budding of lipid droplets.

7.2 Results and Discussion

7.2.1 Proof of formation of Droplet Embedded Vesicles (DEVs) and contact angle

Lipid droplets exist in the cytosol of an organism as oil droplets covered in a phospholipid monolayer i.e., oil in water droplets. In vitro, artificial lipid droplets can be mixed with GUVs to be incorporated in the intermonolayer space of the GUV membrane. This forms a DEV which serves as a mimic of the genesis of lipid droplets from the ER membrane (Figure 7.3). The formation of lipid droplets, and the likelihood of budding is dependent on the interactions between the oil and the lipid e.g., squalene forms a lens shaped DEV (non-budded with a small contact angle) with PC GUVs, whereas triolein forms droplet shaped DEVs (more budded with a contact angle closer to 180°). [160] [165]

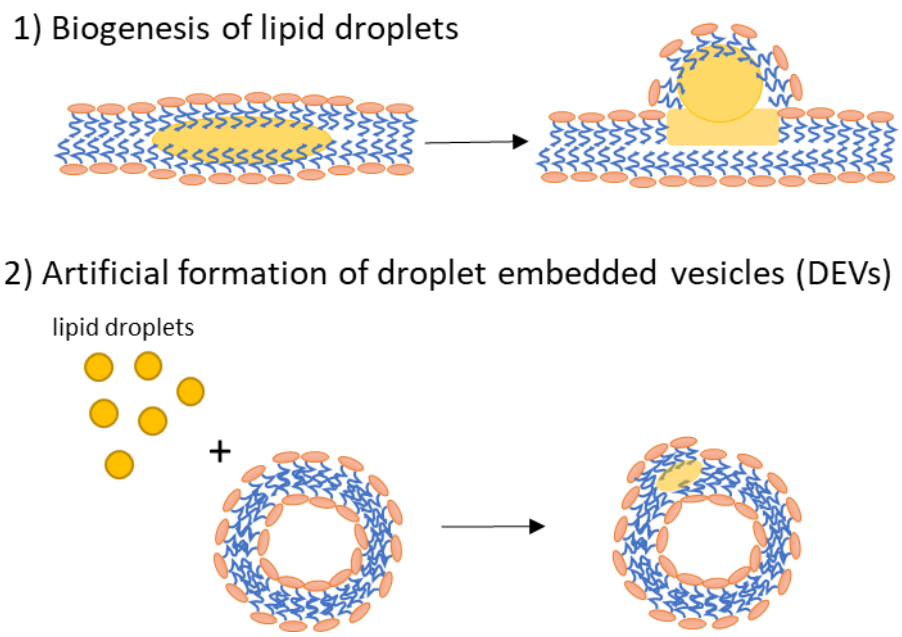


Figure 7. 3 1) In vivo representation of lipid droplet formation in ER membranes, accumulation of oil molecules eventually results in the lipid droplet budding from the membrane. 2) In vitro this process can be replicated in GUVs to form DEVs.

The formation of DEVs with purely DOPC GUVs and triolein was successfully synthesised. The brightfield images clearly depict the formation of lipid droplets within the GUV bilayer (Figure 7.4). The bigger lipid droplets are on the apex of the GUVs due to the buoyancy difference with water. To show the oil droplets are encapsulated within the bilayer the DOPC was stained with Rh-DHPE. The continuation of the fluorescent signal to the artificial lipid droplets provides evidence of the droplet being embedded in the bilayer (Figure SI 7.1). [160 166]

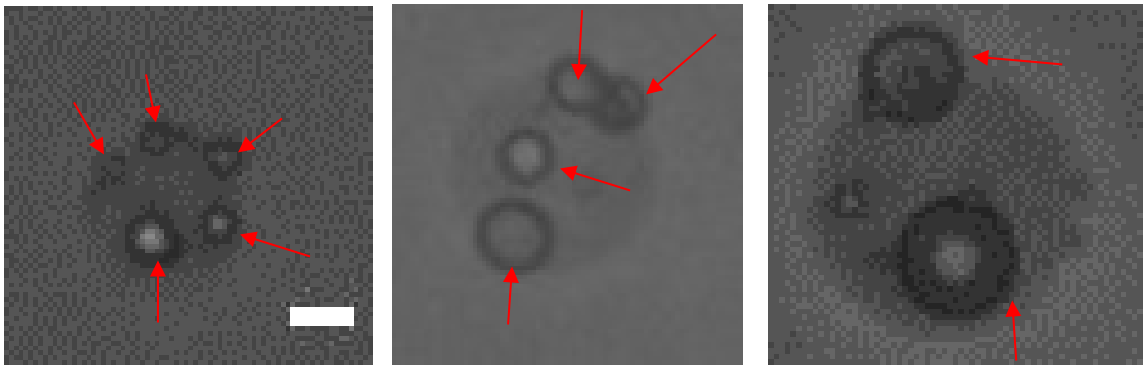


Figure 7. 4 Brightfield image showing proof of formation of DEVs with arrows pointing at the oil droplet. The GUVs are comprised solely of DOPC, and the oil encapsulated is triolein. Scale bar is 10 µm (applied to all three images)

The contact angle between the lipid droplets and GUVs can be calculated in cases in which the oil droplet is on the edge of the DEV (Figure SI 7.2). The contact angle for purely DOPC vesicles is 104 ±

8°, which suggests that a lens is forming, and the droplet is unlikely to bud off as the value is far less than 180°. As this area of study is still new, literature values to support this finding are not available. The contact angle of PC DEVs has been reported as 160 ± 5°, and equal mixtures of PC:DPPC as 155 ± 5°. [160] From this it can be concluded that different phospholipids have different budding aptitudes however DOPC and DPPC do favour the formation of droplets.

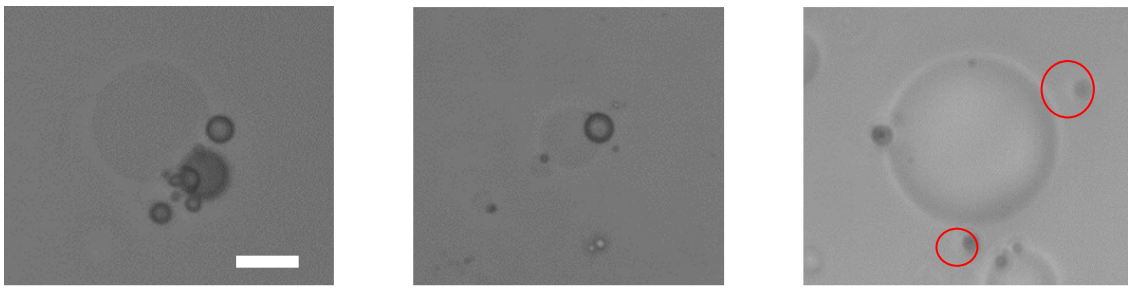


Figure 7. 5 Brightfield images of DEVs made from varying compositions of DOPC: DOPE with triolein. The red circles are likely indicative of egressed lipid droplets. Scale bar is 10 µm (applies to all three images)

The budding aptitudes of DPPC: DOPE mixtures have been analysed at varying compositions. The brightfield DEV images show the lipid droplet visually seems smaller with increasing compositions of DOPE (Figure 7.5). It can be hypothesised that the GUVs with greater compositions of DOPE have less favourable interactions with the triolein. The previous chapter showed that in the absence of water, triolein phase separates from DOPE, therefore they do not favourably interact. This could explain why the uptake of triolein in DOPE-rich bilayers is less and results in a smaller lipid droplet size, however more extensive work with DOPC and triolein interactions is required to derive the conclusion that triolein interacts more preferentially with DOPC than DOPE.

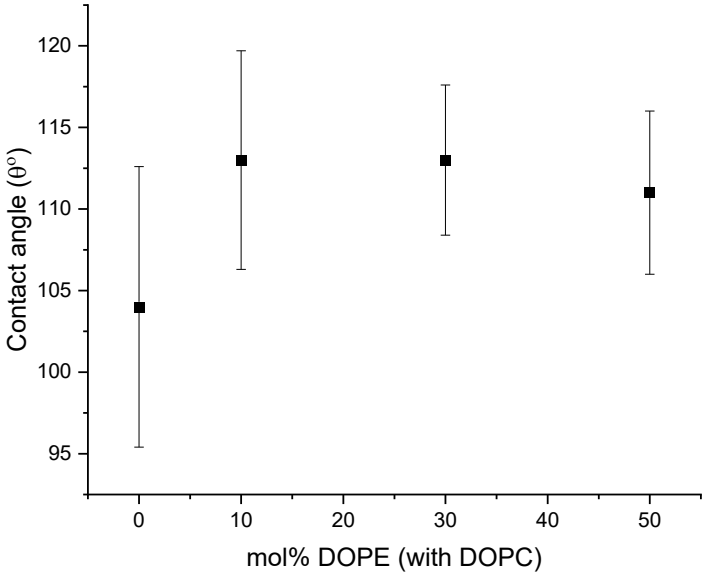


Figure 7. 6 Contact angle between the triolein lipid droplet and GUV within DEVs comprised of DOPC and DOPE mixtures. The error bar is indicative of the standard error of the mean calculated from three DEVs

The contact angle between the lipid droplet and GUV in DEVs (Figure 7.5) was calculated for n=3 DEVs for compositions of DOPC: DOPE GUVs. The addition of 10 mol% DOPE to DOPC DEVs with triolein, increases the contact angle to 113 ± 8° (Figure 7.6). After the initial increase in contact angle, increasing the DOPE composition further does not have much impact. The standard error within this data is quite large, this is likely because of the small sample size, as it was not possible to extract a contact angle for droplets which were not sitting on the edge of the GUV.

The increase in contact angle with the addition of DOPE suggests that the budding aptitude is greater, meaning the surface tension has increased. This could be because DOPE naturally forms a H_{II} phase in the bulk, as it is forced to adopt a lamellar conformation in the GUV, it exerts tension on to the bilayer. It could also be influencing the membrane curvature which promotes lipid droplet formation and budding (Figure 7.1). Zoni et al. have reported that PE promotes 'blister formation' of triglycerides and correspondingly triglyceride depletion from the membrane, using molecular dynamic simulations.[167] This is in agreement with the contact angle data reported (Figure 7.6), as compositions of DOPE and DOPC results in a higher contact angle than that of DOPC. However, the difference between the contact angles is not significant and falls within the same standard error range, suggesting that both

DOPC and DOPE have similar budding aptitudes. Visually however, a 50:50 mixture of DOPC: DOPE, not only forms smaller lipid droplets with triolein, but the egress of these droplets can also be seen (Figure 7.5, red circles). It is possible these are just oil droplets, and did not originate from the DEV, however their proximity to the DEV and size suggest they may be phospholipid coated oil vesicles.

The data presented suggests that DOPE promotes budding of lipid droplets more than DOPC, however the budding aptitude is not widely increased at a composition of up to 1:1 (DOPC: DOPE). Further experiments need to be designed to investigate the budding aptitude of pure DOPE which does not require the formation of GUVs.

7.2.2 The addition of α-Toc to DEVs

Previous chapters have explored the ability of α-Toc to induce curvature in membranes in the bulk phase. This chapter introduces α-Toc to DEVs comprised of DOPC, and DOPC: DOPE (1:1), with triolein. This determines whether α-Toc influences the budding aptitude of lipid droplets, and therefore the egress of triolein from a bilayer.

Initially only DEVs comprised of DOPC, α-Toc and triolein were analysed. The addition of 5 mol% α-Toc resulted in budding of lipid droplets from the DEV bilayer (Figure 7.7), meaning that α-Toc can sufficiently increase surface tension to promote a budding event. This is consistent with the results of the chapter 5 which shows that the addition of 5 mol% α-Toc causes an increase in membrane tension (Figure 5.10). The egress of triolein lipid droplets from DOPC/α-Toc vesicles could be attributed to α-Toc's ability to induce curvature. Although in bulk phase, SAXS data has shown that α-Toc only induces the H_{II} and other curved phases at compositions of 34 mol% and above with DOPC, it is likely that even at lower compositions

α-Toc is inducing local curvature. This property favours the formation of a nucleation site and the accumulation of triolein molecules (Figure 7.1). [168]

It should be noted that the budding of a lipid droplet is preceded by the deformation of the GUV, meaning a change in curvature in parts of the bilayer are necessary for the budding to occur. After the budding event, it is unclear whether the DEV has ruptured, or just disappeared from the plane of focus due to a change in density.

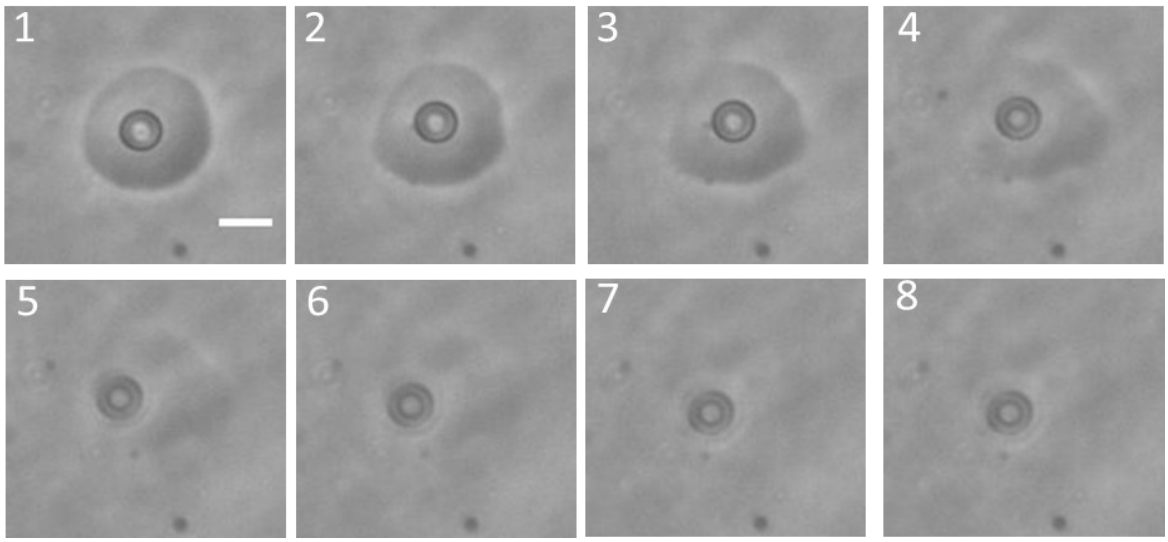


Figure 7. 7 Series of images depicting a budding event of a lipid droplet from a DEV. The DEV is comprised 5 mol% α-Toc with DOPC and triolein. Scale bar is 10 μm.

The addition of even smaller amounts of 1 mol% α-Toc to equimolar DOPC: DOPE DEVs also resulted in a budding event (Figure 7.8). This is like the amount of α-Toc naturally occurring in cell membranes therefore is an indication of its potent ability to induce local curvature. SAXS data of equimolar DOPC: DOPE with various compositions of α-Toc, depict a lamellar phase up until 10 mol% α-Toc in the bulk phase (Figure SI 7.3). It is at 15 mol% α-Toc in which the curved H_{II} and cubic phases are apparent. The fact that 1 mol% is sufficient to promote budding depicts α-Toc effective local function.

This is a rare example by which α-Toc's structural properties can directly be related to its antioxidant function. α-Toc's ability to induce curvature results in the packaging of oil (triolein) droplets coated in a phospholipid bilayer, this limits oxidation reactions between the oil-water interface. It is unclear whether α-Toc associates to the phospholipid bilayer in the DEV or the lipid droplet monolayer after the budding event.

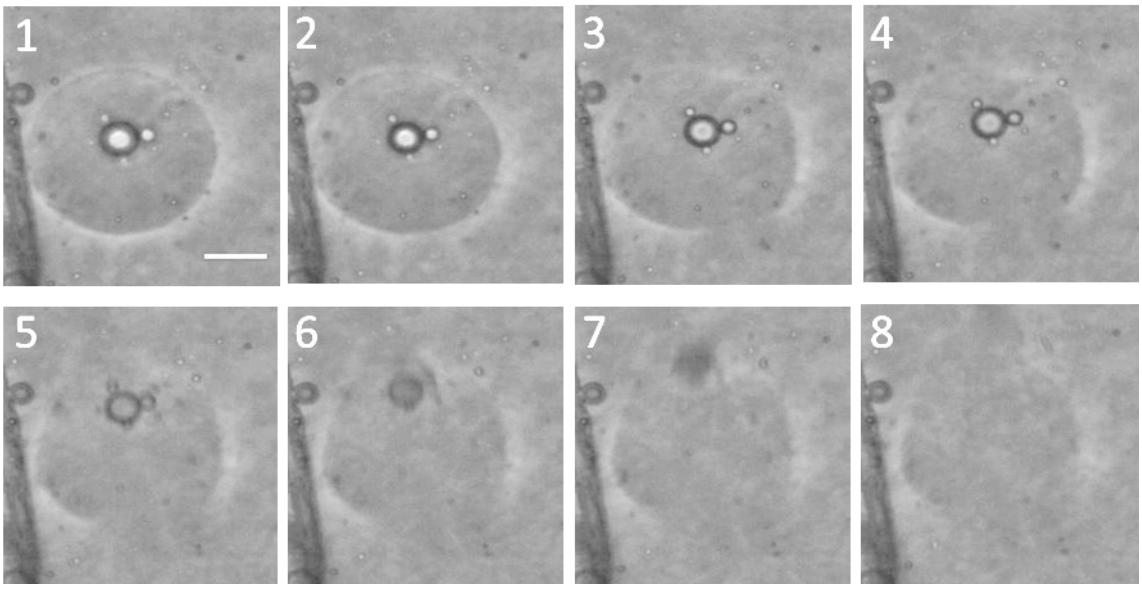


Figure 7. 8 Series of images depicting a budding event of a lipid droplet from a DEV. As the DEV egresses, the density of both the lipid droplet and the GUV changes meaning they are no longer in focus. The DEV is comprised 1 mol% α-Toc with DOPC: DOPE (1:1) and triolein. Scale bar is 10 μm.

7.3 Chapter Summary

This chapter explores the interactions of triolein with phospholipids using brightfield microscopy. Oil droplets can accumulate within a bilayer and depending on the oil to lipid interactions, form blisters large enough to become lipid droplets. These lipid droplets can bud off from the bilayer and function as vesicles of oil coated in a monolayer of lipid. The process of packaging oils and fatty acids into these vesicles is continuously performed by cell membranes and in particular by the endoplasmic reticulum.

158 169

To mimic this in vivo process, DEVs have been developed. This chapter shows the proof of formation of these DEVs made from DOPC and triolein and DOPE: DOPC and triolein. This shows that these lipids interact favourably to encapsulate triolein within the bilayer. The contact angle found between the lipid droplet and the DEV bilayers show that DOPE promoted budding more so than DOPC. The contact angle of DEVs with DOPE is slightly higher than DOPC, however it is not significant.

The addition of α-Toc to the system however is significant. The addition of 5 mol% α-Toc to DOPC and triolein DEVs results in budding events, as does the addition of 1 mol% α-Toc to DOPC: DOPE DEVs. This finding shows α-Toc potent ability to influence biological processes and the local environment in lipid bilayers. α-Toc's ability to promote budding agrees well with its antioxidant function as it packages minimises the oil-water interface.

Chapter 8: Future Outlook and Conclusions

8.1 Key findings and future outlook of Chapter 4

Chapter 4 analyses the influence of the addition of α-Toc to DPPC. DSC, ^{31}P ss-NMR and WAXS results show that α-Toc has a significant effect on the packing of the lipid acyl chains of DPPC. The DSC results show that the addition of α-Toc perturbs the L_β to L_α transition, broadens the endotherm, decreases the enthalpy change and lowers the overall transition temperature. This indicates that α-Toc is reducing the energy gap between the L_β and L_α phase, either by a fluidising impact or an ordering impact. Below the transition temperature of DPPC, the fluidising impact of α-Toc is also confirmed by line broadening of ^{31}P NMR and the deviation from 4.2 Å in WAXS. Above the transition temperature, the ordering impact of α-Toc on the L_α phase is elucidated by ^{2}H ss-NMR.

A remarkable finding is the phase separation of GUVs composed of DPPC, DOPC and α-Toc. The presence of phase separated domains in compositions of a saturated lipid, an unsaturated lipid and cholesterol have previously widely been reported. This is the first time that phase separation is seen to be induced by a molecule other than a sterol or a stanol. The fact that α-Toc can promote the lateral segregation of lipid domains is a novel finding. It is difficult to distinguish which two phases are separating from one another, it could be indicative of fluid-gel or fluid-fluid phase separation. In the case of cholesterol, extensive literature studies have shown that cholesterol promotes the formation of the L_o phase which separates from the L_α. In this case, the order profile calculated from ^{2}H ss-NMR suggests that α-Toc also has an ordering effect, however not to the extent of cholesterol. From these results it can be deduced that α-Toc is likely forming a L_o- type phase which separates from the L_α. [95]

Further studies in analysing phase separation in GUVs comprised of other lipids with α-Toc could be carried e.g., cholesterol also induces separation in GUVs comprised of sphingomyelin and DOPC. It would be useful to determine whether α-Toc can also induce phase separation in lipids other than DPPC and DOPC. Another unknown within this current data, is whether α -Toc is preferentially

interacting with DPPC or DOPC. In the case of cholesterol, it has been established that it associates to saturated lipids, however in the case of α -Toc it is unclear. Experiments using a fluorescent analogue of α-Toc may determine this. [170]

8.2 Key findings and future outlook of Chapter 5

Chapter 5 explores the interactions of α-Toc with DOPC using SAXS. A key novel finding is the co-existence of the Im3m phase with the H_{II} phase at certain compositions of α-Toc with DOPC. This depicts α-Toc's ability to induce curvature which is likely due α-Toc's bulky headgroup-type moiety destabilising the bilayer. It could also be hypothesised that α-Toc sits deeper within the bilayer in unsaturated lipids as the 'kink' within the double bonds can facilitate this position and therefore promotes curvature. [171]

The ternary phase diagram of DPPC, DOPC and α-Toc provides an insight into where curvature occurs. The H_{II} and Im3m phase is detected at certain compositions within the phase diagram, in which the DOPC content is higher than DPPC. It is also noteworthy that the Im3m phase is not ever found in isolation, rather it is always associated to H_{II}. This is unusual as a bicontinous cubic phase is normally considered an intermediate between lamellar and hexagonal phases.

The fact that α-Toc can induce curvature within a membrane suggests that it can produce local stress within biological membranes. This could affect lipid-protein interactions, which may amplify its function as an antioxidant. Its phase behaviour is also important ex vivo for skin care and food formulations.

Future work involved analysing the impact of lower compositions of α-Toc with DOPC. The addition of up to 30 mol% α-Toc to DOPC still forms the L_α phase as curvature is induced at higher compositions. However, this L_α changes as the α-Toc content increases, the SAXS peaks become broader and the d-spacing is altered. The impact of α-Toc to the L_α phase of DOPC is explored somewhat by fluctuation

analysis, however other techniques such as micropipette aspiration may confirm the bending rigidity and membrane tension values.

8.3 Key findings and future outlook of Chapter 6 and 7

Chapter 6 explores the ternary mixtures of triolein, DOPE and α-Toc as this system is indicative of components within food products. Chapter 6 uses SAXS to compose a ternary phase diagram (in excess water) with these three components. At certain compositions the phase co-existence of H_{II} and Fd3m can be detected which is not common. An ever more uncommon phase is the inverse micellar hcp phase (space group P63/mmc) which is present at certain other compositions. This phase has previously only been reported once. It is interesting that these closely packed phases only occur when triolein is added to the system. Binary DOPE and α-Toc (in excess water) only forms the H_{II} phase. Therefore, this is a potent indication of α-Toc's ability to protect triolein by separating it from the water (and encapsulating within the cores of the hcp or Fd3m phase) and therefore function as an effective antioxidant. Further studies such as oxidation experiments are required to confirm this.

Chapter 7 explores the molecular interactions between DOPE (and DOPC) and triolein by forming droplet embedded vesicles (DEVs). Previous literature studies have shown that oil is encapsulated within lipid bilayers (in water environments) to form a lens like structure. When the accumulation of oil molecules within a bilayer reaches a certain limit, the lens like structure expands and buds off as a droplet. This is a lipid droplet whereby a monolayer of lipid encapsulates an oil core. This process is indicative of biological processes e.g., the packaging of lipids into vesicles from the Golgi membrane.[163] [160] [172]

In this work, the proof of triolein encapsulation within DOPE: DOPC bilayers has been shown by forming and imaging DEVs. This is indicative of the favourable interactions between DOPE and DOPC with triolein. The contact angle between the triolein droplet and the vesicle bilayer was also calculated as a contact angle close to 180° is indicative of lipid droplet budding. It was found that varying the DOPE:DOPC ratio did not have an impact on the contact angle between the oil droplet and the vesicle.

The addition of α-Toc to the system however did have a large impact. DEVs comprised of DOPC (and DOPE) with α-Toc, not only favoured the formation of oil droplets within the bilayer, but they also promoted budding. Brightfield images show budding events occurring when a lipid droplet containing triolein egresses from the vesicle. This is indicative of α-Toc's ability to induce curvature as this increases the tension within the membrane to promote budding. Future studies within this area are vast. The analysis of the membrane tension within DEVs could be analysed using micropipette aspiration or droplet interface bilayers could be analysed to calculate the 'budding angle'. [159] [168]

8.4 Implications and limitations of work

α-Toc's potent antioxidant activity has been found to be effective in the prevention and reversal of many diseases such as cardiovascular, cancer and Alzheimer's. It is also harnessed in skincare products for anti-aging purposes and has the potential to increase the shelf-life of oxidation prone food products. However, in the many oxidation studies conducted, in the myriad of disease areas, the utility of α-Toc has been inconsistent. This is because α-Toc's antioxidant activity is dependent on factors such as chemical environment and dosing. The aims of this work were to analyse α-Toc in different environments to better understand its interactions with lipids. This in turn, allows us to harness its antioxidant potential and builds on knowledge of its structural function.

α-Toc's ability to induce phase separation in mixed saturation lipids is indicative of its capability to structurally alter the lateral segmentation of lipids in a bilayer. This is powerful as many cell signalling processes in vivo, are dependent on specific lipid compositions within the cell membrane. This finding also indicates similarities between the structural function of α-Toc and cholesterol, as cholesterol also induces lateral phase separation. From a commercial perspective, replacing cholesterol with α-Toc (vitamin E) in food systems would be deemed as a healthier alternative.

This body of work also highlights α-Toc potent ability to induce curvature. The induction of the cubic phases: Im3m and hcp, and the hexagonal phase indicates how α-Toc may be achieving its antioxidant function. Not only is α-Toc able more readily available to intercept free radicals, when in a curved

structure, it also can physically separate the hydrophilic and hydrophobic boundary. For example, the hcp phase contains voids for the hydrophobic (triolein) to locate into. This physically separates the triolein from the water, minimising the occurrence of oxidation reactions.

α-Toc's curvature inducing ability also has many wider applications. In vivo, the induction of local curvature has an impact on various cell processes such as cell signalling and exocytosis. Ex vivo, cubic, and hexagonal phases offer the potential of novel drug and nutrient delivery routes. This increases the utility of α-Toc in drug formulations, as not only does it have an antioxidant function but also a structural function.

One of the limitations of this body of work is that α-Toc's structural function is not directly correlated to its antioxidant. It would be beneficial to understand if and how a specific phase impacts oxidation reactions e.g., does the presence of the Im3m phase with the hexagonal at specific α-Toc and DOPC compositions enhance or decrease the antioxidant activity. This could be accomplished by conducting oxidation studies.

Another limitation of this work is that many of the experiments, although provide a good understanding of the phase behaviour, have only been conducted once. In the case of the X-ray diffraction data, it is likely that some samples are not as well homogenised or are dehydrated. Future studies would look at repeating some of these experiments to ensure that results are consistent.

Chapter 9: Bibliography

1 S. Rizvi, S. T. Raza, F. Ahmed, A. Ahmad, S. Abbas and F. Mahdi, *Sultan Qaboos Univ. Med. J.*, 2014, **14**, e157-65.

2 J. M. Zingg, *IUBMB Life*, 2019, **71**, 456–478.

3 X. Wang and P. J. Quinn, *Prog. Lipid Res.*, 1999, **38**, 309–336.

4 S. Lemaire-Ewing, C. Desrumaux, D. Néel and L. Lagrost, *Mol. Nutr. Food Res.*, 2010, **54**, 631–640.

5 P. J. Quinn, *Biochem.*, 2004, **69**, 58–66.

6 V. E. KAGAN, *Ann. N. Y. Acad. Sci.*, 1989, **570**, 121–135.

7 V. A. Tyurin, V. E. Kagan and E. A. Serbinova, *Biull. Eksp. Biol. Med.*, 1986, **102**, 689–692.

8 S. J. Singer and G. L. Nicolson, *Science (80-.).*, 1972, **175**, 720–731.

9 F. M. Goñi, *Biochim. Biophys. Acta - Biomembr.*, 2014, **1838**, 1467–1476.

10 D. L. Daleke, *J. Lipid Res.*, 2003, **44**, 233–242.

11 A. A. Spector and M. A. Yorek, *J. Lipid Res.*, 1985, **26**, 1015–35.

12 K. Shaw, PhD Thesis, Imperial College, London, 2009.

13 *Introduction to Soft Matter-Revised Edition*, 2007.

14 O. Ces and X. Mulet, *Signal Transduct.*, 2006, **6**, 112–132.

15 Y. Elani, PhD Thesis, Imperial College London, 2014.

16 A. I. I. Tyler, H. M. G. Barriga, E. S. Parsons, N. L. C. McCarthy, O. Ces, R. V. Law, J. M. Seddon and N. J. Brooks, *Soft Matter*, 2015, **11**, 3279–3286.

17 J. M. M. Seddon and R. H. H. Templer, in *Handbook of Biological Physics*, North-Holland, 1995, vol. 1, pp. 97–160.

18 J. M. Seddon, E. A. Bartle and J. Mingins, *J. Phys. Condens. Matter*, 1990, **2**, SA285–SA290.

19 G. C. Shearman, A. I. I. Tyler, N. J. Brooks, R. H. Templer, O. Ces, R. V. Law and J. M. Seddon, *J. Am. Chem. Soc.*, 2009, **131**, 1678–1679.

20 J. M. Seddon, *Biochim. Biophys. Acta - Rev. Biomembr.*, 1990, **1031**, 1–69.

21 C. Conn and J. Seddon, in *Liposomes, Lipid Bilayers and Model Membranes*, CRC Press, 2014, pp. 31–48.

22 D. Marsh, *Biochim. Biophys. Acta - Rev. Biomembr.*, 1996, **1286**, 183–223.

23 W. Helfrich, *Zeitschrift fur Naturforsch. - Sect. C J. Biosci.*, 1973, **28**, 693–703.

24 S. Purushothaman, PhD Thesis, Imperial College, London, 2014.

25 S. Purushothaman, P. Cicuta, O. Ces and N. J. Brooks, *J. Phys. Chem. B*, 2015, **119**, 9805–9810.

26 J. R. Silvius, *Biochim. Biophys. Acta - Biomembr.*, 2003, 1610, 174–183.

27 M. B. Sankaram and T. E. Thompson, *Biochemistry*, 1990, **29**, 10676–10684.

28 D. A. Brown and E. London, *J. Membr. Biol.*, 1998, **164**, 103–114.

29 T. Koga and J. Terao, *J. Agric. Food Chem*, 1995, **43**, 1450–1454.

30 J. Atkinson, R. F. Epand and R. M. Epand, *Free Radic. Biol. Med.*, 2008, **44**, 739–764.

31 E. Serbinova, V. Kagan, D. Han and L. Packer, *Free Radic. Biol. Med.*, 1991, **10**, 263–75.

32 B. Chen, A. Han, M. Laguerre, D. J. McClements and E. A. Decker, *Food Funct.*, 2011, **2**, 302–309.

33 B. Chen, A. Han, D. J. McClements and E. A. Decker, *J. Agric. Food Chem.*, 2010, **58**, 11993–

11999.

34 X. Wang and P. J. Quinn, *Eur. J. Biochem.*, 2000, **267**, 6362–6368.

35 X. Wang and P. J. Quinn, *Biochim. Biophys. Acta - Biomembr.*, 2000, **1509**, 361–372.

36 J. Salgado, J. Villalain and J. C. Gomezfernandez, *Arch. Biochem. Biophys.*, 1993, **306**, 368–376.

37 N. Barouh, C. Bourlieu-Lacanal, M. C. Figueroa-Espinoza, E. Durand and P. Villeneuve, *Compr. Rev. Food Sci. Food Saf.*, 2022, **21**, 642–688.

38 D. Marquardt, J. A. Williams, N. Kučerka, J. Atkinson, S. R. Wassall, J. Katsaras and T. A. Harroun, *J. Am. Chem. Soc.*, 2013, **135**, 7523–7533.

39 H. Saito and K. Ishihara, *J. Am. Oil Chem. Soc.*, 1997, **74**, 1531–1536.

40 A. T. Diplock and J. A. Lucy, *FEBS Lett.*, 1973, 29, 205–210.

41 S. Urano, M. Iida, I. Otani and M. Matsuo, *Biochem. Biophys. Res. Commun.*, 1987, **146**, 1413–1418.

42 J. Atkinson, T. Harroun, S. R. Wassall, W. Stillwell and J. Katsaras, *Mol. Nutr. Food Res.*, 2010, **54**, 641–651.

43 M. G. Traber and J. Atkinson, *Free Radic. Biol. Med.*, 2007, **43**, 4–15.

44 M. Afri, B. Ehrenberg, Y. Talmon, J. Schmidt, Y. Cohen and A. A. Frimer, *Chem. Phys. Lipids*, 2004, **131**, 107–121.

45 A. K. Mukherjee, S. K. Ghosal and C. R. Maity, *Cell. Mol. Life Sci.*, 1997, **53**, 152–155.

46 W. H. Zachariasen, *Acta Crystallogr.*, 1967, **23**, 558–564.

47 M. M. Woolfson, *An Introduction to X-ray Crystallography*, Cambridge University Press, 1997.

48 L. Katz, *J. Chem. Educ.*, 1964, **41**, 292.

49 A. I. I. Tyler, R. V. Law and J. M. Seddon, in *Methods in Membrane Lipids: Second Edition*, Humana Press, New York, NY, 2015, pp. 199–225.

50 J. Bolze, V. Kogan, D. Beckers and M. Fransen, *Rev. Sci. Instrum.*, 2018, **89**, 085115.

51 N. Yagi, *Compr. Biomed. Phys.*, 2014, **8**, 17–33.

52 W. Clegg, *J. Chem. Soc. Dalt. Trans.*, 2000, **1**, 3223–3232.

53 F. Holger Försterling, *Spin dynamics: Basics of Nuclear Magnetic Resonance, Second Edition*, 2009, vol. 37.

54 P. D. Lickiss, *J. Organomet. Chem.*, 1987, **329**, C34.

55 J. Seelig, *Q. Rev. Biophys.*, 1977, **10**, 353–418.

56 M. Weingarth and M. Baldus, 2014, pp. 1–17.

57 A. E. McDermott and T. Polenova, *Solid-state NMR studies of biopolymers*, John Wiley & Sons, 2010.

58 M. J. Duer, *Solid-state NMR spectroscopy : principles and applications*, Blackwell Science, 2002.

59 N. Pace, Kings College London, PhD thesis, 2016.

60 M. Mehring, R. G. Griffin and J. S. Waugh, *J. Chem. Phys.*, 1971, **55**, 746–755.

61 H. W. Spiess, *Dyn. NMR Spectrosc.*, 1978, 55–214.

62 A. Iuga, C. Ader, C. Gröger and E. Brunner, *Annu. Reports NMR Spectrosc.*, 2006, **60**, 145–189.

63 T. H. Semmence, Imperial College London, PhD thesis, 2018.

64 M.-A. Sani, D. K. Weber, F. Delaglio, F. Separovic and J. D. Gehman, *PeerJ*, 2013, **1**, e30.

65 P. Gill, T. T. Moghadam and B. Ranjbar, *J. Biomol. Tech.*, 2010, **21**, 167.

66 A. Chorlay, A. Santinho and A. R. Thiam, *STAR Protoc.*, 2020, 100116.

67 Y. Z. Yoon, J. P. Hale, P. G. Petrov and P. Cicuta, *J. Phys. Condens. Matter*, 2010, **22**, 062101.

68 J. L. Thewalt, S. R. Wassall, H. Gorrissen and R. J. Cushley, *Biochim. Biophys. Acta - Biomembr.*, 1985, **817**, 355–365.

69 X. Wang, K. Semmler, W. Richter and P. J. Quinn, *Arch. Biochem. Biophys.*, 2000, **377**, 304–314.

70 X. Wang and P. J. Quinn, *Prog. Lipid Res.*, 1999, **38**, 309–36.

71 M. A. Kamal and V. A. Raghunathan, *Biochim. Biophys. Acta - Biomembr.*, 2012, **1818**, 2486–2493.

72 S. Karmakar and V. A. Raghunathan, , DOI:10.1103/PhysRevLett.91.098102.

73 S. Karmakar, V. A. Raghunathan and S. Mayor, *J. Phys. Condens. Matter*, 2005, **17**, S1177–S1182.

74 D. Marquardt, N. Kučerka, S. R. Wassall, T. A. Harroun and J. Katsaras, *Chem. Phys. Lipids*, 2016, **199**, 17–25.

75 E. J. MCMURCHIE, G. H. Mcintosh, D. P. Liposomes, E. J. MCMURCHIE and G. H. Mcintosh, *J. Nutr. Sci. Vitaminol. (Tokyo).*, 1986, **32**, 551–558.

76 J. A. Clarke, J. M. Seddon and R. V. Law, *Soft Matter*, 2009, **5**, 369–378.

77 S. O. Yesylevskyy, A. P. Demchenko, S. Kraszewski and C. Ramseyer, *Sci. World J.*, 2013, **2013**, 1–10.

78 S. L. Veatch and S. L. Keller, *Biophys. J.*, 2003, **85**, 3074–83.

79 E. A. Smith, W. Wang and P. K. Dea, *Chem. Phys. Lipids*, 2012, **165**, 151–159.

80 D. Malia, MRes Dissertation, Imperial College London, 2018.

81 G. Neunert, J. Tomaszewska-Gras, P. Siejak, Z. Pietralik, M. Kozak and K. Polewski, *Chem. Phys. Lipids*, 2018, **216**, 104–113.

82 M. R. Vist and J. H. Davis, *Biochemistry*, 1990, **29**, 451–464.

83 T. P. W. McMullen, R. N. A. H. Lewis and R. N. McElhaney, *Biochemistry*, 1993, **32**, 516–522.

84 M. S. Paz, F. J. Aranda and J. C. Gmez-fern, 1996, **1279**, 251–258.

85 H. Yao, S. Matuoka, B. Tenchov and I. Hatta, *Biophys. J.*, 1991, **59**, 252–255.

86 K. P. Shaw, N. J. Brooks, J. A. Clarke, O. Ces, J. M. Seddon and R. V. Law, *Soft Matter*, 2012, **8**, 1070–1078.

87 L. Chen, Z. Yu and P. J. Quinn, *Biochim. Biophys. Acta - Biomembr.*, 2007, **1768**, 2873–2881.

88 F. Picard, M. J. Paquet, J. Levesque, A. Belanger and M. Auger, *Biophys. J.*, 1999, **77**, 888–902.

89 K. Arnold, A. Lösche and K. Gawrisch, *Biochim. Biophys. Acta - Biomembr.*, 1981, **645**, 143–148.

90 X. Peng and J. Jonas, *Biochemistry*, 1992, **31**, 6383–6390.

91 N. Kahya, D. Scherfeld, K. Bacia and P. Schwille, *J. Struct. Biol.*, 2004, 147, 77–89.

92 K. Suga and H. Umakoshi, *Langmuir*, 2013, **29**, 4830–4838.

93 M. DiPasquale, M. H. L. Nguyen, B. W. Rickeard, N. Cesca, C. Tannous, S. R. Castillo, J. Katsaras, E. G. Kelley, F. A. Heberle and D. Marquardt, *Biochim. Biophys. Acta - Biomembr.*, 2020, **1862**, 183189.

94 M. Hao, S. Mukherjee and F. R. Maxfield, *Proc. Natl. Acad. Sci. U. S. A.*, 2001, **98**, 13072–7.

95 S. L. Veatch, I. V Polozov, K. Gawrisch and S. L. Keller, *Liquid Domains in Vesicles Investigated by NMR and Fluorescence Microscopy*, .

96 M. R. Morrow and J. L. Thewalt, in *Solid-State NMR*, IOP Publishing, 2020, pp. 2-1-2–20.

97 H. McConnell and A. Radhakrishnan, *Proc. Natl. Acad. Sci.*, 2006, **103**, 1184–1189.

98 S. R. Wassall, J. L. Thewalt, L. Wong, H. Gorrissen and R. J. Cushley, *Biochemistry*, 1986, **25**, 319–326.

99 P. L. Yeagle, *Membr. Cells*, 2016, 155–188.

100 A. I. I. Tyler, J. A. Clarke, J. M. Seddon and R. V. Law, in *Methods in Membrane Lipids: Second Edition*, Springer New York, 2014, pp. 227–253.

101 J. A. Clarke, A. J. Heron, J. M. Seddon and R. V Law, *Biophys. J.*, **90**, 2383–2393.

102 S. Leekumjorn and A. K. Sum, *Biophys. J.*, **90**, 3951–3965.

103 M. Shaghaghi, A. Keyvanloo, Z. Huang, F. C. Szoka and J. L. Thewalt, *Langmuir*, 2017, **33**, 14405–14413.

104 T. R. Molugu, X. Xu, A. Leftin, S. Lope-Piedrafita, G. V. Martinez, H. I. Petrache and M. F. Brown, in *Modern Magnetic Resonance*, Springer International Publishing, Cham, 2018, pp. 581–603.

105 T. P. W. McMullen, R. N. A. H. Lewis and R. N. McElhaney, *Curr. Opin. Colloid Interface Sci.*, 2004, **8**, 459–468.

106 I. Martiel, L. Sagalowicz and R. Mezzenga, *Adv. Colloid Interface Sci.*, 2014, **209**, 127–143.

107 B. G. Tenchov, R. C. MacDonald and D. P. Siegel, *Biophys. J.*, 2006, **91**, 2508–2516.

108 I. Martiel, L. Sagalowicz and R. Mezzenga, *Langmuir*, 2013, **29**, 15805–15812.

109 J. Barauskas, C. Cervin, F. Tiberg and M. Johnsson, *Phys. Chem. Chem. Phys.*, 2008, **10**, 6483–6485.

110 X. Wang and P. J. Quinn, *Eur. J. Biochem.*, 1999, **264**, 1–8.

111 A. Ortiz, F. J. Aranda and J. C. Gómez-Fernández, *Biochim. Biophys. Acta - Biomembr.*, 1987,

898, 214–222.

112 X. Wang and P. J. Quinn, *Biophys. Chem.*, 1999, **80**, 93–101.

113 S. J. Marrink and A. E. Mark, *Biophys. J.*, 2004, **87**, 3894–3900.

114 D. Marsh, *Biophys. J.*, , DOI:10.1016/S0006-3495(96)79790-4.

115 Y. Kozlovsky, A. Efrat, D. P. Siegel and M. M. Kozlov, *Biophys. J.*, 2004, **87**, 2508–2521.

116 X. Wang and P. J. Quinn, *Biochimie*, 2006, **88**, 1883–8.

117 M. Alwarawrah, J. Dai and J. Huang, *J. Phys. Chem. B*, 2010, **114**, 7516.

118 T. A. Daly, M. Wang and S. L. Regen, *Langmuir*, 2011, **27**, 2159–2161.

119 J. Dai, M. Alwarawrah and J. Huang, *J. Phys. Chem. B*, 2009, **114**, 840–848.

120 Y. Ma, S. K. Ghosh, D. A. Dilena, S. Bera, L. B. Lurio, A. N. Parikh and S. K. Sinha, *Biophys. J.*, 2016, **110**, 1355–1366.

121 M. Aghaaminiha, A. M. Farnoud and S. Sharma, *Soft Matter*, 2021, **17**, 2742–2752.

122 W.-C. Hung, M.-T. Lee, F.-Y. Chen and H. W. Huang, , DOI:10.1529/biophysj.106.099234.

123 Y. J. Kwon, S. Jo, H. S. Na, S. H. Kim, M. J. Kim and J. H. Lee, *Food Sci. Biotechnol.*, 2020, **29**, 479–486.

124 T. T. Mills, J. Huang, G. W. Feigenson and J. F. Nagle, *Gen. Physiol. Biophys.*, 2009, **28**, 126.

125 H. Zhan and T. Lazaridis, *Biophys. J.*, 2013, **104**, 643.

126 I. Szleifer, D. Kramer, A. Ben-Shaul, W. M. Gelbart and S. A. Safran, *J. Chem. Phys.*, 1990, **92**, 6800–6817.

127 M. Doktorova, D. Harries and G. Khelashvili, *Phys. Chem. Chem. Phys.*, 2017, **19**, 16806–16818.

128 R. En, S. Graci, N. Bezlyepkina, R. L. Knorr, R. Lipowsky, R. Dimova, R. S. Gracià, N. Bezlyepkina, R. L. Knorr, R. Lipowsky and R. Dimova, *Soft Matter*, 2010, **6**, 1472–1482.

129 J. A. Szule, N. L. Fuller and R. Peter Rand, *Biophys. J.*, 2002, **83**, 977–984.

130 S. Chakraborty, M. Doktorova, T. R. Molugu, F. A. Heberle, H. L. Scott, B. Dzikovski, M. Nagao, L.-R. Stingaciu, R. F. Standaert, F. N. Barrera, J. Katsaras, G. Khelashvili, M. F. Brown and R. Ashkar, , DOI:10.1073/pnas.2004807117/-/DCSupplemental.

131 T. Robinson and P. S. Dittrich, *ChemBioChem*, 2019, **20**, 2666–2673.

132 A. Bradford, J. Atkinson, N. Fuller and R. P. Rand, *J. Lipid Res.*, 2003, **44**, 1940–5.

133 Š. Perutková, M. Daniel, G. Dolinar, M. Rappolt, V. Kralj-Iglič and A. Iglič, *Adv. Planar Lipid Bilayers Liposomes*, 2009, **9**, 237–278.

134 P. Mariani, V. Luzzati and H. Delacroix, *J. Mol. Biol.*, 1988, **204**, 165–189.

135 J. Juhasz, F. J. Sharom and J. H. Davis, *BBA - Biomembr.*, 2009, **1788**, 2541–2552.

136 J. H. Davis, J. J. Clair and J. Juhasz, *Biophysj*, **96**, 521–539.

137 E. N. Frankel, S.-W. Huang, J. Kanner and J. B. German, *J. Agric. Food Chem*, 1994, **42**, 1054–1059.

138 S. Ichikawa, S. Sugiura, M. Nakajima, Y. Sano, M. Seki and S. Furusaki, *Biochem. Eng. J.*, 2000, **6**, 193–199.

139 A. I. Hopia, S.-W. Huang, K. Schwarz, J. B. German and E. N. Frankel, .

140 K. W. Miller and D. M. Small, *J. Colloid Interface Sci.*, 1982, **89**, 466–478.

141 G. Lindblom and L. Rilfors, *Biochim. Biophys. Acta - Rev. Biomembr.*, 1989, **988**, 221–256.

142 M. Johnsson, J. Barauskas and F. Tiberg, *J. Am. Chem. Soc.*, 2005, **127**, 1076–1077.

143 G. Orädd, G. Lindblom, K. Fontell and H. Ljusberg-Wahren, *Biophys. J.*, 1995, **68**, 1856–1863.

144 L. Lei, Y. Ma, D. R. Kodali, J. Liang and H. T. Davis, *J. Am. Oil Chem. Soc.*, 2003, **80**, 383–388.

145 B. Chen, D. J. McClements and E. A. Decker, *Crit. Rev. Food Sci. Nutr.*, 2011, **51**, 901–916.

146 E. S. Budilarto and A. Kamal-Eldin, *Eur. J. Lipid Sci. Technol.*, 2015, **117**, 1095–1137.

147 A. Sadeghpour, M. L. Parada, J. Vieira, M. Povey and M. Rappolt, *J. Phys. Chem. B*, 2018, **122**, 10320–10329.

148 E. Y. Shalaev and P. L. Steponkus, *Biochim. Biophys. Acta - Biomembr.*, 1999, **1419**, 229–247.

149 M. G. Corradini and D. Julian McClements, in *Reference Module in Chemistry, Molecular Sciences and Chemical Engineering*, Elsevier, 2017.

150 G. Schmidt, S. Müller, P. Lindner, C. Schmidt and W. Richtering, *J. Phys. Chem. B*, 1998, **102**, 507–513.

151 M. Rappolt, F. Cacho-Nerin, C. Morello and A. Yaghmur, *Soft Matter*, 2013, **9**, 6291.

152 K. M. Lebold and M. G. Traber, *Free Radic. Biol. Med.*, 2014, **66**, 13–19.

153 M. S. Brewer, *Compr. Rev. Food Sci. Food Saf.*, 2011, **10**, 221–247.

154 D. C. Turner and S. M. Gruner, *Biochemistry*, 2002, **31**, 1340–1355.

155 P. E. Harper, A. T. Cavazos, J. J. Kinnun, H. I. Petrache and S. R. Wassall, *Langmuir*, 2020, **36**, 4908–4916.

156 G. C. Shearman, A. I. I. Tyler, N. J. Brooks, R. H. Templer, O. Ces, R. V. Law and J. M. Seddon, *Liq. Cryst.*, 2010, **37**, 679–694.

157 X. Zeng, Y. Liu and M. Impéror-Clerc, *J. Phys. Chem. B*, 2007, **111**, 5174–5179.

158 T. C. Walther and R. V. Farese, *Annu. Rev. Biochem.*, 2012, **81**, 687–714.

159 A. R. Thiam, R. V. Farese Jr and T. C. Walther, *Nat. Rev. Mol. Cell Biol.*, 2013, **14**, 775–786.

160 K. Ben M'barek, D. Ajjaji, A. Chorlay, S. Vanni, L. Forêt and A. R. Thiam, *Dev. Cell*, 2017, **41**, 591-604.e7.

161 J. A. Olzmann and P. Carvalho, *Nat. Rev. Mol. Cell Biol.*, 2019, **20**, 137–155.

162 S. O. Olofsson, P. Boström, L. Andersson, M. Rutberg, M. Levin, J. Perman and J. Borén, *Curr. Opin. Lipidol.*, 2008, 19, 441–447.

163 A. R. Thiam and L. Forêt, *Biochim. Biophys. Acta - Mol. Cell Biol. Lipids*, 2016, **1861**, 715–722.

164 A. Chorlay, L. Forêt and A. R. Thiam, *Biophys. J.*, 2021, **120**, 5491–5503.

165 P. Campomanes, V. Zoni and S. Vanni, *Commun. Chem.*, 2019, **2**, 72.

166 V. T. Salo, S. Li, H. Vihinen, M. Hölttä-Vuori, A. Szkalisity, P. Horvath, I. Belevich, J. Peränen, C. Thiele, P. Somerharju, H. Zhao, A. Santinho, A. R. Thiam, E. Jokitalo and E. Ikonen, *Dev. Cell*, 2019, **50**, 478-493.e9.

167 V. Zoni, R. Khaddaj, P. Campomanes, A. R. Thiam, R. Schneiter and S. Vanni, *Elife*, 2021, **10**, 1–24.

168 A. Chorlay and A. R. Thiam, *Biophys. J.*, 2018, **114**, 631–640.

169 W. M. Henne, M. L. Reese and J. M. Goodman, *EMBO J.*, , DOI:10.15252/embj.201898947.

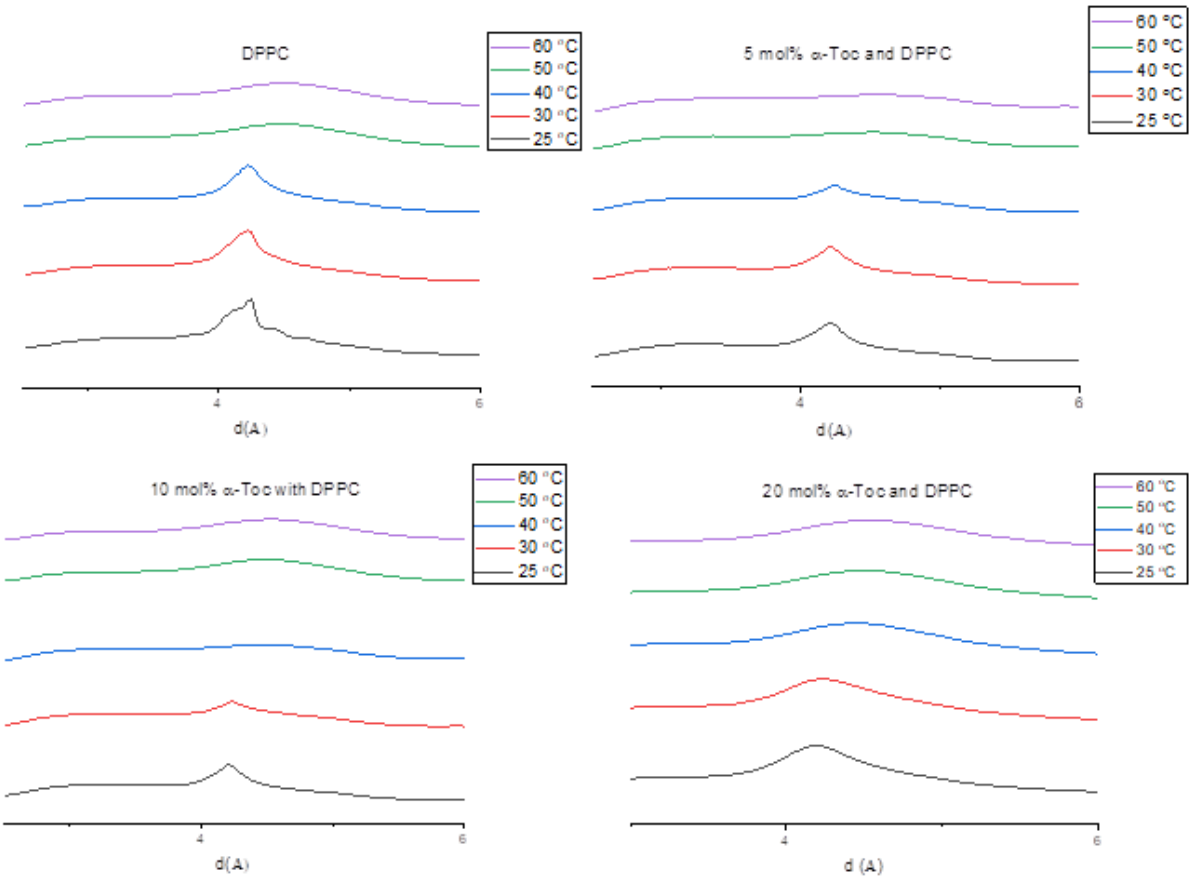
170 P. Sengupta, B. Baird and D. Holowka, *Semin. Cell Dev. Biol.*, 2007, **18**, 583–590.

171 X. Leng, J. J. Kinnun, D. Marquardt, M. Ghefli, N. Kučerka, J. Katsaras, J. Atkinson, T. A. Harroun, S. E. Feller and S. R. Wassall, *Biophys. J.*, 2015, **109**, 1608–1618.

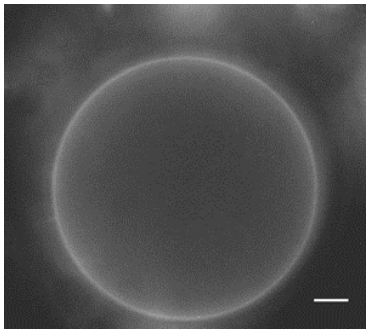
172 A. Roux and R. Loewith, *Dev. Cell*, 2017, 41, 571–572.

Chapter 10: Supplementary Information

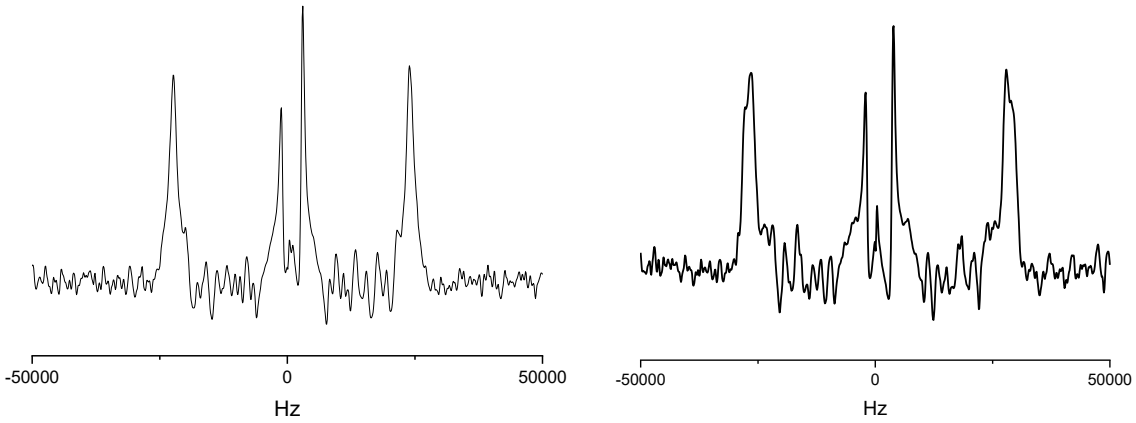
10.1 Supplementary Information Chapter 4 (SI4)



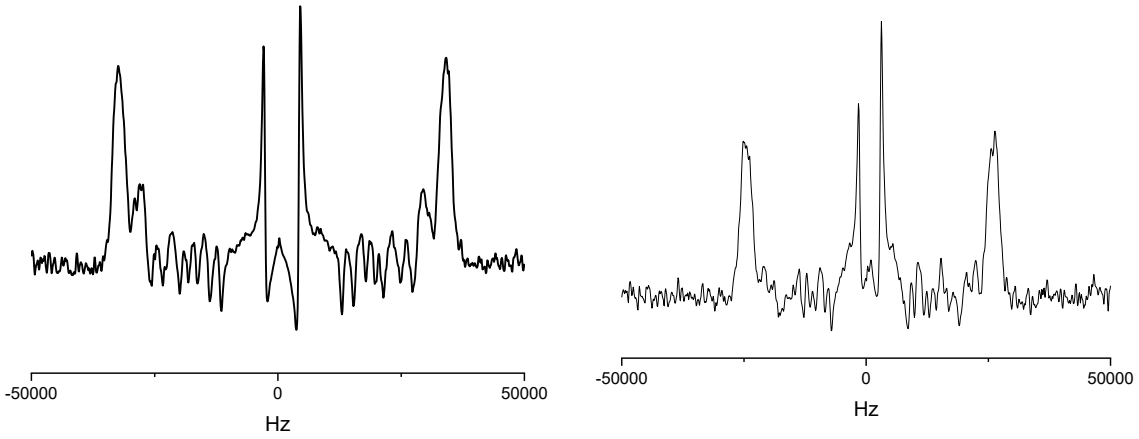
SI 4. 1 WAXS plots of DPPC with 5, 10 and 20 mol% α-Toc at various temperatures. With increasing α-Toc compositions, the WAXS peak broadens and flattens out.



SI 4. 2 Fluorescently tagged GUV comprising of equimolar DPPC and DOPC depicting a uniform phase



SI 4. 4 Depaked NMR spectra of DPPC: DOPC at 25 °C (left) and 60 °C (right)



SI 4. 5 Depaked NMR spectra of DPPC: DOPC: α-Toc (2:2:1) at 25 °C (left) and 60 °C (right)

For an oblique lattice, the reciprocal lattice is given by:

$$S^2 = h^2a^{*2} + k^2b^{*2} + 2hka^*b^*cos\gamma^* \qquad \text{Eq.4.1}$$

Where:

$$S_{(hk)} = \frac{1}{d_{(hk)}} \qquad \text{Eq. 4.2}$$

$$a^* = \frac{1}{asin\gamma} \qquad \text{Eq. 4.3}$$

$$b^* = \frac{1}{bsin\gamma} \qquad \text{Eq. 4.4}$$

$$\gamma^* = 180° - \gamma \qquad \text{Eq. 4.5}$$

For the (0,1) peak, eq.4.1 becomes:

$$S^2_{(0,1)} = b^{*2}$$

For the (1,0) peak eq. 4.1 becomes:

$$S^2_{(1,0)} = a^{*2}$$

These values can then be substituted into eq 4.1 for the (1,1) peak and solved to find ϒ.

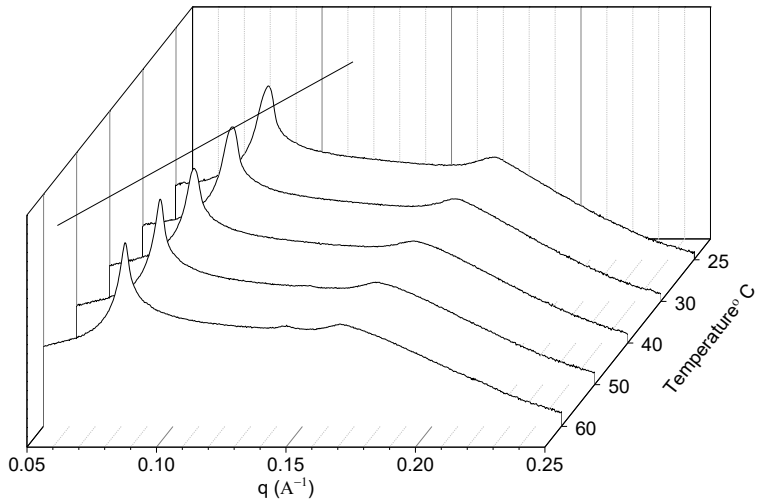
$$\gamma^* = cos^{-1}\left(\frac{S^2_{(1,1)} - a^{*2} - b^{*2}}{2a^*b^*}\right) \qquad \text{Eq. 4.6}$$

In the case of 10 mol% α-Toc with DPPC, the (0,1) peak is not present. In this case the (2,1) peak was used in equation 4.1 to give:

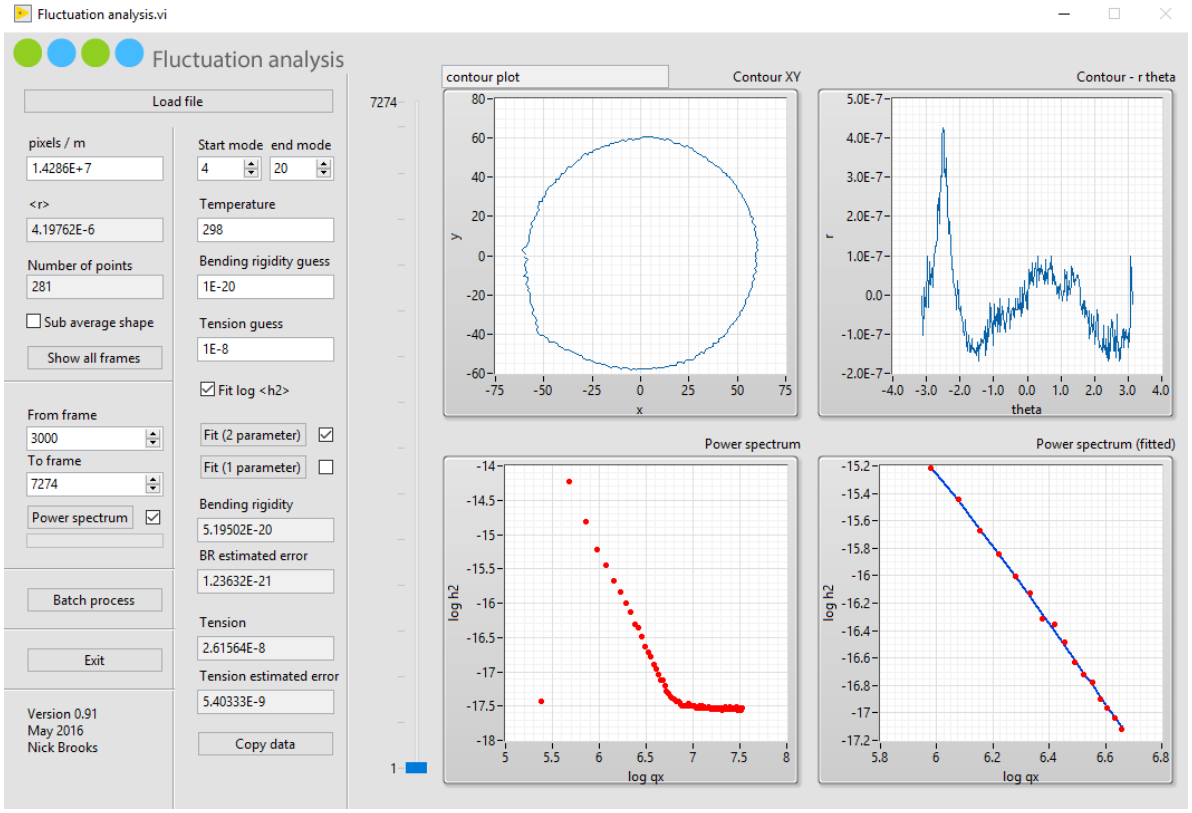
$$\gamma^* = cos^{-1}\left(\frac{S^2_{(2,1)} - 4a^{*2} - b^{*2}}{4a^*b^*}\right) \qquad \text{Eq. 4.7}$$

Equations 4.6 and 4.7 were substituted into each other to calculate b^* and then γ^*.

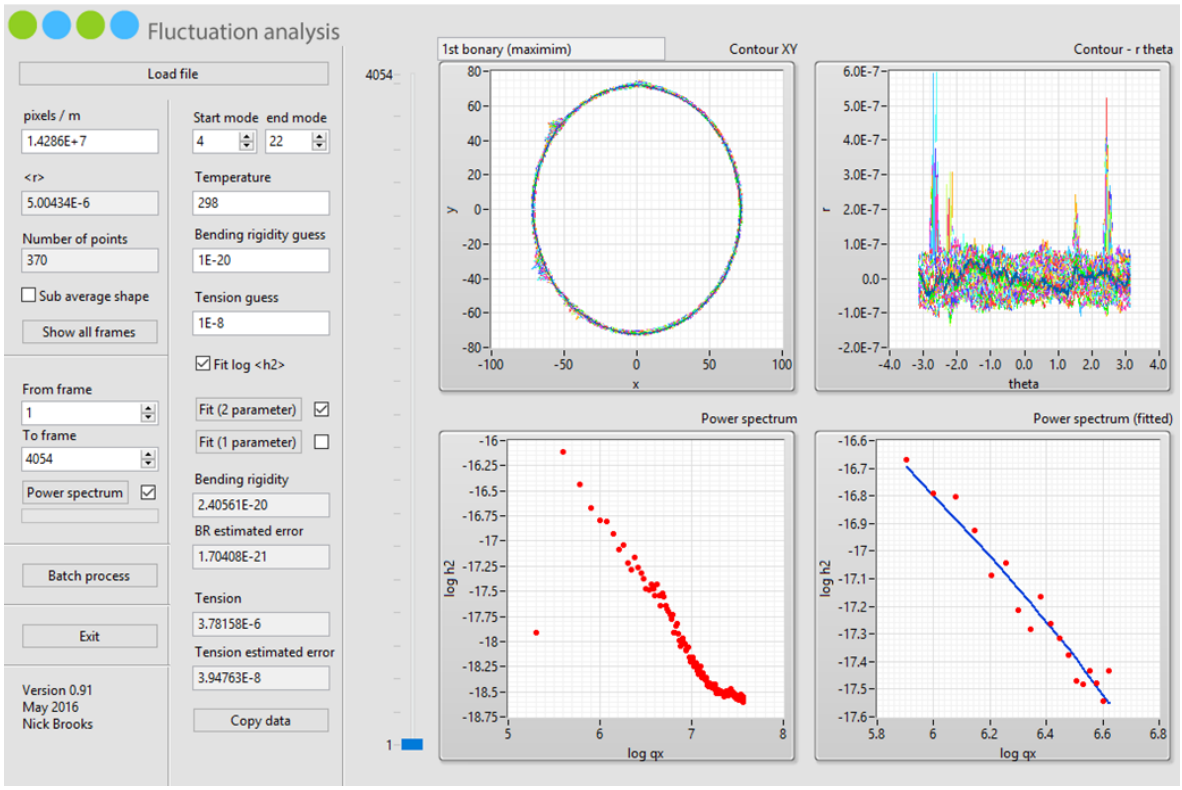
10.2 Supplementary Information Chapter 5 (SI5)



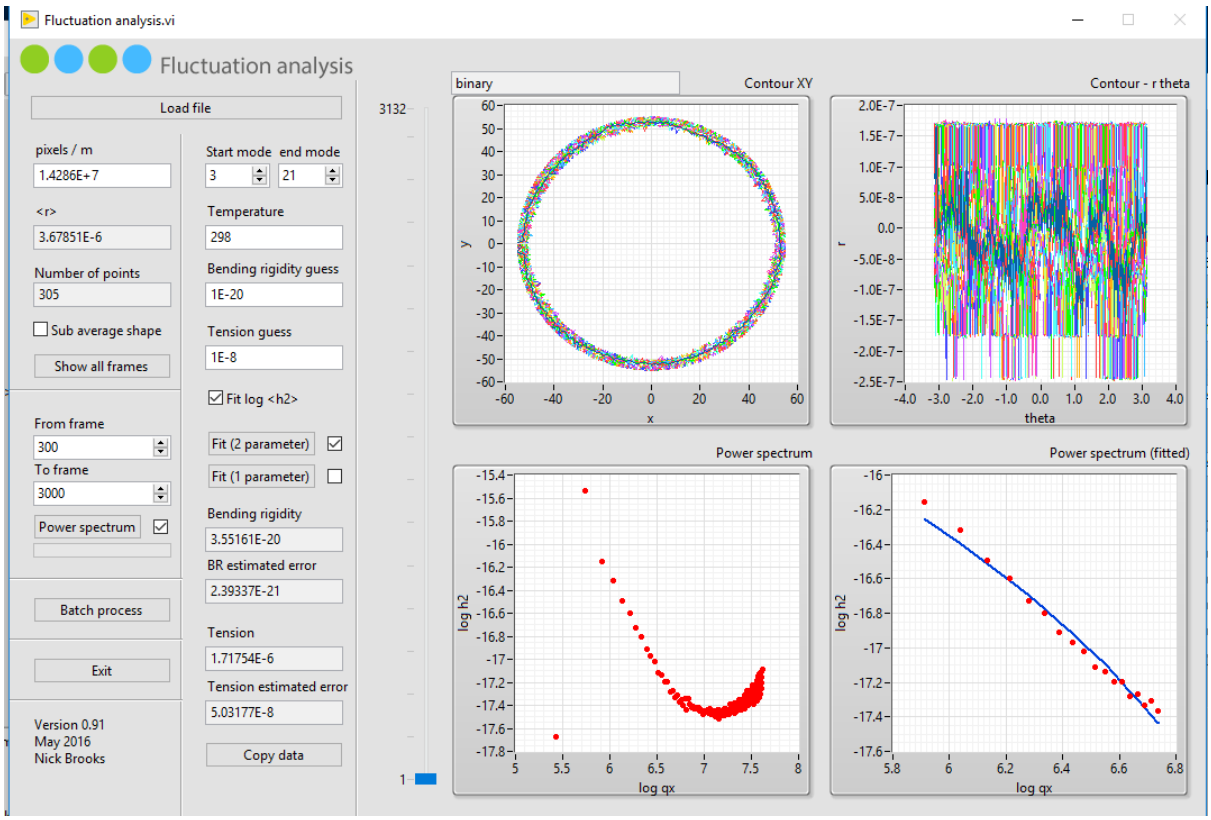
SI 5. 1 Temperature scan of 30 mol% α-Toc with DOPC in excess water. A single (10) peak is retained at each temperature.



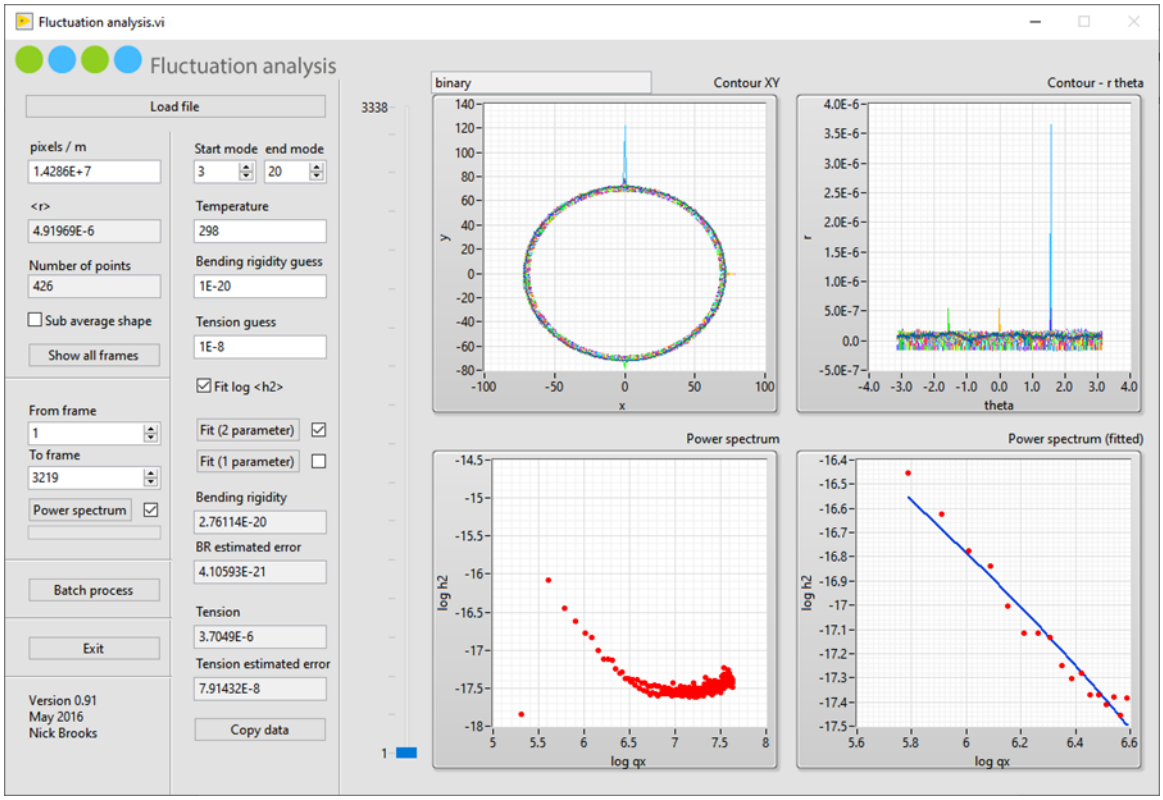
SI 5. 2 Fluctuation Analysis results of pure DOPC



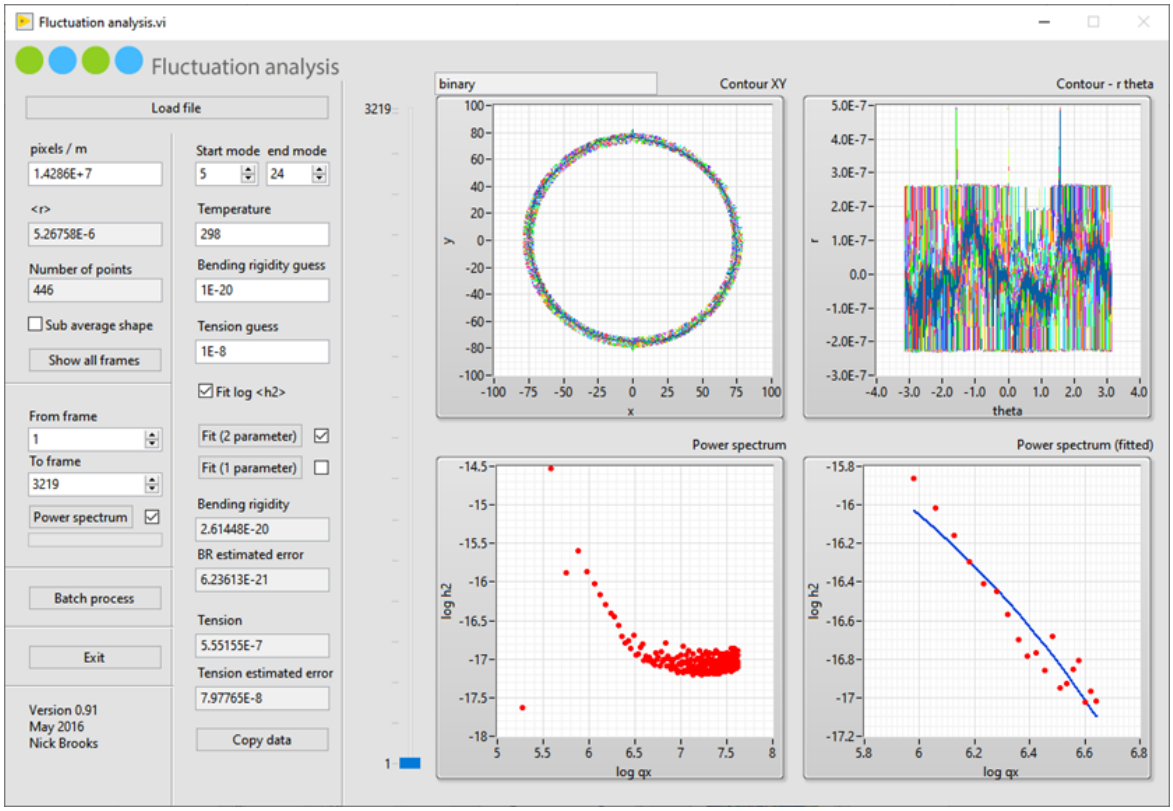
SI 5. 3 Fluctuation Analysis results of 5 mol% α-Toc with DOPC



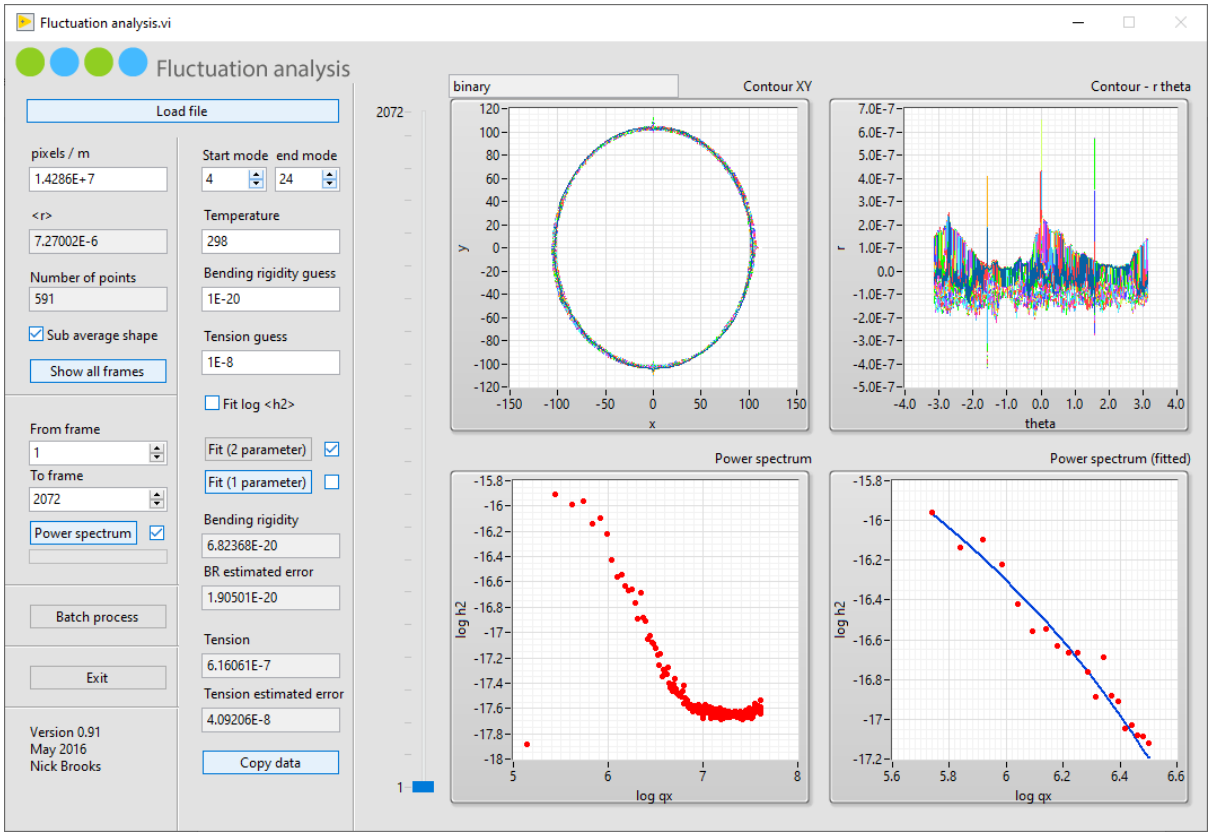
SI 5. 4 Fluctuation Analysis results of 10 mol% α-Toc with DOPC



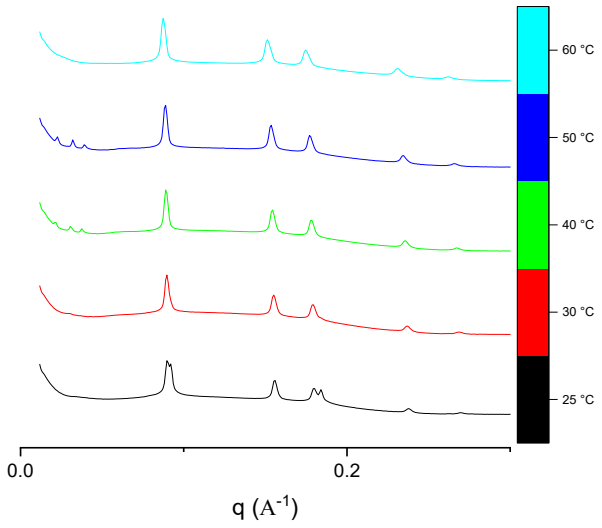
SI 5. 5 Fluctuation Analysis results of 15 mol% α-Toc with DOPC



SI 5. 6 Fluctuation Analysis results of 20 mol% α-Toc with DOPC

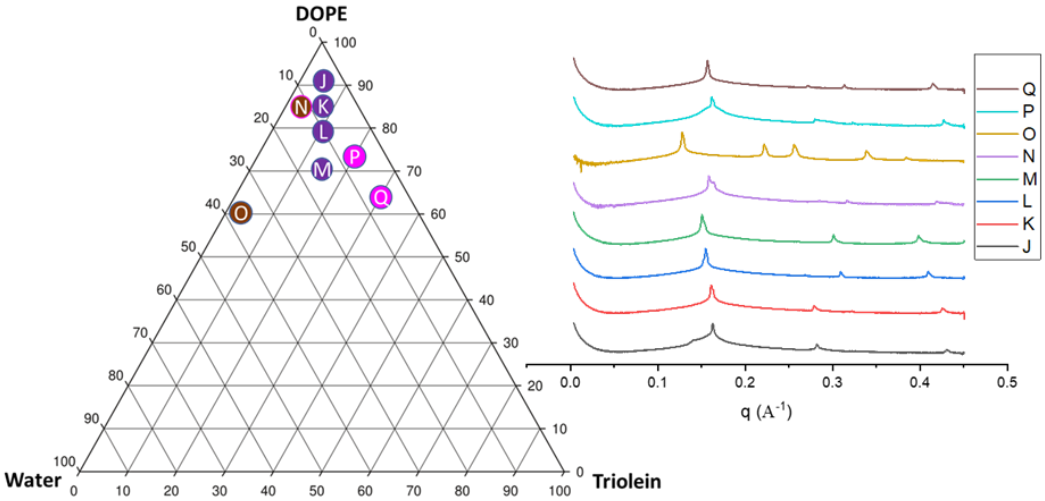


SI 5. 7 Fluctuation Analysis results of 30 mol% α-Toc with DOPC

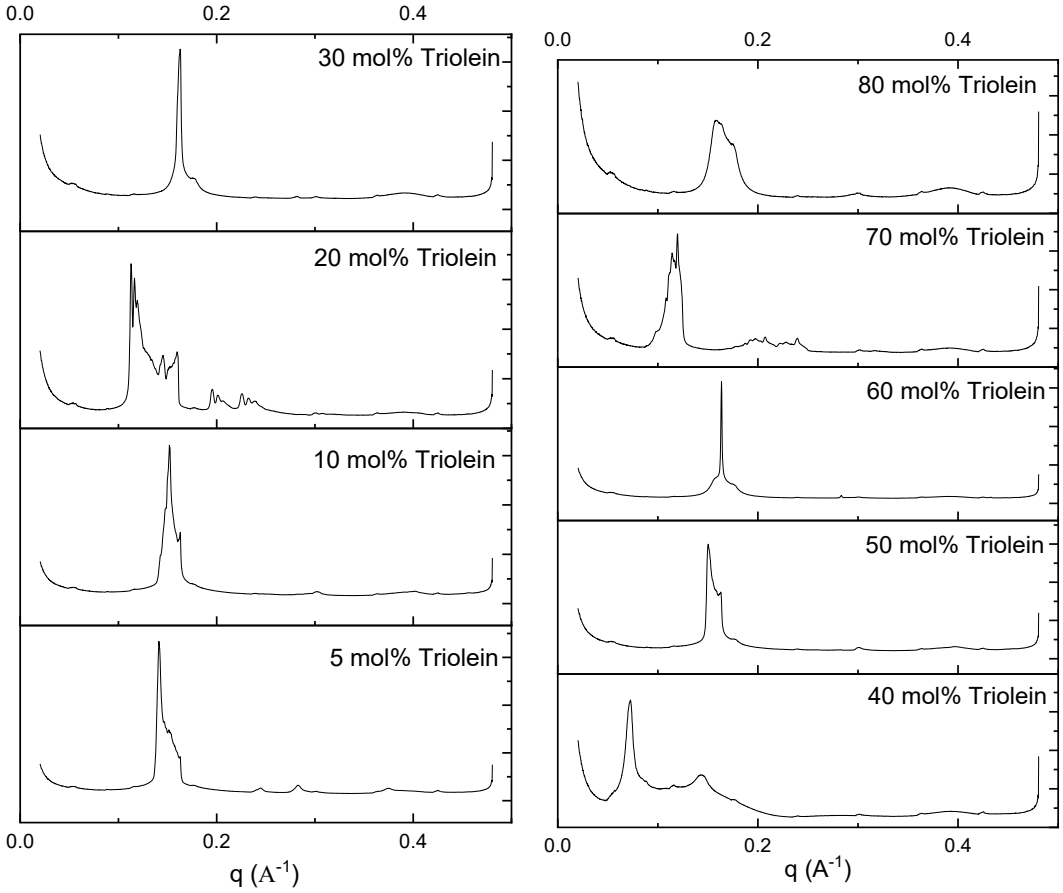


SI 5. 8 SAXS data of composition I, 40 mol% α-Toc with 1:1 (DPPC: DOPC), at various temperatures in excess water. At 25 °C, there may be phase co-existence of the lamellar and H_{II} phases, however at higher temperatures the lamellar phase is not present and emergence of the Im3m phase can be seen with H_{II}

10.3 Supplementary Information Chapter 6 (SI6)



Supplementary Figure 6. 1 Ternary phase diagram of triolein, Water and DOPE (wt%) with corresponding SAXS patterns mostly depicting H_{II} phases. The compositions of triolein: Water: DOPE are: (J) 1:1:18 (K) 1:1:11.3 (L) 1:1:8 (M) 1:1:4.7 (N) 1:2.2:19 (O)1:10.8:19 (P) 2.5:1:9 (Q) 4.3:1:9



S.I 6. 2 SAXS data of DOPE with triolein in excess water at 25 °C (mol% Triolein given on figure). All peaks can be indexed to a H_{II} phase; however the Bragg peaks are distorted and additional unassigned peaks are present.

HCP phase analysis

$$\frac{1}{d_{hkl}^2} = \frac{1}{a^2}\left(\frac{4}{3}(h^2 + k^2 + hk) + \frac{1}{R^2}l^2\right)$$

Where R=$\frac{c}{a}$

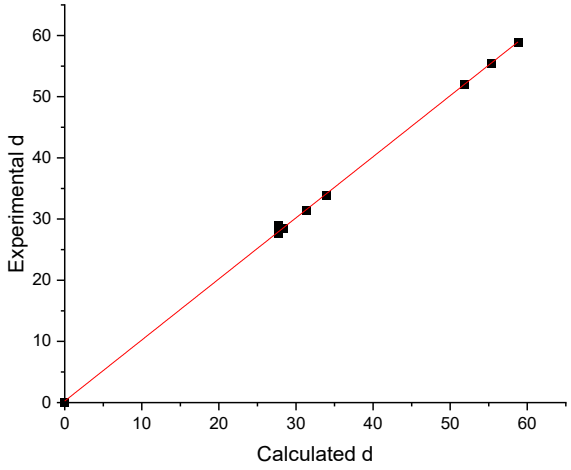
For the (010) peak, the equation becomes:

$$\frac{1}{d_{010}^2} = \frac{4}{3a^2}$$

For the (004) peak, the equation becomes:

$$\frac{1}{d_{004}^2} = \frac{16}{c^2}$$

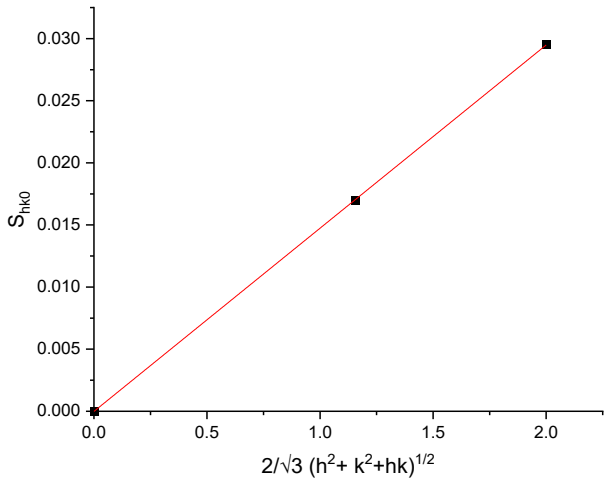
Substituting experimental d values, allows for the calculation of the lattice parameters a and c.



Supplementary Figure 6. 2. The calculated d-spacings of the *hcp* phase with respect to experimental d spacings show a close agreement.

According to equation 6.1, if l=0 then s_{hk0} vs. $\frac{2}{\sqrt{3}}(h^2 + k^2 + hk)^{1/2}$ would yield a straight line. This shows proof of the formation of the hcp phase ($s_{hk0} = \frac{1}{d}$)

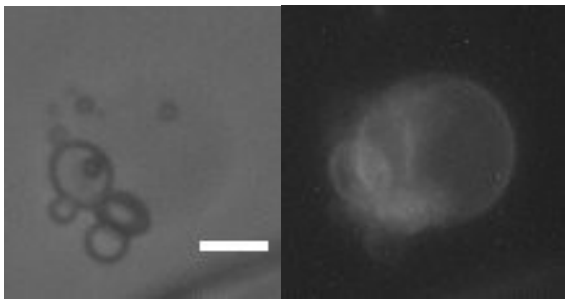
Index hkl (where l=0)	$\frac{2}{\sqrt{3}}(h^2 + k^2 + hk)^{1/2}$	**Experimental d (Å)**	**S_{hk0}**
010	$\frac{2}{\sqrt{3}}$	58.8	0.017
110	2	33.9	0.0295



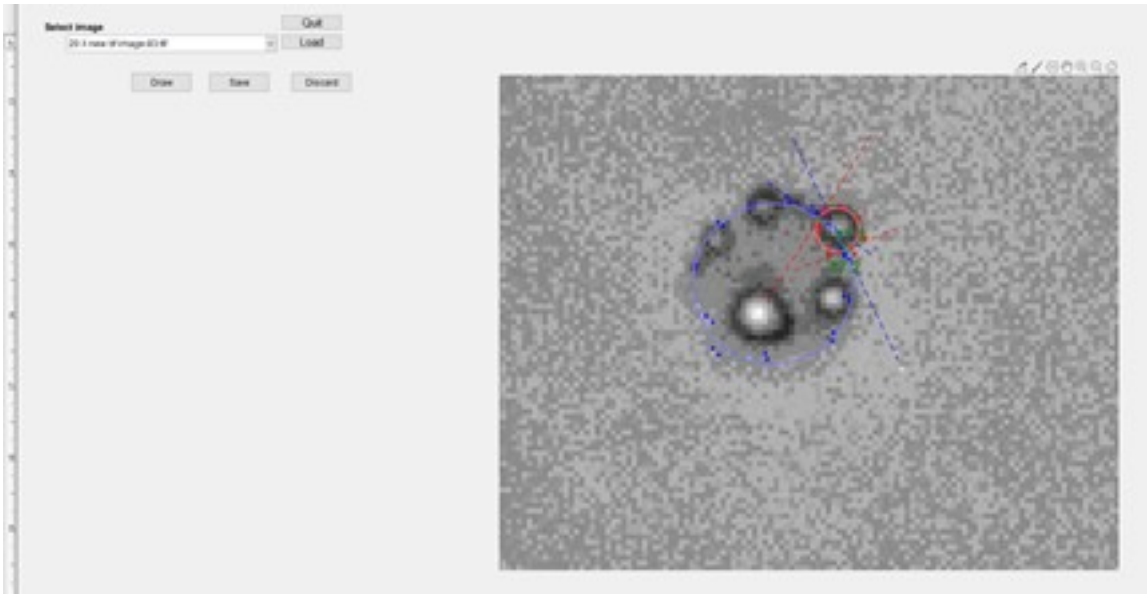
Supplementary Figure 6. *4*. The calculated d-spacings of the hcp phase with respect to experimental d spacings show a close agreement

10.4 Supplementary Information Chapter 7 (SI7)

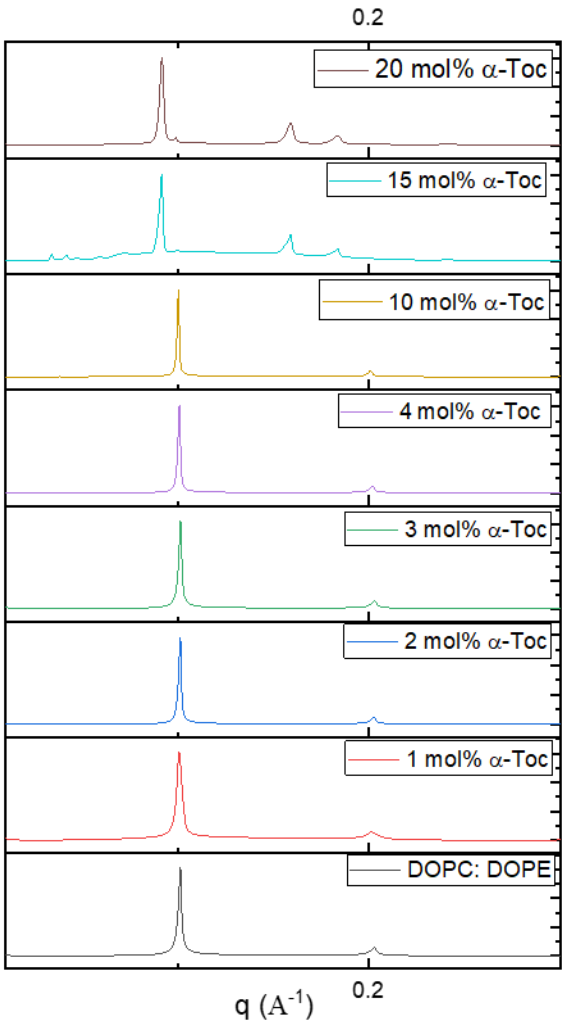
Supplementary Information



SI 7. 1 Brightfield image of a DEV (left) and a fluorescent image of DEV (right). The continuity of the fluorescence in the lipid droplet depicts that the oil is encapsulated between the bilayers



SI 7. 2 Calculation of the contact angle was computed on MATLAB. The contact angle can only be found for DEVs in which there is an oil droplet on the edge.



SI 7. 3 SAXS of equimolar DOPC: DOPE with various compositions of α-Toc at 25°C (excess water). A lamellar phase is present up until 10 mol%, beyond this concentration the curved hexagonal and cubic phases are present.